Contrast Media & Molecular Imaging

Use of Animal Models in Molecular Imaging

Lead Guest Editor: Aage K. O. Alstrup
Guest Editors: Svend B. Jensen, Michael Pedersen, Pia Afzelius, and Pedro Rosa-Neto

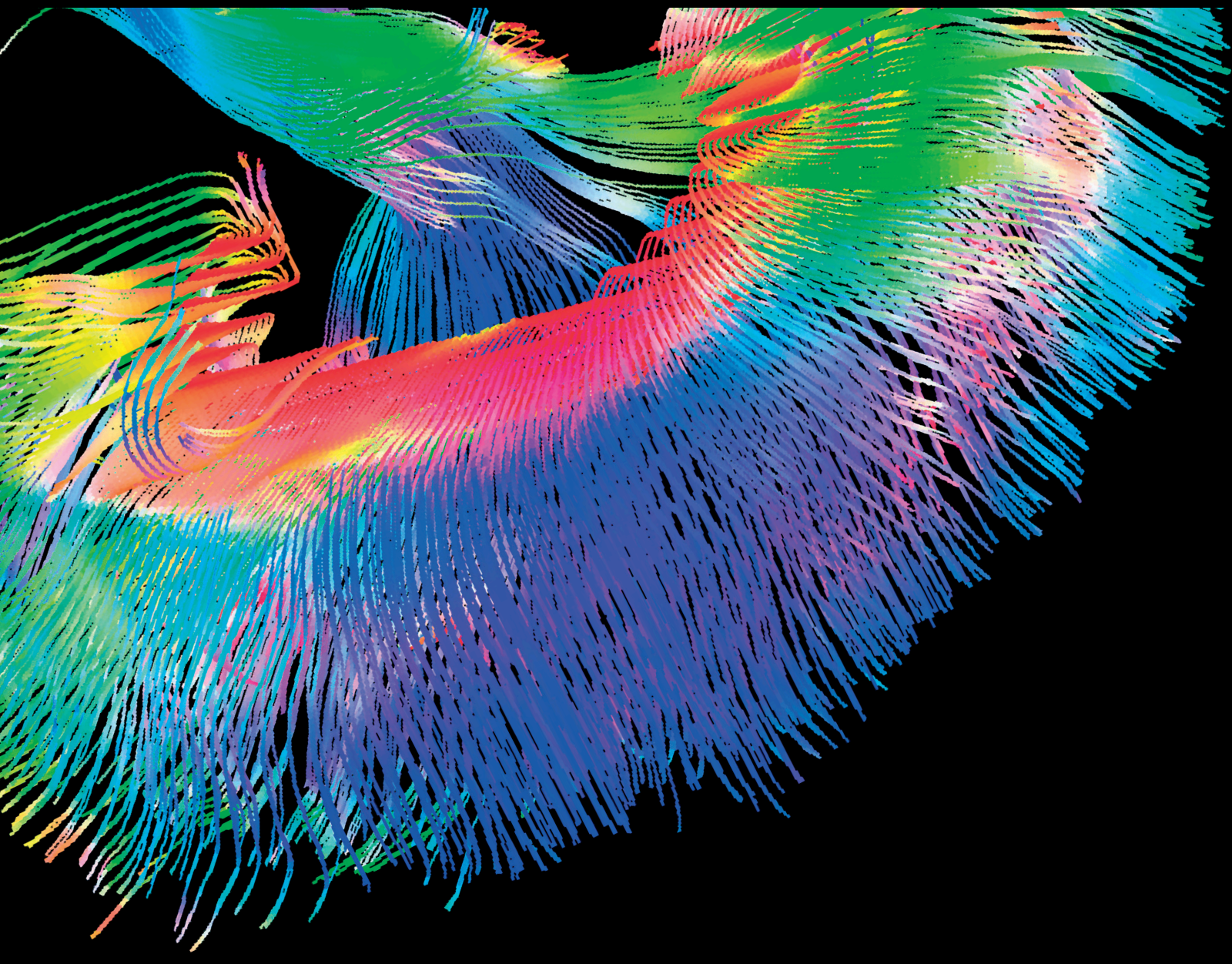

Use of Animal Models in Molecular Imaging

Contrast Media & Molecular Imaging

Use of Animal Models in Molecular Imaging

Lead Guest Editor: Aage K. O. Alstrup
Guest Editors: Svend B. Jensen, Michael Pedersen, Pia Afzelius, and Pedro Rosa-Neto

Contents

Hindawi
Contrast Media & Molecular Imaging
Volume 2020, Article ID 5168147, 2 pages
https://doi.org/10.1155/2020/5168147

Editorial

Use of Animal Models in Molecular Imaging

Aage Kristian Olsen Alstrup,[1] **Svend Borup Jensen**,[2,3] **Pia Afzelius**,[4] **Pedro Neto**,[5] **and Michael Pedersen**[1]

[1]*Aarhus University Hospital, Aarhus, Denmark*
[2]*Aalborg University Hospital, Aalborg, Denmark*
[3]*Department of Chemistry and Biosciences Aalborg University, Aalborg, Denmark*
[4]*Nordsjællands Hospital, Hillerød, Denmark*
[5]*McGill University, Montreal, Canada*

Correspondence should be addressed to Aage Kristian Olsen Alstrup; aagealst@rm.dk

Received 17 December 2019; Accepted 18 December 2019; Published 14 February 2020

Modern preclinical research is continuously using imaging techniques to provide scientific results useful for human medicine. The imaging techniques provide either morphological or volumetric presentations of the organs of interest, hemodynamic measures of the cardiovascular system, and/or semiquantitative/empirical parameters of the cellular metabolism and function [1]. Disease progression is followed noninvasively over time in experimental animal models, providing information about pathophysiologic characteristics that mimic human diseases [2]. In parallel, focus emerges regarding reduction of both suffering and the number of experimental animals used per study, in accordance with the principles behind 3 Rs for good animal ethics in research: replacement, reduction, and refinement [3].

Experimental animals must be situated in a fixed position and respiratory and physiologically stable to ensure imaging with optimal quality [4, 5]. Nonetheless, little attention has been paid to the impact of anesthesia, sex, choice of species and strain/stock, housing conditions, diet/fasting, behavioral scores, circadian rhythm, etc, on the acquired data [6]. Consequently, the rate of successful translation from animal models to human diseases is modest. This failure to translate from animals to humans is likely due, in part, to poor methodology and failure of the models to accurately mimic the human disease condition [7]. However, a deeper insight into the abovementioned parameters could likely improve the translation ability of preclinical animal models. Therefore, we need to address these fundamental issues in experimental animal research.

This special issue in Contrast Media and Molecular Imaging focuses on these issues, and the emphasis is on the relationship between molecular imaging measures and the impact of factors.

In one of the published studies, M. D. Overgaard and coworkers investigated the placental uptake of a radiolabeled tracer. The authors recognized that the biological differences in the placenta between laboratory chinchillas and humans made it difficult to transfer the results. Another research team who also used pregnant chinchillas had more luck. Using ultrasound, A. Greco and coworkers examined the development of the fetuses, including the age of the fetuses and found that pregnant chinchillas are, in this context, useful models for human pregnancy.

The choice of model, as well as experimental animals to mimic humans, was the subject of a PET study comparing dosimetry of a drug performed in mice, pigs, and humans. S. Beykan and coworkers showed that the pig model was a superior model for humans.

In another study, the researchers examined possible pitfalls with imaging of myelin following lysophosphatidylcholine (LPC) injections in the central nervous system in a well-known animal model of demyelination. M. Zhang and coworkers conclusion was that the PET scans advantageously could be supplemented with an MRI scan to avoid the risk of false results due to LPC side effects.

A group of researchers applied an MRI scan for quantifying iron overload in the liver in a mouse model. Y. Matsuo-Tezeka and coworkers found that MRI T2 ∗

relaxation time was able to determine the content with high sensitivity. In another MRI study perfomed by K. M. Parkins and coworkers and also performed with mice, showed that engineered cells did not form tumors as well as their naïve counterparts, demonstrating the scanner's ability to evaluate animal models.

Furthermore, this special issue includes a review published by G. Musch on molecular imaging techniques to penetrate the depth of the pathophysiological mechanisms at stake during acute pulmonary disease.

Conflicts of Interest

The editors declare that they have no conflicts of interest regarding the publication of this special issue.

Aage Kristian Olsen Alstrup
Svend Borup Jensen
Pia Afzelius
Pedro Neto
Michael Pedersen

References

[1] P. H. Elsinga, A. Waarde, A. M. J. Paans, and R. A. J. O. Dierckx, *Trends on the Role of PET in Drug Development*, World Scientific, Singapore, 2012.

[2] I. E. Holm, A. K. O. Alstrup, and Y. Luo, "Genetically modified pig models for neurodegenerative disorders," *Journal of Pathology*, vol. 238, no. 2, pp. 167–187, 2016.

[3] W. M. S. Russell and R. L. Burch, *The Principles of Human Experimental Technique*, University of California, CA, USA, 1959.

[4] S. Gargiulo, A. Greco, M. Gramanzini et al., "Mice anesthesia, analgesia, and care, part II: anesthetic considerations in preclinical imaging studies," *ILAR Journal*, vol. 53, no. 1, pp. E70–E81, 2012.

[5] A. K. O. Alstrup and D. F. Smith, "PET neuroimaging in pigs," *Scandinavian Journal of Laboratory Animal Science*, vol. 1, pp. 1–21, 2012.

[6] A. K. O. Alstrup and D. F. Smith, "Anaesthesia for positron emission tomography scanning of animal brains," *Laboratory Animals*, vol. 47, no. 1, pp. 12–18, 2013.

[7] C. G. Begley and J. P. A. Ioannidis, "Reproducibility in science," *Circulation Research*, vol. 116, no. 1, pp. 116–126, 2015.

Hindawi
Contrast Media & Molecular Imaging
Volume 2019, Article ID 7463047, 7 pages
https://doi.org/10.1155/2019/7463047

Research Article

T2* Relaxation Time Obtained from Magnetic Resonance Imaging of the Liver Is a Useful Parameter for Use in the Construction of a Murine Model of Iron Overload

Yukari Matsuo-Tezuka, Yusuke Sasaki, Toshiki Iwai, Mitsue Kurasawa, Keigo Yorozu, Yoshihito Tashiro, and Michinori Hirata

Product Research Department, Chugai Pharmaceutical Co. Ltd., Kamakura, Japan

Correspondence should be addressed to Michinori Hirata; hiratamcn@chugai-pharm.co.jp

Received 15 October 2018; Revised 8 March 2019; Accepted 1 September 2019; Published 22 September 2019

Guest Editor: Michael Pedersen

Aim. Iron overload is a life-threatening disorder that can increase the risks of cancer, cardiovascular disease, and liver cirrhosis. There is also a risk of iron overload in patients with chronic kidney disease. In patients with renal failure, iron storage is increased due to inadequate iron utilization associated with decreased erythropoiesis and also to the inflammatory status. To evade the risk of iron overload, an accurate and versatile indicator of body iron storage in patients with iron overload is needed. In this study, we aimed to find useful iron-related parameters that could accurately reflect body iron storage in mice in order to construct a murine model of iron overload. *Methods*. To select an appropriate indicator of body iron status, a variety of parameters involved in iron metabolism were evaluated. Noninvasively measured parameters were R1, R2, and R2* derived from magnetic resonance imaging (MRI). Invasively measured parameters included serum hepcidin levels, serum ferritin levels, and liver iron contents. Histopathological analysis was also conducted. *Results/Conclusion*. Among the several parameters evaluated, the MRI T2* relaxation time was able to detect iron storage in the liver as sensitively as serum ferritin levels. Moreover, it is expected that using an MRI parameter will allow accurate evaluation of body iron storage in mice over time.

1. Introduction

Iron is an essential element for biological function. However, excess iron has the potential for life-threatening consequences via production of reactive oxygen species (ROS). It is reported that under iron-overload conditions, mitochondrial DNA and organs are damaged by ROS produced by the labile iron pool [1]. A typical iron-overload disease is hereditary hemochromatosis. It is characterized by dysregulated iron absorption and subsequent overaccumulation of iron in various tissues such as the liver, pancreas, heart, and joints [2]. Prolonged iron-overload conditions cause liver cirrhosis, liver cancer, and diabetes [3, 4].

To evade iron-overload disease, it is crucial to assess body iron storage in an appropriate manner. However, it is difficult to know the exact status of body iron storage because iron metabolism is influenced by various factors such as inflammation, erythropoiesis, and disease conditions [5]. A typical example of dysregulated iron metabolism is found in chronic kidney disease (CKD) [6]. In patients with chronic renal failure, damaged kidneys produce less erythropoietin than do healthy kidneys, which causes a reduction in erythropoietic activity and consequently a reduction in iron utilization for hemoglobin synthesis. As a result, iron storage is increased in CKD patients. Moreover, in patients with CKD, production of proinflammatory cytokines is also increased in association with renal failure and uremia. Cytokines such as IL-6 are known to dysregulate iron homeostasis via the upregulation of hepcidin, a key regulator of iron homeostasis [7]. Thus, it is difficult to accurately assess body iron status in patients with inflammation, erythropoietic failure, and dysregulated iron

homeostasis. Considering the risk posed by dysregulation of iron homeostasis, especially the risk of iron overload, development of an accurate and versatile indicator of body iron storage is necessary.

As indicators of body iron storage, serum ferritin level is usually used in the clinical setting as is the concentration of serum/plasma hepcidin, which is reported to correlate well with liver iron concentration [8, 9]. Although these are commonly used, there are limits to their application because serum ferritin and hepcidin levels are easily influenced by inflammatory status and erythropoietic status. Although liver biopsy is infrequent in the clinical setting, its versatility is low in terms of its invasiveness. Magnetic resonance imaging (MRI) is coming to be used in clinical settings as a tool with which to assess body iron storage, not only visually but also quantitatively [10]. One of the advantages of MRI is its noninvasiveness, allowing MRI to be used for sequential assessment of target atoms/molecules. MRI is also considered to be advantageous for assessment of body iron status in that it is not influenced by inflammation-mediated disorders of iron metabolism. However, the use of MRI is not popular due to its high cost and poor access. In summary, although there are various parameters used for assessing body iron status in the clinical setting, each has its advantages and disadvantages. In this study, we sought an optimal indicator of body iron storage for use in nonclinical research.

In nonclinical research with mice, liver iron concentration can be used as an absolute reference for body iron storage. We constructed an iron loading model by injecting mice with different dosages of iron-dextran and measured various iron parameters to select effective biomarkers for body iron storage. As invasive indicators of body iron storage, we measured serum ferritin and hepcidin and evaluated their correlations with liver iron concentration. As noninvasive indicators, T1, T2, and T2* relaxation time of the liver were measured by an MRI system designed for use with mice. We evaluated the correlations between liver iron concentration and other iron-related parameters including MRI parameters.

2. Materials and Methods

2.1. Chemicals and Antibodies. Iron-dextran and Dulbecco's phosphate-buffered saline were purchased from Sigma-Aldrich (St. Louis, MO, USA). All other chemicals and solvents were of analytical reagent grade.

2.2. Animals. Seven-week-old male C57BL/6NCrlCrlj mice were purchased from Charles River Laboratories Japan (Kanagawa, Japan). All animals were allowed to acclimatize for 8 days to recover from shipping-related stress prior to the study. Mice were housed under specific pathogen-free conditions with free access to food and water. All studies were approved by the Institutional Animal Care and Use Committee at Chugai Pharmaceutical Co., Ltd., and conformed to the Institute for Laboratory Animal Research (ILAR).

2.3. Animal Treatment. Iron-dextran was diluted to appropriate concentrations in phosphate buffer vehicle (phosphate-buffered saline containing 0.02% polyoxyethylene sorbitan monooleate (Tween 80)). Iron-loaded mice were prepared by intraperitoneal injection of iron-dextran (0.1, 0.5, or 2.5 mg/mouse). Three days after iron or vehicle loading, MRI of mice was taken, followed by euthanization by exsanguination under anesthesia with isoflurane. Five mice from each group were used.

2.4. Magnetic Resonance Imaging of Hepatic Iron Stores. Mice were anesthetized by exposure to isoflurane and maintained under anesthesia during the experiment. Magnetic resonance images were acquired using an MRI system (Agilent, Santa Clara, CA, USA) for collecting and analyzing parametric maps of the mouse liver at 7T (300 MHz). Breathing rate was monitored by the scanner with a pressure sensitive respiratory monitor (SA Instruments, Stony Brook, NY). To avoid respiratory-related motion artifacts, isoflurane levels were modulated as necessary to maintain the respiratory rate at 30 ± 10 breaths per minute. Proton-density-weighted images were acquired using a fast spin-echo multislice sequence (TR = 1500 ms, TE = 10 ms, echo train length = 8, kzero = 1, 128×128 matrix, field-of-view (FOV) = 40×40 mm, thickness = 1 mm). For the quantification of T1 values, we used an inversion recovery gradient echo multislice sequence which allowed the acquisition of a single T1 map (TR = 4.64 ms, TE = 1.96 ms, inversion recovery time = 0.1, 1.075, 2.05, 3.025, 4.0 s, flip angle 10°, 64×64 matrix, FOV = 40×40 mm, thickness = 2 mm). T2 values were obtained using a fast spin-echo multislice sequence (TR = 1500 ms, TE = 8, 11, 16, 22 ms, echo spacing = 8.35 ms, kzero = 1, 128×128 matrix, FOV = 40×40 mm, thickness = 2 mm). T2* values were obtained using gradient echo multislice sequence (TR = 100 ms, TE = 3, 5, 8, 12 ms, flip angle 20°, 128×128 matrix, FOV = 40×40 mm, thickness = 2 mm). Images were analyzed using VnmrJ software (Agilent) whereby T1 and T2, T2* parameter maps were calculated from acquired images. The relaxation rate was calculated as follows: R1 = 1/T1, R2 = 1/T2, and $R2^* = 1/T2^*$.

2.5. Specimen Collection. Blood was collected and divided into two aliquots. The first aliquot was collected into Minicollect ethylenediaminetetraacetic acid tubes (Greiner Bio-One, Kremsmünster, Austria). The second aliquot was collected into evacuated blood-collecting tubes (Terumo Corporation, Tokyo, Japan), and serum was isolated according to the manufacturer's instructions. Part of the liver was harvested for histological analysis and fixed in 10% neutral buffered formalin. The remaining part of the liver was used for iron content analysis.

2.6. Measurement of Hematological and Iron Indices in the Blood. Hematological indices were measured by an automated hematology analyzer (XT-2000iV; Sysmex, Hyogo, Japan). Serum iron levels as well as unsaturated iron binding capacity (UIBC) and total iron binding capacity (TIBC) were measured using an automatic biochemistry analyzer (TBA-120FR, Toshiba Medical Systems, Tochigi, Japan). Serum hepcidin

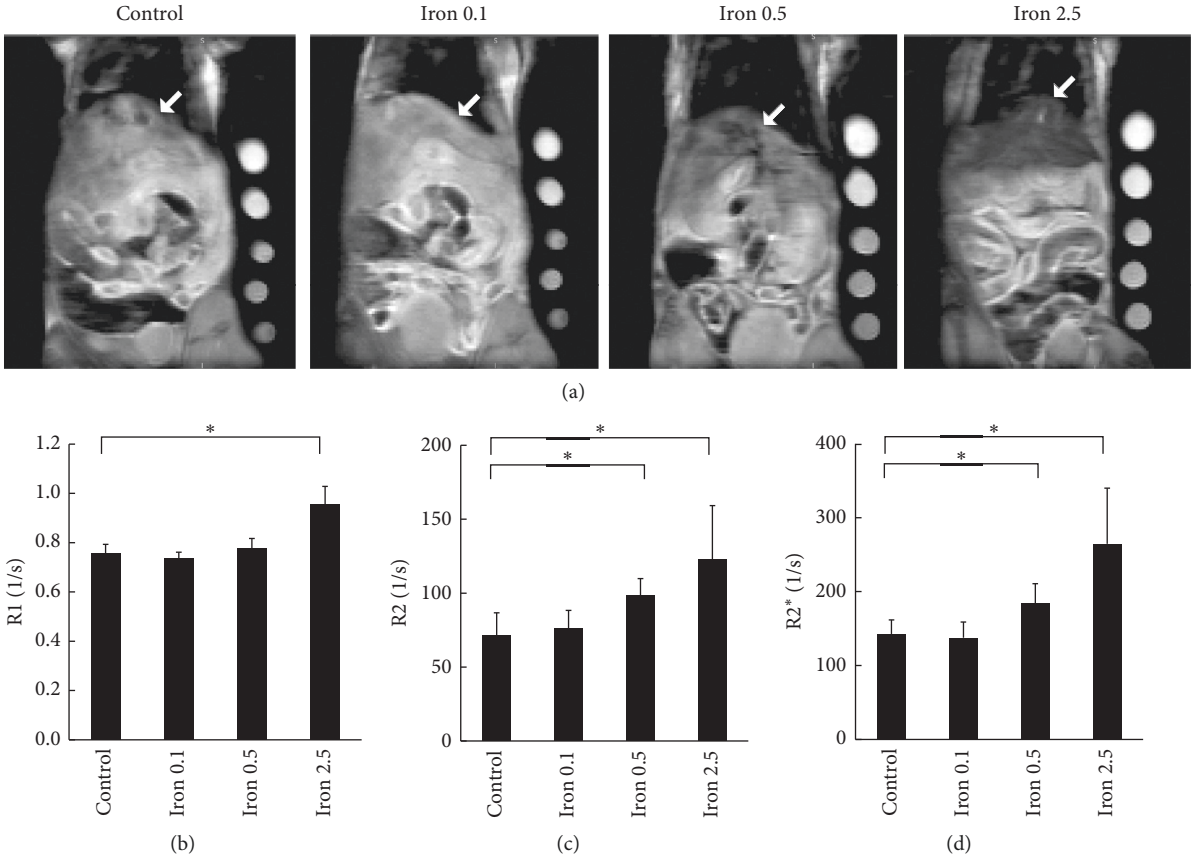

Figure 1: (a) Representative proton-density-weighted images of livers (indicated by white arrow) on Day 3 after administration of iron-dextran or dextran (control = dextran; Iron 0.1 = 0.1 mg iron-dextran/mouse; Iron 0.5 = 0.5 mg iron-dextran/mouse; Iron 2.5 = 2.5 mg iron-dextran/mouse). (b) R1, (c) R2, and (d)R2* of MRI of livers on Day 3 after administration of iron-dextran or dextran (control = dextran; Iron 0.1 = 0.1 mg iron-dextran/mouse; Iron 0.5 = 0.5 mg iron-dextran/mouse; Iron 2.5 = 2.5 mg iron-dextran/mouse). Results are expressed as mean + SD. Five mice from each group were used. Statistical significances were analyzed by Dunnett's test. $^*P < 0.05$.

level was measured by liquid chromatography/electrospray ionization tandem mass spectrometry using an AB Sciex Triple Quad 5500 system (AB Sciex, Foster City, CA, USA) equipped with a Prominence UFLCXR system (Shimadzu Corporation, Kyoto, Japan) as reported previously [11]. Serum ferritin levels were determined by ELISA kit (ALPCO, Salem, NH, USA).

2.7. Measurement of Iron Content in Liver. Liver samples were first dissolved in nitric acid and decomposed by heating. Iron concentrations were then measured by inductively coupled plasma-atomic emission spectrometry (ICP-AES, Yagai-Kagaku Co., Sapporo, Japan).

2.8. Histopathology. Sections (4 μm thick) were prepared from paraffin-embedded formalin-fixed liver samples. Liver hemosiderin deposition was assessed by Berlin blue staining.

2.9. Statistical Analysis. All values are shown as mean and standard deviation (SD). Statistical analysis was performed using JMP version 11.2.1 software (SAS Institute, Cary, NC, USA). Comparisons between groups were assessed by Dunnett's test. A P value of less than 0.05 was used to estimate statistical significance. Linear approximation and correlation coefficients were also analyzed.

3. Results

3.1. Noninvasive MRI Analysis of Liver Iron Storage. We used MRI to assess liver iron storage in 4 groups with different body iron status: the control group and the 0.1, 0.5, and 2.5 mg iron-dextran loaded groups. Representative proton-density-weighted images are shown in Figure 1(a). Mean R1, R2, and R2* are shown in Figures 1(b)–1(d), respectively. The R1 could detect the difference between the control group and the group loaded with 2.5 mg of iron-dextran. The R2 and R2* could detect the difference between the control group and the group loaded with 0.5 mg of iron-dextran as well as the difference between the control group and the group loaded with 2.5 mg of iron-dextran.

3.2. Invasive Analysis of Iron Parameters in Serum and Liver Samples. Specimens were collected to evaluate a variety of iron parameters such as hemosiderin deposition in the liver, liver iron content, serum hepcidin levels, and serum ferritin levels. Representative images of hemosiderin deposition visualized by Berlin blue staining are shown in Figure 2(a).

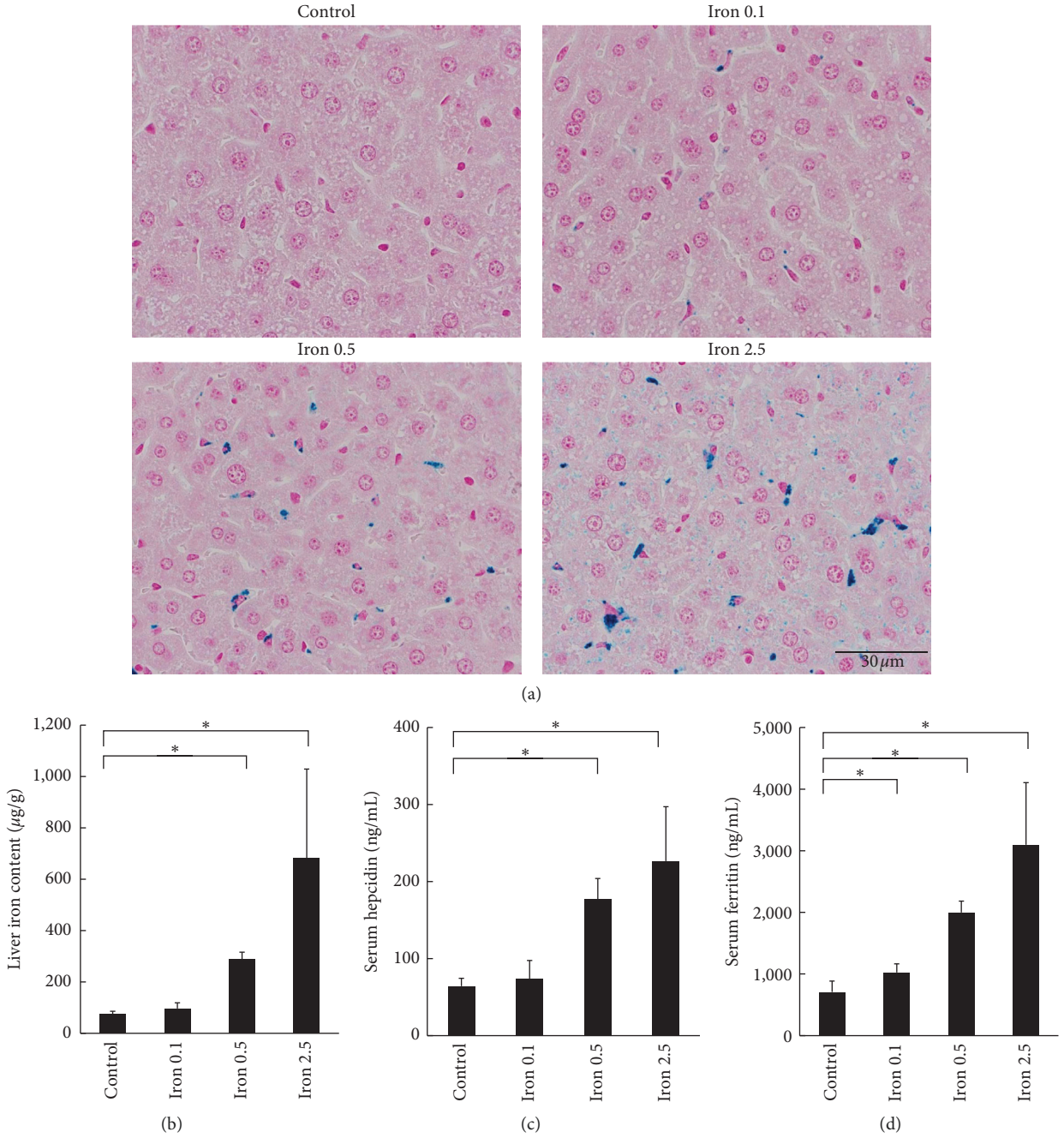

FIGURE 2: (a) Histopathological analysis for hepatic hemosiderin deposition in iron-loaded mice on Day 3 after administration of iron-dextran or dextran (control = dextran; Iron 0.1 = 0.1 mg iron-dextran/mouse; Iron 0.5 = 0.5 mg iron-dextran/mouse; Iron 2.5 = 2.5 mg iron-dextran/mouse). (b) Liver iron content, (c) serum hepcidin levels, and (d) serum ferritin levels on Day 3 after administration of iron-dextran or dextran (control = dextran; Iron 0.1 = 0.1 mg iron-dextran/mouse; Iron 0.5 = 0.5 mg iron-dextran/mouse; Iron 2.5 = 2.5 mg iron-dextran/mouse). Results are expressed as mean + SD. Five mice from each group were used. Statistical significances were analyzed by Dunnett's test. $^*P < 0.05$.

As were shown by the R1, R2, and R2* obtained from MRI, hemosiderin deposition tended to increase with iron loading dose. Liver iron content (Figure 2(b)) and serum hepcidin levels (Figure 2(c)) could detect the difference between the 0.5 mg iron-dextran loading group and the control group. Serum ferritin levels (Figure 2(d)) could detect the difference between the 0.1 mg iron-dextran loading group and the control group. On the other hand, hematological parameters and serum iron concentration were not increased by these levels of iron loading (Table 1).

3.3. R2 and Serum Ferritin Level Were Correlated Most Strongly with Liver Iron Content among All Iron-Related Parameters.* To investigate how well each indicator reflected body iron storage in each iron-loading model, correlation

Table 1: Hemoglobin levels and iron indices in the blood on Day 3 after administration of iron-dextran or dextran (control = dextran group; Iron 0.1 = 0.1 mg iron-dextran/mouse; Iron 0.5 = 0.5 mg iron-dextran/mouse; Iron 2.5 = 2.5 mg iron-dextran/mouse).

	Control	Iron 0.1	Iron 0.5	Iron 2.5
Hemoglobin (g/dL)	15.0 ± 1.1	15.3 ± 1.6	15.8 ± 1.5	14.3 ± 0.6
Serum iron (μg/dL)	152.8 ± 42.7	182.8 ± 46.8	143.6 ± 27.2	184.6 ± 22.0
UIBC (μg/dL)	120.0 ± 13.0	121.8 ± 22.2	140.8 ± 24.3	130.6 ± 30.4
TIBC (μg/dL)	272.8 ± 35.7	304.6 ± 45.8	284.4 ± 26.9	315.2 ± 27.2

Mean ± SD ($n = 5$); UIBC, unsaturated iron binding capacity; TIBC, total iron binding capacity.

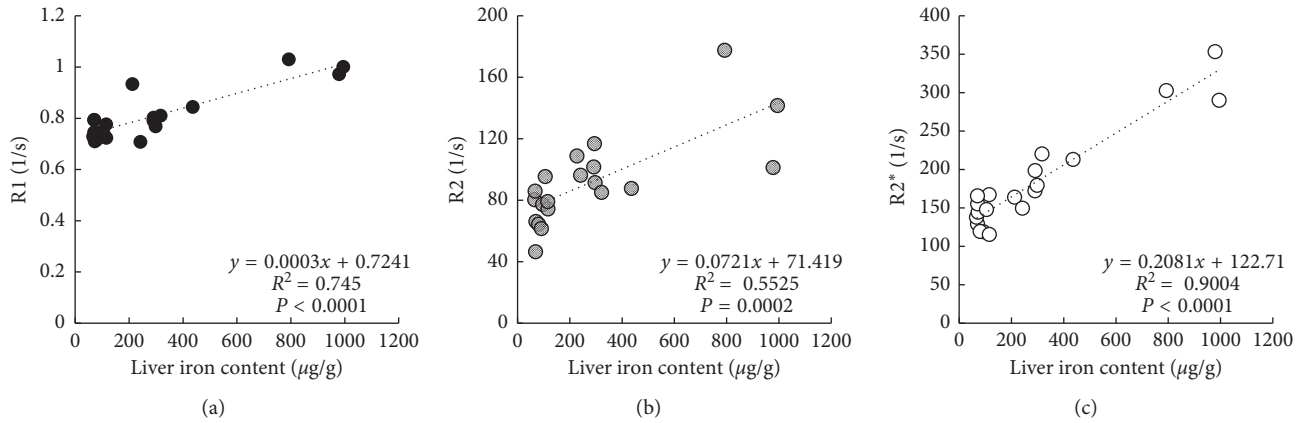

Figure 3: Correlations of (a) R1 value obtained from MRI of liver *vs.* liver iron content, (b) R2 value obtained from MRI of liver *vs.* liver iron content, and (c) R2* value obtained from MRI of liver *vs.* liver iron content.

analyses between liver iron content and all other iron-related parameters were conducted. Analysis of the R1, R2, and R2* (Figures 3(a)–3(c)) revealed that the R2* was the MRI parameter that correlated most highly with liver iron content ($R^2 = 0.9004$). Among the invasive iron-related parameters (Figures 4(a) and 4(b)), serum ferritin levels were most strongly correlated with liver iron content ($R^2 = 0.9281$). According to these comparison studies, as a noninvasive parameter, the T2* relaxation time obtained from MRI of the liver is an effective indicator of body iron status, and as an invasive parameter, serum ferritin level is also an effective indicator of body iron status.

4. Discussion

As shown in iron-overload disorders such as hemochromatosis and β-thalassemia, excess iron is detrimental to the body [4, 12]. To monitor body iron status in people with these conditions, serum ferritin and hepcidin are generally used as biomarkers for iron storage. However, it is difficult to assess body iron storage in patients with inflammation or infection because several inflammatory cytokines are produced under such conditions and iron-related parameters such as serum ferritin and hepcidin are influenced by such factors. A typical example of dysregulated iron metabolism is CKD. In patients with renal failure, damaged kidneys cannot produce adequate erythropoietin, a humoral factor promoting proliferation and maturation of erythroid cells, and consequently hemoglobin synthesis is downregulated. This leads to an increase in stored iron. In some patients with CKD, iron metabolism is further complicated because of inflammatory status [13, 14]. To make matters worse, one of the therapeutic approaches for renal anemia is iron supplementation. To evade the risk of excess iron accumulation, it is crucial to make use of an iron storage indicator that reflects body iron storage simply and accurately. An appropriate marker for body iron storage is necessary not only for patients with CKD but for all patients with dysregulated iron metabolism to evade the risk of tissue damage evoked by excess iron.

To select an appropriate indicator of body iron storage, we evaluated noninvasively and invasively measured iron-related parameters in mice loaded with different dosages of iron-dextran. Among the parameters evaluated, the MRI-derived T2* relaxation time as a noninvasive parameter and serum ferritin level as an invasive parameter were shown to be relatively accurate indicators of body iron storage. Moreover, serum ferritin level was the most sensitive indicator of body iron storage because this was the only parameter that could detect the difference between the control group and the group administered 0.1 mg iron-dextran/mouse. Although serum ferritin level is an accurate and sensitive indicator of body iron storage, this parameter is known to be influenced by inflammatory status [15]. Moreover, even under normal conditions, mouse serum ferritin levels are quite high compared with human levels. Therefore, when considering application to humans, serum ferritin level is not always optimal as an index of body iron storage. Among circulating iron-related parameters, serum iron was not associated with the dosage of iron-dextran (Table 1), and therefore it was considered to be inappropriate as an index of iron storage. On the other hand, the

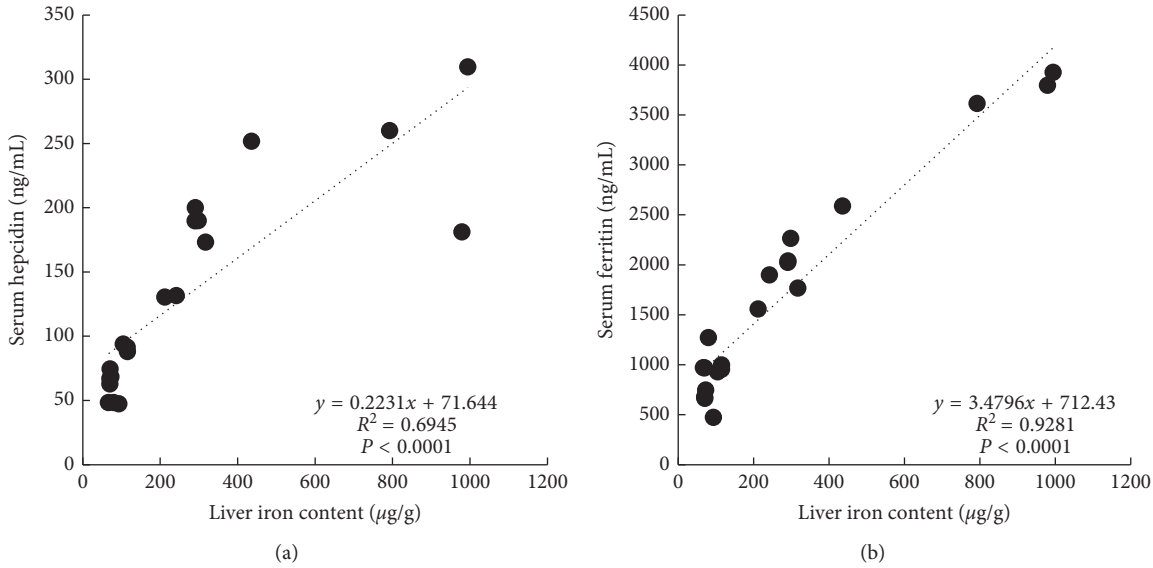

Figure 4: Correlations of (a) serum hepcidin level *vs.* liver iron content and (b) serum ferritin level vs. liver iron content.

MRI-derived T2* relaxation time is not only a sensitive indicator of body iron storage but is also a parameter that can be measured noninvasively. Taking into account its accuracy and its capability to assess changes in body iron storage over time, we concluded that the MRI-derived T2* relaxation time is the most appropriate indicator for assessing body iron storage. This parameter is known to be appropriate for measuring the paramagnetic effect of iron in the clinical setting [16], which supports the superiority of T2* relaxation time in assessing liver iron concentration in a murine model of iron overload.

The spleen is another iron storage organ. We evaluated T2* relaxation time of the spleen as well as the liver and analyzed its correlation with spleen iron content. However, the T2* relaxation time could not accurately evaluate spleen iron content because the tissue composition of the spleen was incompatible with MRI measurement (data not shown).

Among the several types of iron overload model, iron loading by administration of iron-dextran can be regarded as a model for secondary hemochromatosis. Because parenteral iron supplementation is the simplest and easiest way to achieve predetermined iron storage levels, research on secondary hemochromatosis is expected to be accelerated even without the use of genetically modified mice. Moreover, by using the T2* relaxation time obtained from MRI, it is possible to assess body iron status in the model prior to the study and during the study without sacrifice. In the clinical setting, the association between iron storage and tissue damage has not been adequately elucidated yet. The combination of a murine parenteral iron loading model and iron assessment by MRI could help us study the pathology of dysregulated iron metabolism.

In summary, it is shown that MRI designed for small animals is helpful for assessing body iron status in mice, and from among several iron-related parameters, the T2* relaxation time obtained from MRI could detect iron storage sensitively and accurately. Therefore, it is possible to conduct research on iron metabolism in mice to a greater depth than ever before. However, it remains a challenge to take the findings from research on iron metabolism in mice and apply them in the clinical setting. To confirm that iron-related indices in mice are applicable to humans, invasive and noninvasive indices associated with iron metabolism need to be investigated in both mice and humans.

Data Availability

The data used to support the findings of this study were provided by Chugai Pharmaceutical Co., Ltd., under license and so cannot be made freely available. Access to these data will be considered by the corresponding author upon request, with the permission of Chugai Pharmaceutical Co., Ltd.

Conflicts of Interest

The authors declare that they have no competing interests.

Acknowledgments

We thank Mrs. Yuki Omori and Ms. Asami Yoshioka for their technical assistance in collecting specimens.

References

[1] S. J. Dixon and B. R. Stockwell, "The role of iron and reactive oxygen species in cell death," *Nature Chemical Biology*, vol. 10, no. 1, pp. 9–17, 2014.

[2] C. A. Worthen and C. A. Enns, "The role of hepatic transferrin receptor 2 in the regulation of iron homeostasis in the body," *Frontiers in Pharmacology*, vol. 5, p. 34, 2014.

[3] K. Lagergren, K. Wahlin, F. Mattsson, D. Alderson, and J. Lagergren, "Haemochromatosis and gastrointestinal cancer," *International Journal of Cancer*, vol. 139, no. 8, pp. 1740–1743, 2016.

[4] L. W. Powell, R. C. Seckington, and Y. Deugnier, "Haemochromatosis," *The Lancet*, vol. 388, pp. 706–716, 2016.
[5] T. Ganz and E. Nemeth, "Iron homeostasis in host defence and inflammation," *Nature Reviews Immunology*, vol. 15, no. 8, pp. 500–510, 2015.
[6] K. Zumbrennen-Bullough and J. L. Babitt, "The iron cycle in chronic kidney disease (CKD): from genetics and experimental models to CKD patients," *Nephrology, Dialysis, Transplantation*, vol. 29, no. 2, pp. 263–273, 2014.
[7] E. Nemeth, S. Rivera, V. Gabayan et al., "IL-6 mediates hypoferremia of inflammation by inducing the synthesis of the iron regulatory hormone hepcidin," *The Journal of Clinical Investigation*, vol. 113, no. 9, pp. 1271–1276, 2004.
[8] P. Kanwar and K. V. Kowdley, "Diagnosis and treatment of hereditary hemochromatosis: an update," *Expert Review of Gastroenterology & Hepatology*, vol. 7, no. 6, pp. 517–530, 2013.
[9] J. B. Wish, "Assessing iron status: beyond serum ferritin and transferrin saturation," *Clinical Journal of the American Society of Nephrology: CJASN*, vol. 1, no. Suppl 1, pp. S4–S8, 2006.
[10] L. J. Anderson, "Assessment of iron overload with T2* magnetic resonance imaging," *Progress in Cardiovascular Diseases*, vol. 54, no. 3, pp. 287–294, 2011.
[11] N. Murao, M. Ishigai, H. Yasuno, Y. Shimonaka, and Y. Aso, "Simple and sensitive quantification of bioactive peptides in biological matrices using liquid chromatography/selected reaction monitoring mass spectrometry coupled with trichloroacetic acid clean-up," *Rapid Communications in Mass Spectrometry: RCM*, vol. 21, no. 24, pp. 4033–4038, 2007.
[12] A. Liaska, P. Petrou, C. D. Georgakopoulos et al., "beta-Thalassemia and ocular implications: a systematic review," *BMC Ophthalmology*, vol. 16, no. 1, 2016.
[13] S. A. Antunes and M. E. Canziani, "Hepcidin: an important iron metabolism regulator in chronic kidney disease," *Jornal Brasileiro de Nefrologia*, vol. 38, no. 3, pp. 351–355, 2016.
[14] L. Mercadal, M. Metzger, J. P. Haymann et al., "The relation of hepcidin to iron disorders, inflammation and hemoglobin in chronic kidney disease," *PloS One*, vol. 9, no. 6, Article ID e99781, 2014.
[15] D. B. Kell and E. Pretorius, "Serum ferritin is an important inflammatory disease marker, as it is mainly a leakage product from damaged cells," *Metallomics: Integrated Biometal Science*, vol. 6, no. 4, pp. 748–773, 2014.
[16] Y. Gandon, D. Olivié, D. Guyader et al., "Non-invasive assessment of hepatic iron stores by MRI," *The Lancet*, vol. 363, no. 9406, pp. 357–362, 2004.

Hindawi
Contrast Media & Molecular Imaging
Volume 2019, Article ID 1510507, 7 pages
https://doi.org/10.1155/2019/1510507

Review Article

A Window on the Lung: Molecular Imaging as a Tool to Dissect Pathophysiologic Mechanisms of Acute Lung Disease

Guido Musch

Department of Anesthesiology, Washington University in St. Louis, St. Louis, MO 63110, USA

Correspondence should be addressed to Guido Musch; guidomusch@wustl.edu

Received 23 January 2019; Accepted 8 May 2019; Published 25 August 2019

Guest Editor: Svend B. Jensen

In recent years, imaging has given a fundamental contribution to our understanding of the pathophysiology of acute lung diseases. Several methods have been developed based on computed tomography (CT), positron emission tomography (PET), and magnetic resonance (MR) imaging that allow regional, in vivo measurement of variables such as lung strain, alveolar size, metabolic activity of inflammatory cells, ventilation, and perfusion. Because several of these methods are noninvasive, they can be successfully translated from animal models to patients. The aim of this paper is to review the advances in knowledge that have been accrued with these imaging modalities on the pathophysiology of acute respiratory distress syndrome (ARDS), ventilator-induced lung injury (VILI), asthma and chronic obstructive pulmonary disease (COPD).

1. Introduction

Since the first chest X-ray, lung imaging has focused, for the most part, on detecting structural alterations of lung anatomy due to pulmonary diseases, usually inferred from abnormalities in the distribution of lung density, or changes in lung metabolism, predominantly glucose metabolism, in the diagnosis and monitoring of lung cancer with positron emission tomography (PET).

In recent years, however, there has been a tremendous growth of methods that leverage imaging to elucidate pathophysiologic mechanisms of acute lung disease. Because several of these imaging methods are noninvasive, many have been successfully translated from initial studies in animals to humans. This has allowed for a better understanding of how certain acute lung conditions develop as well as identification of which animal species, size, and injury models are most appropriate for translatability of the experimental results to the human scenario, depending on the specific condition or mechanism being investigated.

The aim of this review is to highlight a sample of acute pulmonary conditions for which imaging of experimental models has enabled substantial progress in the understanding of their pathophysiology, with a specific focus on the contributions of PET. Major relative strengths and weaknesses of the three imaging modalities discussed in this review are presented in Table 1.

2. Acute Respiratory Distress Syndrome (ARDS) and Ventilator-Induced Lung Injury (VILI)

2.1. Imaging of Pulmonary Density, Mechanics, and Inflammation. Because one of the defining features of ARDS is bilateral radiographical lung opacities, it is not surprising that imaging has played a major role in elucidating the pathophysiology of this syndrome. The current prevailing theory is that these opacities result from two main factors: (a) surfactant dysfunction [1], leading to increased surface tension at the alveolar lining and thus favoring edema and alveolar collapse and (b) the effect of gravity on the ARDS lung, with the lung's dependent portions being compressed by the weight of the overlying edema fluid [2]. Because such gravitational effect is proportional to lung height and density, animal models that reproduce this effect must have lung size and physiology similar to the human. Consequently, many studies were done in large animals such as sheep, dogs, or pigs. Although no single animal model reproduces all the complex features of ARDS pathophysiology,

Table 1: Main strengths and weakness of CT, PET, and MR for functional lung imaging.

	Strengths	Weaknesses
CT	High spatial resolution Speed of acquisition	Radiation exposure Limited ability to image biologic processes
PET	Image biologic processes Tracer kinetic modeling	Radiation exposure Lower spatial resolution
MR	High spatial resolution Radiation free	Requires hyperpolarized gases to image ventilation Limited ability to image biologic processes

some established models of ARDS have been developed to reproduce its most salient features, particularly noncardiogenic pulmonary edema. These models include (1) oleic acid injection, in which oleic acid, infused through a central vein, damages the alveolocapillary membrane, thus increasing its permeability and leading to alveolar flooding [3]; (2) lung lavage, in which surfactant is depleted by repeated saline lavage, leading to unstable alveolar mechanics and development of atelectasis and edema because of increased surface tension [4]; and (3) injurious mechanical ventilation, in which high tidal volumes are used to mechanically damage the lung, leading to edema and hyaline membrane formation resembling the condition of VILI, which frequently coexists with ARDS [5–8]. Lung lavage and injurious mechanical ventilation can be combined in a "two-hit" injury model in which VILI worsens preexisting surfactant dysfunction [9].

Imaging studies performed in these animal models, mainly employing computed tomography (CT), supported the concept that, in the heterogeneously inflated ARDS lung, there is a range of opening pressures for derecruited (i.e., nonaerated) alveoli. Such pressure depends on the position of the alveolus along the gravitational axis [2], on the radius of curvature and the surface tension at the air-liquid interface, and on the energy required to fracture liquid bridges that obstruct small airways [10, 11]. By applying pressure at the airway to overcome alveolar opening pressures, either through positive end-expiratory pressure (PEEP) or recruitment maneuvers, or by changing the distribution of such pressures through prone positioning, airspaces can be recruited and lung ventilation and perfusion-to-ventilation matching restored in regions that were derecruited [12, 13]. Consequently, the first major contribution of tomographic imaging studies in animal models of ARDS is to elucidate the regional mechanism by which interventions that aim to recruit alveoli, and thus restore aeration and gas exchange, exert their beneficial effect.

CT and PET have also been used to measure the strain imposed by mechanical ventilation on different parts of the lung. Tidal lung strain is defined as the change in volume of a given region of the lung between expiration and inspiration, relative to its volume at end expiration. Strain is a key biophysical determinant of VILI. Regional tidal strain can be measured with PET imaging of inhaled [^{13}N]nitrogen ($^{13}N_2$), by gating frame acquisition of the equilibrated tracer concentration with the end-inspiratory and end-expiratory phases. When a region of the lung expands, its gas content and hence the $^{13}N_2$ concentration measured by PET increase. Thus, the change in regional tracer concentration is related to regional strain [14]. CT can measure regional tidal strain in a conceptually similar manner by measuring density changes between expiration and inspiration [15, 16] or by using registration algorithms to calculate the deformation of a given region of the lung between expiration and inspiration through a three-dimensional warping function [17].

When combined with PET imaging of 2-[^{18}F]fluoro-2-deoxy-D-glucose ([^{18}F]FDG) as a means to measure metabolic activation of inflammatory cells induced by mechanical ventilation [18, 19], PET/CT studies have shown that inflammation prevails in lung regions that are atelectatic or that become exposed to the largest cyclical tidal strain as the injury progresses [20, 21]. In fact, there appears to be a direct linear relationship between lung strain and [^{18}F]FDG phosphorylation rate (commonly denoted as k_3) [22], and [^{18}F]FDG uptake rate (commonly denoted as K_i) was increased in dependent regions of the surfactant depleted lungs, which are the regions expected to undergo repetitive collapse and reexpansion with tidal breathing [23, 24]. These findings in large animal models of VILI and ARDS have been paralleled by similar findings in patients, in whom PET/CT has revealed increased [^{18}F] FDG uptake both in dense regions, where atelectasis and inflammation due to the primary etiology of ARDS are expected to predominate, and in aerated regions exposed to the iatrogenic strain of mechanical ventilation either because of tidal overdistension or cyclical alveolar recruitment and derecruitment [25–27]. Recent evidence indeed suggests that lung regions that exhibit the greatest cyclical change in density with tidal volume at the start of a period of mechanical ventilation eventually become "injured" as defined by an increase of their density above −300 Hounsfield units [28]. Importantly, regions of the lung that present increased [^{18}F]FDG uptake on PET and/or CT abnormalities consistent with alterations of regional mechanical properties also reveal gene expression patterns indicative of activation of specific inflammatory pathways [20, 29]. Consequently, the second major contribution of imaging, in particular of combining the structural information derived from CT with the functional information derived from PET, is to provide mechanistic insight into the pathogenesis of VILI superimposed on ARDS and into the molecular pathways that underlie these conditions.

Recently, magnetic resonance (MR) techniques have been developed to assess geometrical and mechanical properties of the injured lungs [30, 31]. One such technique is based on the inhalation of hyperpolarized helium (^{3}He). Measurement of the apparent diffusion coefficient (ADC) of

^{3}He using diffusion-weighted hyperpolarized gas MR imaging yields estimates of airspace size. Using this technique, Cereda et al. [30] demonstrated that surfactant depletion by saline lavage is accompanied by an increase in alveolar size of airspaces that remain aerated, most likely as a result of distension due to parenchymal tethering to alveoli that become atelectatic. This observation suggests that alveolar derecruitment and overdistension coexist in different parts of the same lung for a given airway pressure. Application of PEEP and instillation of surfactant recruited atelectatic lung and decreased mean ADC, implying that they rendered the distribution of alveolar size more homogeneous. Another technique is based on the assessment of parenchymal elasticity by MR elastography [31].

PET imaging of pulmonary [^{18}F]FDG uptake has also been used to detect inflammation due to sepsis and smoke inhalation, conditions that are often associated with ARDS. Studies in large animal models of sepsis using endotoxin infusion have demonstrated that inflammation in regions of high mechanical ventilatory strain is amplified by endotoxin [22, 32] and that protective mechanical ventilation with high PEEP and low tidal volume decreases [^{18}F]FDG uptake in such regions [33], thus supporting the double-hit theory for the development of acute lung injury. In animal models of acute smoke inhalation, PET has been able to detect increased [^{18}F]FDG uptake (Figure 1) before alterations of pulmonary gas exchange became apparent, thus lending itself to being a potentially useful early diagnostic tool for smoke inhalation-associated ARDS [34].

Most recently, a transgenic PET reporter mouse model of smoke inhalation has been used to demonstrate activation of nuclear factor-kappa B (NF-κB) and expression of genes regulated by this transcription factor at 24 and 48 hours after acute smoke inhalation (Figure 2) [35]. Molecular imaging of endogenous gene expression requires manipulation of the animal's genome and is thus more commonly done in smaller animals, especially mice. In this technique, the herpes simplex virus thymidine kinase gene (HSV-tk) acts as the reporter transgene, inserted in the mouse genome under the control of a NF-κB sensitive promoter. When NF-κB is activated by an inflammatory stimulus, it translocates into the nucleus and activates transcription of all NF-κB regulated genes, including the HSV-tk reporter gene. The resultant reporter protein, HSV-TK, is an enzyme that phosphorylates the acycloguanosine analog 9-(4-[^{18}F] fluoro-3-[hydroxymethyl]butyl)guanine ([^{18}F]FHBG). [^{18}F] FHBG has two properties that make it suited for PET imaging: (1) it is a high-affinity substrate for the HSV1-TK enzyme but has relatively low affinity for mammalian thymidine kinase, resulting in improved detection sensitivity and reduced background noise [36]; (2) once phosphorylated, it is trapped inside the cell, where it accumulates proportionally to the level of HSV-tk gene expression and hence NF-κB activation. This PET imaging technique thus holds promise for elucidating the sequence of molecular and genetic events that lead to the inflammatory process of ARDS and VILI noninvasively and in vivo because the same subject can be studied at multiple time points over the evolution of the acute lung condition.

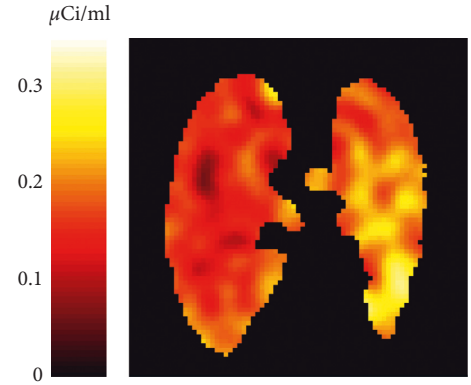

Figure 1: Positron emission tomography image representing pulmonary [^{18}F]FDG activity 4 hours after unilateral cotton smoke inhalation to the left lung of a sheep (positioned on the right side in the figure). Note higher activity in the smoke exposed than in the control lung. Reproduced from Musch et al (Reference [34]).

2.2. Imaging of Pulmonary Perfusion and Gas Exchange. In addition to development of inflammation and alterations in the distribution of lung density, ARDS is characterized by alterations in the regional distribution of perfusion. Several techniques have been developed to measure regional perfusion with PET in animal models and patients with ARDS. One technique is based on the intravenous administration of ^{15}O-water ($H_2{}^{15}O$) as the radiotracer [37]. Because $H_2{}^{15}O$ is freely diffusible in the lung, it rapidly equilibrates between the pulmonary blood and tissue such that the concentration of tracer in the pulmonary venous blood that flows out of a region is equal to the concentration of tracer in the tissue divided by the tissue-to-blood partition coefficient of the tracer (i.e., the tracer leaves the lung at equilibrium with lung tissue). By measuring regional lung activity with PET during $H_2{}^{15}O$ infusion and the subsequent equilibration phase, it is possible to calculate regional pulmonary blood flow from the equation that describes the one-compartment mathematical model of tracer distribution [37]. Regional lung water can be measured by normalizing lung tissue activity at equilibrium by the activity of blood water, measured from blood samples collected during the PET scan. Intravascular lung water can be calculated by taking a PET scan and measuring blood activity after inhalation of ^{11}C- or ^{15}O-carbon monoxide, which binds to hemoglobin with high affinity. Extravascular lung water can then be obtained by subtracting intravascular water from regional water. This technique thus allows determination of regional pulmonary blood flow and extravascular lung water (i.e., edema). In conditions characterized by increased pulmonary vascular permeability, such as ARDS, extravascular lung water is expected to increase [38]. A specific measure of pulmonary vascular permeability can also be derived with PET by measuring the pulmonary transcapillary escape rate of a radiolabeled protein, such as ^{68}Ga-transferrin or ^{11}C-methylalbumin, between the intravascular and the extravascular space [39].

Using the $H_2{}^{15}O$ technique, Gust et al. [40] demonstrated that perfusion redistributes away from dependent edematous lung regions in an oleic acid-induced canine

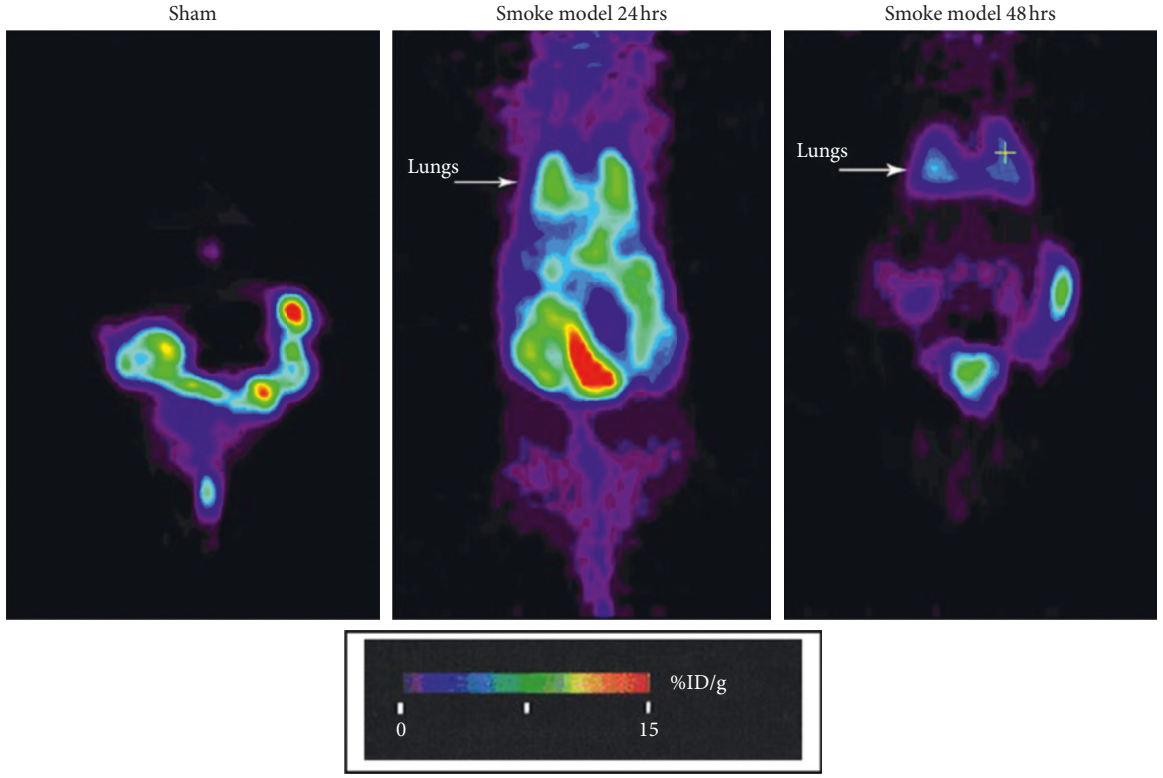

Figure 2: Micropositron emission tomographic image of 9-(4-[^{18}F]fluoro-3-[hydroxymethyl]butyl)guanine ([^{18}F]FHBG) activity in a herpes simplex virus thymidine kinase (HSV-tk) reporter mice after smoke inhalation injury. [^{18}F]FHBG activity is proportional to nuclear factor-kappa B (NF-κB)-mediated gene expression. The arrow indicates the location of the lungs. Note increased pulmonary NF-κB activation, and hence HSV-tk expression, at 24 and 48 hours after smoke inhalation. Reproduced from Syrkina et al. (Reference [35]).

model of ARDS. This redistribution acts as a homeostatic mechanism to preserve arterial oxygenation because pulmonary perfusion is diverted away from shunting regions. Administration of intravenous endotoxin abolished this redistribution of perfusion away from dependent edematous shunting regions, thus worsening oxygenation. Because endotoxin is known to blunt hypoxic pulmonary vasoconstriction, this experimental observation implies that vascular smooth muscle contraction was responsible for the observed perfusion redistribution toward nonedematous lung regions. Interestingly, studies in patients with ARDS using the $H_2{}^{15}O$ technique have also revealed lack of perfusion redistribution away from edematous regions [41], suggesting that hypoxic pulmonary vasoconstriction is, at least to some extent, impaired in ARDS, similarly to the experimental endotoxin studies. Redistribution of perfusion away from injured regions, similar to the oleic acid model, was instead demonstrated after unilateral endobronchial instillation of hydrochloric acid, a model for gastric aspiration, using PET of ^{68}Ga labeled microspheres to measure regional pulmonary perfusion in rats [42].

Another PET technique to measure regional pulmonary blood flow and gas exchange is based on the intravenous administration of $^{13}N_2$ in saline solution. A bolus of $^{13}N_2$ gas dissolved in 20–30 ml of saline solution is infused intravenously at the beginning of a 30- to 60-second apnea while the pulmonary kinetics of $^{13}N_2$ is measured by sequential PET frames. Because of the low solubility of nitrogen in blood and tissues (partition coefficient between water and air is 0.015), virtually all infused $^{13}N_2$ diffuses into the alveolar airspace of aerated alveoli at first pass, where it accumulates in proportion to regional perfusion [43]. However, if alveoli are perfused but not aerated, for example, because they are atelectatic or flooded with edema, $^{13}N_2$ kinetics shows an early peak of tracer activity, reflecting perfusion to that region, followed by an exponential decrease toward a plateau for the remainder of apnea. The magnitude of this decrease is proportional to regional shunt (Figure 3), and robust estimates of regional perfusion and shunt fraction can be derived by applying a mathematical model to the pulmonary kinetics of a $^{13}N_2$-saline bolus, measured by PET during apnea [12]. This technique has been applied in lavage models of ARDS to elucidate the pathophysiological basis for the clinical observation that recruitment maneuvers can, at times, paradoxically worsen oxygenation by diverting perfusion toward dependent shunting lung regions [44].

3. Airway Obstructive Disease

Because in the $^{13}N_2$-saline infusion technique the tracer is delivered to the alveolar airspace by perfusion rather than ventilation, this technique is ideally suited to quantify hypoventilation in regions of airway obstruction, which would not display a sufficient signal if delivery of tracer

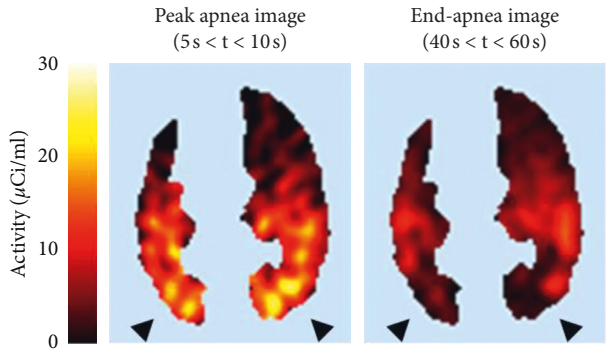

Figure 3: [^{13}N]nitrogen ($^{13}N_2$) positron emission tomography images from a sheep with lavage-induced lung injury. A bolus of $^{13}N_2$ in saline solution was infused intravenously over 3 seconds at the beginning of a 60-second apnea. The distribution of $^{13}N_2$ during early apnea (between 5 and 10 seconds) reflects regional perfusion (peak apnea image). The distribution of $^{13}N_2$ at the end of apnea (between 40 and 60 seconds) is proportional to perfusion only to aerated alveolar units, which retain $^{13}N_2$ during apnea (end-apnea image). The decrease in tracer activity between peak and end-apnea images in the dorsal, dependent lung (*arrowheads*) reflects the presence of shunt in this part of the lung because alveoli that are perfused but not aerated do not retain $^{13}N_2$ during apnea. Modified from Musch et al (Reference [12]).

occurred by inhalation, as commonly done with other imaging techniques to measure regional ventilation. This characteristic makes the $^{13}N_2$-saline infusion technique particularly attractive to study lung diseases characterized by bronchoconstriction.

When breathing is resumed after the end of apnea, specific alveolar ventilation (i.e., alveolar ventilation per unit of gas volume) can be calculated from the washout rate of $^{13}N_2$. In the presence of uniform ventilation, the washout of tracer is accurately described by a single compartment model, manifested by single exponential washout kinetics [43]. In contrast, in the presence of intraregional heterogeneity of ventilation, as is usually found in airway obstructive diseases such as asthma and chronic obstructive pulmonary disease (COPD), the washout kinetics is better described by a multicompartmental model, with a fast and a slow ventilating compartments that represent alveolar units with, respectively, normal ventilation and hypoventilation.

Using this multicompartmental model, Vidal Melo et al. [45] were able to derive ventilation-perfusion distributions from PET images of $^{13}N_2$ that allowed accurate estimation of blood gases in animal models of asthma by inhaled methacholine. The bimodality of these distributions during bronchoconstriction reflected hypoventilation of large contiguous regions of the lung [46], a finding that was confirmed in patients with asthma [47]. In these states, the fraction of lung volume presenting intraregional ventilation heterogeneity (i.e., multicompartmental $^{13}N_2$ washout kinetics) is substantial, in contrast to the predominant single compartment behavior of normal lungs [43].

The extreme case of hypoventilation is represented by airway closure leading to gas trapping distal to the occluded airway. Gas trapping regions will appear as regions of $^{13}N_2$ retention on PET frames acquired at the end of the washout phase. This characteristic has been leveraged to demonstrate that the prone position is effective in reducing areas of gas trapping in asthmatic subjects with induced bronchoconstriction [48].

Combined measurements of regional perfusion and ventilation in patients with COPD showed that both ventilation and perfusion are more heterogeneously distributed in COPD than in normal subjects. However, the heterogeneity of perfusion was greater than expected from the increase in ventilation heterogeneity and occurred predominantly at large length scales, suggesting that perfusion heterogeneity could serve as an early biomarker of pulmonary vascular involvement in COPD [49].

4. Conclusion

In recent years, pulmonary structural and functional imaging techniques based on CT, PET, and MR have been applied to animal models of ARDS (oleic acid infusion and saline lung lavage), sepsis (endotoxin infusion), VILI (high tidal volume mechanical ventilation), and asthma (methacholine inhalation), yielding fundamental progress in our understanding of the pathophysiology of these conditions. Because of their noninvasive nature, several of these techniques can be translated to the corresponding human condition, thus enhancing the clinical relevance of these animal studies.

Conflicts of Interest

The author declares that there are no conflicts of interest regarding the publication of this article.

Acknowledgments

This work was supported by the National Institutes of Health, Bethesda, Maryland (grant number R01HL094639).

References

[1] R. G. Spragg and R. M. Smith, "Pathology of the surfactant system of the mature lung," *American Journal of Respiratory and Critical Care Medicine*, vol. 155, no. 2, pp. 756–760, 1997.

[2] L. Gattinoni, L. D'Andrea, P. Pelosi, G. Vitale, A. Pesenti, and R. Fumagalli, "Regional effects and mechanism of positive end-expiratory pressure in early adult respiratory distress syndrome," *Journal of the American Medical Association*, vol. 269, no. 16, pp. 2122–2127, 1993.

[3] M. A. Martynowicz, T. A. Minor, B. J. Walters, and R. D. Hubmayr, "Regional expansion of oleic acid-injured lungs," *American Journal of Respiratory and Critical Care Medicine*, vol. 160, no. 1, pp. 250–258, 1999.

[4] B. Lachmann, B. Robertson, and J. Vogel, "In vivo lung lavage as an experimental model of the respiratory distress syndrome," *Acta Anaesthesiologica Scandinavica*, vol. 24, no. 3, pp. 231–236, 1980.

[5] H. H. Webb and D. F. Tierney, "Experimental pulmonary edema due to intermittent positive pressure ventilation with high inflation pressures: protection by positive end-expiratory

pressure," *American Review of Respiratory Disease*, vol. 110, no. 5, pp. 556–565, 1974.

[6] D. Dreyfuss, G. Basset, P. Soler, and G. Saumon, "Intermittent positive-pressure hyperventilation with high inflation pressures produces pulmonary microvascular injury in rats," *American Review of Respiratory Disease*, vol. 132, no. 4, pp. 880–884, 1985.

[7] K. Tsuno, P. Prato, and T. Kolobow, "Acute lung injury from mechanical ventilation at moderately high airway pressures," *Journal of Applied Physiology*, vol. 69, no. 3, pp. 956–961, 1990.

[8] K. Tsuno, K. Miura, M. Takeya, T. Kolobow, and T. Morioka, "Histopathologic pulmonary changes from mechanical ventilation at high peak airway pressures," *American Review of Respiratory Disease*, vol. 143, no. 5, pp. 1115–1120, 1991.

[9] V. Taskar, J. John, E. Evander, B. Robertson, and B. Jonson, "Surfactant dysfunction makes lungs vulnerable to repetitive collapse and reexpansion," *American Journal of Respiratory and Critical Care Medicine*, vol. 155, no. 1, pp. 313–320, 1997.

[10] R. D. Hubmayr, "Perspective on lung injury and recruitment: a skeptical look at the opening and collapse story," *American Journal of Respiratory and Critical Care Medicine*, vol. 165, no. 12, pp. 1647–1653, 2002.

[11] R. D. Hubmayr, "Another look at the opening and collapse story," *Critical Care Medicine*, vol. 37, no. 9, pp. 2667-2668, 2009.

[12] G. Musch, G. Bellani, M. F. Vidal Melo et al., "Relation between shunt, aeration, and perfusion in experimental acute lung injury," *American Journal of Respiratory and Critical Care Medicine*, vol. 177, no. 3, pp. 292–300, 2008.

[13] T. Richter, G. Bellani, R. S. Harris et al., "Effect of prone position on regional shunt, aeration, and perfusion in experimental acute lung injury," *American Journal of Respiratory and Critical Care Medicine*, vol. 172, no. 4, pp. 480–487, 2005.

[14] T. J. Wellman, T. Winkler, E. L. V. Costa et al., "Measurement of regional specific lung volume change using respiratory-gated PET of inhaled 13N-nitrogen," *Journal of Nuclear Medicine*, vol. 51, no. 4, pp. 646–653, 2010.

[15] M. K. Fuld, R. B. Easley, O. I. Saba et al., "CT-measured regional specific volume change reflects regional ventilation in supine sheep," *Journal of Applied Physiology*, vol. 104, no. 4, pp. 1177–1184, 2008.

[16] L. F. Paula, T. J. Wellman, T. Winkler et al., "Regional tidal lung strain in mechanically ventilated normal lungs," *Journal of Applied Physiology*, vol. 121, no. 6, pp. 1335–1347, 2016.

[17] D. W. Kaczka, K. Cao, G. E. Christensen, J. H. T. Bates, and B. A. Simon, "Analysis of regional mechanics in canine lung injury using forced oscillations and 3D image registration," *Annals of Biomedical Engineering*, vol. 39, no. 3, pp. 1112–1124, 2011.

[18] D. L. Chen and D. P. Schuster, "Positron emission tomography with [^{18}F]fluorodeoxyglucose to evaluate neutrophil kinetics during acute lung injury," *American Journal of Physiology-Lung Cellular and Molecular Physiology*, vol. 286, no. 4, pp. L834–L840, 2004.

[19] G. Musch, J. G. Venegas, G. Bellani et al., "Regional gas exchange and cellular metabolic activity in ventilator-induced lung injury," *Anesthesiology*, vol. 106, no. 4, pp. 723–735, 2007.

[20] G. C. Motta-Ribeiro, S. Hashimoto, T. Winkler et al., "Deterioration of regional lung strain and inflammation during early lung injury," *American Journal of Respiratory and Critical Care Medicine*, vol. 198, no. 7, pp. 891–902, 2018.

[21] J. Retamal, D. Hurtado, N. Villarroel et al., "Does regional lung strain correlate with regional inflammation in acute respiratory distress syndrome during nonprotective ventilation? An experimental porcine study," *Critical Care Medicine*, vol. 46, no. 6, pp. e591–e599, 2018.

[22] T. J. Wellman, T. Winkler, E. L. V. Costa et al., "Effect of local tidal lung strain on inflammation in normal and lipopolysaccharide-exposed sheep," *Critical Care Medicine*, vol. 42, no. 7, pp. e491–e500, 2014.

[23] N. de Prost, E. L. Costa, T. Wellman et al., "Effects of surfactant depletion on regional pulmonary metabolic activity during mechanical ventilation," *Journal of Applied Physiology*, vol. 111, no. 5, pp. 1249–1258, 2011.

[24] N. de Prost, Y. Feng, T. Wellman et al., "^{18}F-FDG kinetics parameters depend on the mechanism of injury in early experimental acute respiratory distress syndrome," *Journal of Nuclear Medicine*, vol. 55, no. 11, pp. 1871–1877, 2014.

[25] G. Bellani, C. Messa, L. Guerra et al., "Lungs of patients with acute respiratory distress syndrome show diffuse inflammation in normally aerated regions: a [^{18}F]-fluoro-2-deoxy-D-glucose PET/CT study," *Critical Care Medicine*, vol. 37, no. 7, pp. 2216–2222, 2009.

[26] G. Bellani, L. Guerra, G. Musch et al., "Lung regional metabolic activity and gas volume changes induced by tidal ventilation in patients with acute lung injury," *American Journal of Respiratory and Critical Care Medicine*, vol. 183, no. 9, pp. 1193–1199, 2011.

[27] M. Cressoni, D. Chiumello, C. Chiurazzi et al., "Lung inhomogeneities, inflation and [^{18}F]2-fluoro-2-deoxy-D-glucose uptake rate in acute respiratory distress syndrome," *European Respiratory Journal*, vol. 47, no. 1, pp. 233–242, 2016.

[28] M. Cereda, Y. Xin, H. Hamedani et al., "Tidal changes on CT and progression of ARDS," *Thorax*, vol. 72, no. 11, pp. 981–989, 2017.

[29] T. J. Wellman, N. de Prost, M. Tucci et al., "Lung metabolic activation as an early biomarker of acute respiratory distress syndrome and local gene expression heterogeneity," *Anesthesiology*, vol. 125, no. 5, pp. 992–1004, 2016.

[30] M. Cereda, K. Emami, Y. Xin et al., "Imaging the interaction of atelectasis and overdistension in surfactant-depleted lungs," *Critical Care Medicine*, vol. 41, no. 2, pp. 527–535, 2013.

[31] K. P. McGee, Y. K. Mariappan, R. D. Hubmayr et al., "Magnetic resonance assessment of parenchymal elasticity in normal and edematous, ventilator-injured lung," *Journal of Applied Physiology*, vol. 113, no. 4, pp. 666–676, 2012.

[32] E. L. V. Costa, G. Musch, T. Winkler et al., "Mild endotoxemia during mechanical ventilation produces spatially heterogeneous pulmonary neutrophilic inflammation in sheep," *Anesthesiology*, vol. 112, no. 3, pp. 658–669, 2010.

[33] N. de Prost, E. L. Costa, T. Wellman et al., "Effects of ventilation strategy on distribution of lung inflammatory cell activity," *Critical Care*, vol. 17, no. 4, p. R175, 2013.

[34] G. Musch, T. Winkler, R. S. Harris et al., "Lung [^{18}F]fluorodeoxyglucose uptake and ventilation-perfusion mismatch in the early stage of experimental acute smoke inhalation," *Anesthesiology*, vol. 120, no. 3, pp. 683–693, 2014.

[35] O. Syrkina, C. H. Hales, A. A. Bonab et al., "Molecular imaging of smoke-induced changes in nuclear factor-kappa B expression in murine tissues including the lung," *Journal of Burn Care & Research*, vol. 37, no. 6, pp. 335–342, 2016.

[36] S. S. Yaghoubi and S. S. Gambhir, "PET imaging of herpes simplex virus type 1 thymidine kinase (HSV1-tk) or mutant HSV1-sr39tk reporter gene expression in mice and humans using [^{18}F]FHBG," *Nature Protocols*, vol. 1, no. 6, pp. 3069–3074, 2006.

[37] M. A. Mintun, M. M. Ter-Pogossian, M. A. Green, L. L. Lich, and D. P. Schuster, "Quantitative measurement of regional pulmonary blood flow with positron emission tomography," *Journal of Applied Physiology*, vol. 60, no. 1, pp. 317–326, 1986.

[38] P. Sandiford, M. A. Province, and D. P. Schuster, "Distribution of regional density and vascular permeability in the adult respiratory distress syndrome," *American Journal of Respiratory and Critical Care Medicine*, vol. 151, no. 3, pp. 737–742, 1995.

[39] D. P. Schuster, J. Markham, and M. J. Welch, "Positron emission tomography measurements of pulmonary vascular permeability with Ga-68 transferrin or C-11 methylalbumin," *Critical Care Medicine*, vol. 26, no. 3, pp. 518–525, 1998.

[40] R. Gust, J. Kozlowski, A. H. Stephenson, and D. P. Schuster, "Synergistic hemodynamic effects of low-dose endotoxin and acute lung injury," *American Journal of Respiratory and Critical Care Medicine*, vol. 157, no. 6, pp. 1919–1926, 1998.

[41] D. P. Schuster, C. Anderson, J. Kozlowski, and N. Lange, "Regional pulmonary perfusion in patients with acute pulmonary edema," *Journal of Nuclear Medicine*, vol. 43, no. 7, pp. 863–870, 2002.

[42] T. Richter, R. Bergmann, G. Musch, J. Pietzsch, and T. Koch, "Reduced pulmonary blood flow in regions of injury 2 hours after acid aspiration in rats," *BMC Anesthesiology*, vol. 15, no. 1, p. 36, 2015.

[43] G. Musch, J. D. H. Layfield, R. S. Harris et al., "Topographical distribution of pulmonary perfusion and ventilation, assessed by PET in supine and prone humans," *Journal of Applied Physiology*, vol. 93, no. 5, pp. 1841–1851, 2002.

[44] G. Musch, R. S. Harris, M. F. Vidal Melo et al., "Mechanism by which a sustained inflation can worsen oxygenation in acute lung injury," *Anesthesiology*, vol. 100, no. 2, pp. 323–330, 2004.

[45] M. F. Vidal Melo, D. Layfield, R. S. Harris et al., "Quantification of regional ventilation-perfusion ratios with PET," *Journal of Nuclear Medicine*, vol. 44, no. 12, pp. 1982–1991, 2003.

[46] M. F. V. Melo, R. S. Harris, J. D. H. Layfield, and J. G. Venegas, "Topographic basis of bimodal ventilation-perfusion distributions during bronchoconstriction in sheep," *American Journal of Respiratory and Critical Care Medicine*, vol. 171, no. 7, pp. 714–721, 2005.

[47] J. G. Venegas, T. Winkler, G. Musch et al., "Self-organized patchiness in asthma as a prelude to catastrophic shifts," *Nature*, vol. 434, no. 7034, pp. 777–782, 2005.

[48] R. S. Harris, T. Winkler, G. Musch et al., "The prone position results in smaller ventilation defects during bronchoconstriction in asthma," *Journal of Applied Physiology*, vol. 107, no. 1, pp. 266–274, 2009.

[49] M. F. Vidal Melo, T. Winkler, R. S. Harris, G. Musch, R. E. Greene, and J. G. Venegas, "Spatial heterogeneity of lung perfusion assessed with ^{13}N PET as a vascular biomarker in chronic obstructive pulmonary disease," *Journal of Nuclear Medicine*, vol. 51, no. 1, pp. 57–65, 2010.

Hindawi
Contrast Media & Molecular Imaging
Volume 2019, Article ID 9294586, 10 pages
https://doi.org/10.1155/2019/9294586

Research Article

Evaluation of Myelin Radiotracers in the Lysolecithin Rat Model of Focal Demyelination: Beware of Pitfalls!

Min Zhang,[1,2,3] **Gaëlle Hugon**,[1,2] **Caroline Bouillot**,[4] **Radu Bolbos**,[4] **Jean-Baptiste Langlois**,[4] **Thierry Billard**,[4,5,6] **Frédéric Bonnefoi**,[4] **Biao Li**,[3] **Luc Zimmer**,[1,4,7] **and Fabien Chauveau**[1,2]

[1]*University of Lyon, Lyon Neuroscience Research Center (CRNL), Lyon, France*
[2]*CNRS UMR5292, INSERM U1028, University of Lyon 1, F-69003 Lyon, France*
[3]*Shanghai Jiao Tong University, School of Medicine, Department of Nuclear Medicine, Rui Jin Hospital, Shanghai, China*
[4]*CERMEP-Imagerie Du Vivant, F-69677 Bron, France*
[5]*University of Lyon, Institute of Chemistry and Biochemistry (ICBMS), Lyon, France*
[6]*CNRS UMR5246, University of Lyon 1, F-69622 Lyon, France*
[7]*Hospices Civils de Lyon, F-69677 Bron, France*

Correspondence should be addressed to Fabien Chauveau; chauveau@cermep.fr

Received 28 November 2018; Revised 6 February 2019; Accepted 21 February 2019; Published 29 May 2019

Guest Editor: Aage K. O. Alstrup

The observation that amyloid radiotracers developed for Alzheimer's disease bind to cerebral white matter paved the road to nuclear imaging of myelin in multiple sclerosis. The lysolecithin (lysophosphatidylcholine (LPC)) rat model of demyelination proved useful in evaluating and comparing candidate radiotracers to target myelin. Focal demyelination following stereotaxic LPC injection is larger than lesions observed in experimental autoimmune encephalitis models and is followed by spontaneous progressive remyelination. Moreover, the contralateral hemisphere may serve as an internal control in a given animal. However, demyelination can be accompanied by concurrent focal necrosis and/or adjacent ventricle dilation. The influence of these side effects on imaging findings has never been carefully assessed. The present study describes an optimization of the LPC model and highlights the use of MRI for controlling the variability and pitfalls of the model. The prototypical amyloid radiotracer [^{11}C]PIB was used to show that *in vivo* PET does not provide sufficient sensitivity to reliably track myelin changes and may be sensitive to LPC side effects instead of demyelination as such. *Ex vivo* autoradiography with a fluorine radiotracer should be preferred, to adequately evaluate and compare radiotracers for the assessment of myelin content.

1. Introduction

Multiple sclerosis (MS) is a chronic inflammatory demyelinating disorder affecting the quality of life, employment, and social relationships of approximately 2.1 million people worldwide. The formation of focal demyelinated lesions and progressive failure of remyelination is the main characteristic of MS and further leads to axonal injury and neuron loss [1]. Magnetic resonance imaging (MRI) is essential for diagnosis and continuous management of MS [2]. However, conventional MRI measurements (lesion burden, location, and type) correlate poorly with disability and lack long-term prognostic value. New disease-modifying treatments which promote remyelination are now entering clinical evaluation [3]. Therefore, an urgent challenge is to identify the best objective, reliable, and predictive biomarker of remyelination. There is no consensus on which imaging technique should be used. Advanced MRI techniques such as magnetization transfer imaging (MTI) [4] or myelin water fraction (MWF) [5] are increasingly popular as research tools but have not yet been standardized for widespread clinical application. Quantification is not straightforward, as myelin content is inferred indirectly from water binding to lipid bilayer macromolecules [6, 7].

By contrast, positron emission tomography (PET) may provide more direct quantitative assessment of myelin content, by injection of a radiolabeled probe targeting myelin proteins. Several independent groups have illustrated the ability of [^{11}C]PIB to detect white matter alterations in MS [8, 9] and other pathological conditions [10, 11]. These pioneering studies have stimulated the search for new myelin radiotracers with enhanced specific (white matter) binding ratio over nonspecific (gray matter) binding ratio [12] and, ideally, with fluorine-18 labeling to enable wider clinical use [13, 14]. Among available models of demyelination, the simple model consisting in intracerebral injection of lysophosphatidylcholine (LPC, or lysolecithin) [15] appears attractive for first-step evaluation of radiotracers: the detergent action of LPC produces focal demyelination, followed by spontaneous progressive remyelination, while the contralateral hemisphere may serve as an internal control in a given animal. Hence, several imaging studies have used the LPC model in rats, to evaluate MRI biomarkers [16, 17] or PET radiotracers [12, 18]. However, as previously reported by several groups, LPC-induced demyelination may be associated with concurrent focal necrosis [16, 18, 19] and/or ventricle dilation [20]. The influence of these side effects on imaging findings has never been carefully assessed.

The present study describes an optimization of the LPC model and highlights the use of MRI for controlling the variability and pitfalls of the model. Using the prototypical radiotracers [^{11}C]PIB and [^{18}F]AV-45, we show that (i) *in vivo* PET does not provide sufficient sensitivity to reliably track myelin changes in this model and (ii) *ex vivo* autoradiography should rather be used to adequately evaluate and compare radiotracer performance.

2. Materials and Methods

2.1. Animals. A completed ARRIVE (Animal Research: Reporting of In Vivo Experiments) guidelines checklist is included as supplementary material (S1). All experiments were carried out under a protocol approved by the local ethical review board ("Comité d'éthique pour l'Expérimentation Animale Neurosciences Lyon", registration code: C2EA-42), authorized by the French Ministry of Higher Education and Research (n°5892-2016063014207327v2), and were in accordance with European directives on the protection and use of laboratory animals (Council Directive 2010/63/UE, French decree 2013-118).

2.2. Housing. Adult male Sprague Dawley rats (ILAR code Crl:CD(SD)) were ordered from Charles River (L'Arbresle, France) and given a minimum of five days to acclimate to the conventional housing facility, under temperature-controlled (range 20–24°C) conditions and a 12 : 12 h light-dark cycle, with lights on at 07 : 00 and off at 19 : 00. Animals were housed by group of six in open polycarbonate cages (Tecniplast, 2000P, $L \times W \times H = 610 \times 435 \times 215$ mm, floor area 2065 cm^2), with stainless steel lids. Environmental enrichment included spruce-based bedding of 2–4 mm granulometry (Lignocel 3/4 s), round tinted polycarbonate tunnels (153 × 75 mm, SERLAB), and hazel chew blocks (JR Farm). Animals were given access to pellets of wheat and corn (Teklad Global 18% Protein Rodent Diet, ENVIGO) and tap water ad libitum. During housing, animals were monitored daily for health status. At the start of the experiments, animals weighed 250–350 grams.

2.3. Surgery. Demyelination was induced by stereotaxic injection of LPC (Sigma-Aldrich, ref. L4129) at 1% in saline solution into the right corpus callosum and saline into the contralateral site, infused at 0.1 μl/min. Three different injection conditions were successively tested (no randomization):

(i) In group 1 ($n = 8$), injection sites were adapted from previous studies: AP −0.3 mm; ML ±3.0 mm; DV −3.5/−4.0/−4.5/−5.0 mm; 2.5 μl each, from depth to superficial

(ii) In group 2 ($n = 9$), injection sites were slightly adjusted: AP −0.3 mm; ML ±3.3 mm; DV −3.0/−3.7/−4.3/−5.0 mm; 2.5 μl each, from depth to superficial

(iii) In group 3 ($n = 10$), injection sites were restricted to corpus callosum: AP −0.3 mm; ML ±3.3 mm; DV −2.8/−3.5 mm; 2.5 μl each, from depth to superficial

Rats were anesthetized with isoflurane inhalation in air in an anesthesia induction box and then transferred to a stereotaxic apparatus (Stoelting) equipped with a mask delivering isoflurane at 1.0–2.5% for the duration of the experiment. Body temperature was maintained by a heating pad set at 37°C and monitored using a rectal probe. Pain was controlled by buprenorphine (Buprecare, Axience), a potent opioid analgesic, injected subcutaneously at a dose of 0.05 mg/kg 20 min before any surgical act was performed. A local analgesic (lidocaine/prilocaine 5%, Pierre Fabre) was also applied on the scalp before incision. After bilateral craniotomy, LPC and saline were slowly infused with 30-gauge needles (RN type, NH-BIO) via a tubing (Fine Bore Polythene Tubing, Portex, Smith Medical Intl) connected to syringes installed in injection pumps (World Precision Instruments). The needles were left in place for 2 min and then slowly withdrawn. After injection, the scalp was sutured, and an antiseptic (povidone-iodine) and local analgesic (lidocaine) were applied. The rats were then allowed to recover from anesthesia. The long-term action of buprenorphine (ca 6 hours) allowed the animals to completely recover without the need of a second administration. No adverse events were observed.

Imaging studies were performed on an additional batch of animals (10 animals injected as in group 3, with a single animal being the experimental unit) and started 7 days postinjection with MRI. One animal showed no MRI changes and was excluded. *In vivo* PET, or *ex vivo* autoradiography, was performed between 8 and 15 days postinjection in 9 animals, a period during which no significant spontaneous remyelination is expected [12, 17, 18].

2.4. In vivo Study. All imaging sessions were performed under isoflurane anesthesia delivered in air by approved systems (TEM Sega).

2.4.1. MR Imaging. The animals were placed in prone position in a dedicated plastic bed equipped with a stereotactic holder (Bruker Biospec Animal Handling Systems) and maintained under gaseous anesthesia delivered via a cone mask throughout the MRI protocol. Body temperature was maintained at $37 \pm 1^{\circ}$C by thermoregulated water via a circuit incorporated in the plastic bed. A respiratory sensor was then placed on the abdomen to continuously monitor respiration rate on a specialized device (ECG Trigger Unit HR V2.0, Rapid Biomedical).

MRI acquisitions were performed on a horizontal 7T Bruker Biospec MRI system (Bruker Biospin MRI GmbH) with a set of 400 mT/m gradients, controlled by a Bruker ParaVision 5.1 workstation. A Bruker birdcage volume coil (outer diameter = 112 mm and inner diameter = 72 mm) was used for signal transmission and a Bruker single-loop surface coil (25 mm diameter), positioned on the head of the animal to target the brain, for signal reception.

For the MRI protocol, 2D T2-weightedfat-saturated images (T2WI) on the rapid acquisition with relaxation-enhanced (RARE) method were obtained on axial slices. Acquisition parameters were as follows: echo time (TE) 60 ms, repetition time (TR) 5000 ms, RARE factor = 8, and average = 4. A total of 15.1 mm slices were acquired with field of view (FOV) of 3 cm × 1.5 cm and matrix size of 256 × 128, providing in-plane resolution of 117 × 117 microns, for 4 minutes' scan time.

2.4.2. [^{11}C]PIB PET/CT Imaging. [^{11}C]PIB was labeled as previously described [21]. Radiochemical purity was >95%. After catheterization of a caudal vein, animals ($n = 4$) were positioned prone in a micro-PET/CT apparatus (Inveon, Siemens) with the head centered in the field of view (FOV). Gaseous anesthesia was maintained via a cone mask, and breathing rate was monitored throughout the experiment. [^{11}C]PIB with mean activity of 14.2 MBq (383 μCi) (range, 9.6–20.2 MBq) was injected intravenously as a bolus. Dynamic PET acquisition in list mode over 60 min was started immediately after radiotracer injection. CT scanning was performed to correct attenuation and scatter. All PET images were reconstructed by 3D ordinary poisson ordered subsets expectation-maximization (OP-OSEM3D) with 4 iterations and a zoom factor of 2. The reconstructed volume comprised 159 slices of 128 × 128 voxels, in a bounding box of 49.7 × 49.7 × 126 mm. Nominal in-plane resolution was ~1.4 mm full-width-at-half-maximum in the FOV center.

2.4.3. Image Analysis. Using the MIPAV (Medical Image Processing, Analysis, and Visualization) application (https://mipav.cit.nih.gov/), MR images were visually inspected in search for areas in the corpus callosum exhibiting a normalization of the natively hyposignal (Figure 1(a)) and for any edematous hypersignal encompassing the corpus callosum and adjacent areas (Figure 1(b)). A region of interest (ROI) encompassing the abnormal area of the corpus callosum was manually drawn on MR slices and mirrored onto the contralateral corpus callosum. In addition, brain slices were screened to identify and measure the maximal width of the lateral ventricle along the mediolateral plane (Figure 1(c)). Each of these two measurements was performed by two operators (blind to other data). MR images were then imported in the Inveon Research Workpackage (IRW, Siemens) and registered onto PET/CT images. Summed tracer uptake (% injected dose per gram) in the ROIs was calculated from 20 to 40 minutes' acquisition.

2.5. Ex vivo Study

2.5.1. [^{18}F]AV-45 Autoradiography. [^{18}F]AV-45 was labeled as previously described [22, 23]. Radiochemical purity was >95%. Under isoflurane anesthesia, animals ($n = 5$) were intravenously injected with 12.6 MBq (340 μCi) (range, 8.6–18.9 MBq) [^{18}F]AV-45 and euthanized 10 min after radiotracer injection. Brains were rapidly removed, snap-frozen at -20°C, coronally cryosectioned into 30 μm slices, and mounted on glass slides. After air-drying at room temperature, slides were exposed to sensitive imaging plates (BAS-IP MS 2025, Fujifilm) for 4 hours. The distribution of radioactivity was then digitized on a bioimaging analyzer (BAS-5000, Fujifilm).

2.5.2. Myelin Histological Staining. Following autoradiography, brain sections were postfixed with 4% formaldehyde in PBS, then briefly dehydrated in 70% ethanol. Slides were incubated in 0.1% Sudan Black B (SBB) solution (Sigma-Aldrich, ref. 199664) at room temperature for 10 min, washed in 70% ethanol for 10–30 s, then moved into distilled water for mounting in aqueous medium (Roti-Mount, Carl Roth). The slides with demyelinated lesions were observed and photographed under a microscope (Axioplan 2, Zeiss).

2.5.3. Image Analysis. Autoradiograms were visualized on Multigauge software (Fujifilm). ROIs were drawn manually on the targeted injection sites in the corpus callosum by a single operator, and lesion-to-contralateral uptake ratios were calculated. Corresponding ROIs were also drawn manually on histological images, and myelin content in ipsilateral and contralateral corpus callosum were semi-quantitatively measured by an experienced observer blind to the autoradiography results, using Image-Pro Plus 6.0 software (Media Cybernetics) and expressed as optical density per unit area. The lesion-to-contralateral ratios were then calculated for optical density per unit area. For each animal, quantification was performed on 4 brain sections encompassing the whole volume showing a decreased binding, hence resulting in 20 measurements.

2.6. Statistical Analysis. Data were analyzed on SPSS 19.0 software. Group comparisons were performed using Kruskal–Wallis tests and Mann–Whitney test after binarization of side-effect detection. Slice-by-slice correlation between autoradiography and histology measurements, as well as correlation between operators, used Spearman's tests. The significance threshold was set at $p < 0.05$.

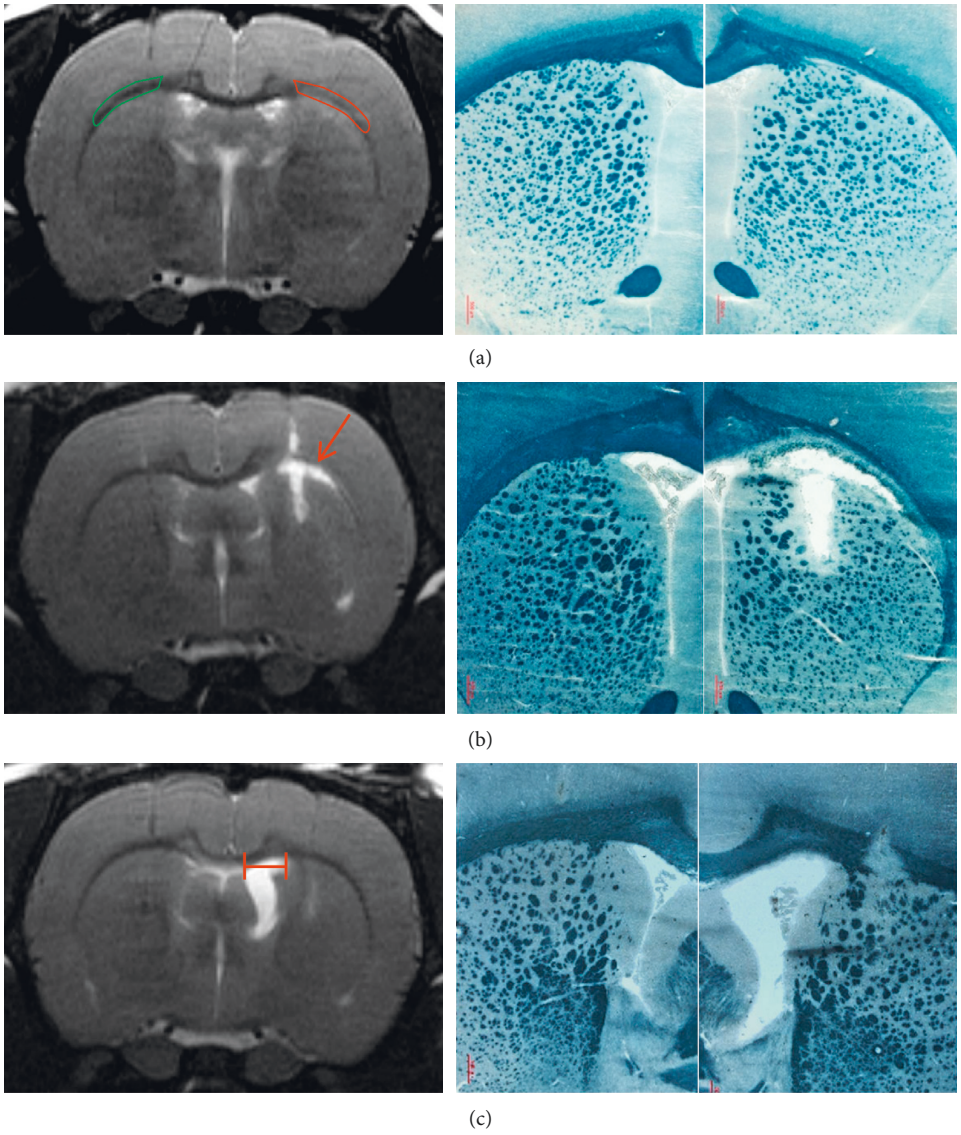

Figure 1: Comparison of MRI (T2WI, left column) and histology with Sudan black B (SBB, right column) at the injection sites. Postmortem histological staining matched *in vivo* MRI observations. Therefore, anatomical MRI was used to (a) manually delineate areas of demyelination showing corpus callosum loss of hypointense contrast (in red, with mirror region of interest in green), (b) identify necrosis areas with overt focal edematous hypersignal (arrow), and (c) measure the maximum width of the lateral ventricle along the mediolateral plane (red segment) as an index of ventricular dilation after LPC injection.

3. Results

3.1. MRI-Based Optimization of LPC Injections. Optimization of the injection protocol was driven by the need to obtain a large area of demyelination in the corpus callosum, so as to be clearly detected *in vivo* on PET. However, necrosis and adjacent ventricular dilation are pitfalls commonly reported after LPC injection [12, 18–20]. In line with these reports, our first attempts to establish a pure model of demyelination highlighted the need to keep a low LPC concentration (1%) and low injection speed (0.1 μL/min) (data not shown). Because visual postmortem examination of brain tissue, seen upon cutting brains on a cryostat, may be biased by extraction and processing, *in vivo* anatomical T2-weighted MRI was used to evaluate different injection protocols. Although T2 contrast might be influenced by several concurrent processes, pilot histological comparisons showed a fair agreement between (i) the loss of the natively hypointense contrast of corpus callosum and successful demyelination (Figure 1(a)) and (ii) strong edematous hypersignals and necrosis (Figure 1(b)). Therefore, in an effort to provide immediately available criteria for enrolling animals into a subsequent PET protocol, the following simple MRI metrics were used for evaluating the optimization process: (i) manual delineation of signal abnormality on corpus callosum as a surrogate for demyelination (Figure 1(a)) and (ii) manual measurement of the maximal width of the lateral ventricle as a surrogate for abnormal dilation (Figure 1(c)). Two operators independently performed

these two measurements with overall good reproducibility (both correlations were significant at the $p < 0.01$ level). Importantly, deviations were below the resolution of PET imaging. Raw data are provided as supplementary dataset S2, and mean of the two measurements is reported thereafter.

Figure 2 summarizes the results of this optimization process in three experimental groups. In the first group, we adapted previously reported injection conditions (group 1: 4 injection sites in striatum and corpus callosum; total volume 10 μl). This led to detectable edematous hypersignals in half of the animals and a mean ventricle width of 1.9 ± 0.5 mm. In group 2, increasing the distance between the 4 injection points and the lateral distance from the bregma only slightly decreased the rate of edema (4 over 9 animals) and reduced ventricle width (1.7 ± 0.5 mm). As edematous foci were mainly observed in the striatum, we simplified the injection protocol and kept only two injection sites, at the lower and upper levels of the corpus callosum (group 3; total volume 5 μl); with this protocol, no animals showed focal edema, and ventricle width was further reduced (1.2 ± 0.5 mm). The mean volume of the abnormally normalized signal in the corpus callosum increased in parallel with the reduction of LPC side effects, reaching $2.4 \pm 0.9\,\text{mm}^3$, which suggested increased demyelination. However, these measurements were not significantly different between groups ($p > 0.05$), highlighting the residual variability of the model and prompting us to examine how PET signals were affected. Would the following exclusion criteria have been applied: (i) focal edematous hypersignal or (ii) maximal lateral ventricle width >1.4 mm (corresponding to the in-plane PET resolution)—only 5 animals over 27 would have been considered devoid of side effects and selected (1 in group 1 and 4 in group 3). Of note, the volume of the abnormally normalized signal in the corpus callosum, or "apparent" demyelination, was significantly higher in these 5 rats than in the 22 others with at least one side effect ($p = 0.03$).

3.2. In vivo [^{11}C]PIB PET. Among a new batch of animals, injected in the conditions as group 3, four additional rats were selected, to reflect the variety of lesions and pitfalls following LPC injection. These animals underwent [^{11}C]PIB PET imaging between 8 and 15 days after stereotaxic injection. Apparent demyelination volume on MRI and [^{11}C]PIB uptake within this volume and in a mirror volume in the contralateral corpus callosum are reported in Table 1. In rats A and B, [^{11}C]PIB uptake was not decreased (ratio ≥ 1) despite a large demyelination area without edematous lesion or ventricle dilation (Figures 3(a) and 3(b)). Rats C and D presented a smaller demyelination area and one side effect each: focal edema in rat C (Figure 3(c)) and ventricle dilation (max width > 1.4 mm) in rat D (Figure 3(d)). MRI-driven quantification showed slightly decreased [^{11}C]PIB uptake in rat C (ratio 0.88) but not rat D (ratio 1.00). Importantly, PET images highlighted decreased PIB uptake at the necrosis and ventricle dilation sites. These results strongly suggested that *in vivo* [^{11}C]PIB PET imaging could not reliably detect demyelination in the LPC-induced rodent model. Moreover, side effects of LPC injection may lead to false-positive detection of demyelination when concurrent MRI is not available. These qualitative but clear-cut results were considered as an endpoint for the PET study.

3.3. Ex vivo [^{18}F]AV-45 Autoradiography. Because *in vivo* detection of LPC-induced demyelination may be inaccurate due to lack of spatial resolution and consequently decreased sensitivity, 5 additional animals, injected in the same conditions as group 3, underwent *ex vivo*high-resolution autoradiography. Obtaining *ex vivo* images with a measurable signal-to-noise ratio required changing from the carbon-11 PIB tracer to a fluorine-18 radiotracer, such as [^{18}F]AV-45. At this 100 μm spatial resolution, pitfalls of the animal model were easily identified as complete lack of signal in the 2D images (Supplementary Figure S3) and could not be confounded with loss of binding in the demyelinated corpus callosum. Binding in the ipsilateral corpus callosum was clearly decreased in all animals (Figure 4(a)), confirming the MRI observations (Figure 4(b)). The ipsi-to-contralateral [^{18}F]AV-45 uptake ratio, averaged from 4 brain sections per animal, was similar in all five animals (0.78 ± 0.02). Furthermore, subsequent myelin histology on the same sections correlated visually (Figure 4(c)) and quantitatively (Figure 4(d), $r = 0.559$, $p = 0.005$) with the corresponding [^{18}F]AV-45 signals.

4. Discussion

Unilateral LPC-induced demyelination has gained increased popularity as a first-line animal model for preclinical evaluation of imaging biomarkers. Compared to other rodent models of demyelination, it has the advantages of (i) producing larger demyelination lesions than EAE models [24] and (ii) not requiring another group of control animals, as for transgenic shivered mice [25] or cuprizone-induced demyelination [26]. The goal of the present study was to set up a workflow for the evaluation of new myelin radiotracers using this LPC model in rats.

As a first step, we observed, as previously reported, that demyelination of the corpus callosum can be accompanied by necrosis and/or ipsilateral ventricle dilation [19, 20]. Necrosis might be due to locally excessive LPC concentration, and ventricle dilation is thought to be mediated by inflammation. Here, we used anatomical MRI to monitor the incidence of these side effects *in vivo* (Figure 1). By targeting white matter in the corpus callosum only (without striatum), and by increasing the mediolateral distance of the injection sites, we were able to reduce the proportion of animals without any side effects. Further refinements of the injection procedure might include the use of (i) glass-capillary microneedles to minimize tissue damage and nonspecific inflammatory responses [27] and (ii) T2 mapping instead of T2-weighted imaging, so as to allow an operator-independent,threshold-based, estimation of ventricle volume, and corpus callosum apparent demyelination [28].

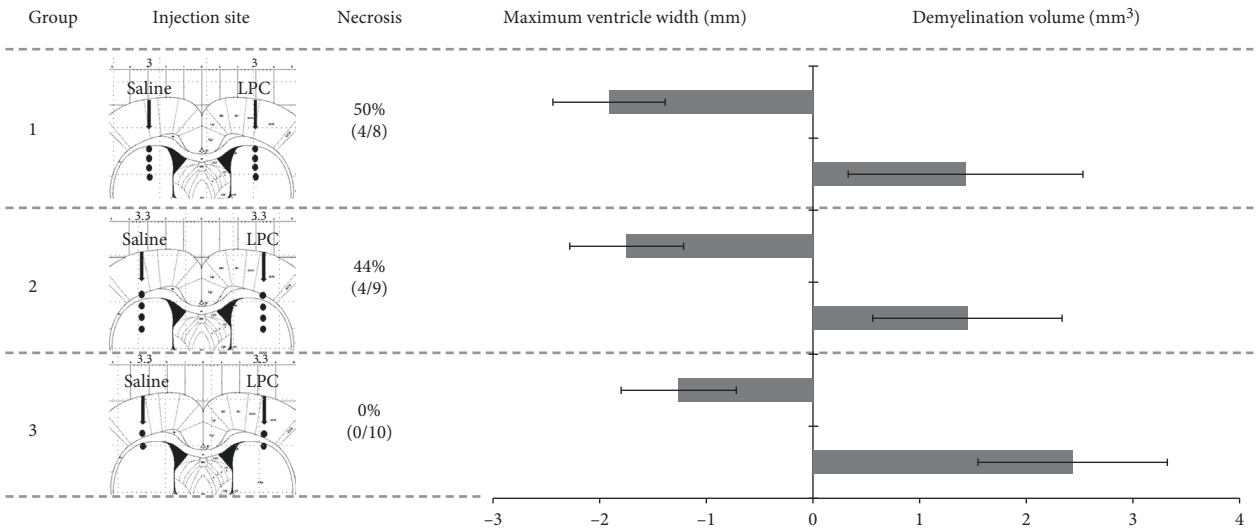

Figure 2: Optimization of the LPC injection protocol. LPC concentration (1% in saline) and infusion rate (0.1 μl/min) were kept constant between the three groups. The injection sites are shown in the corresponding Paxinos coronal diagram, with the following coordinates: group 1, AP −0.3 mm, ML ±3.0 mm, DV −3.5/−4.0/−4.5/−5.0 mm; group 2, AP −0.3 mm, ML ±3.3 mm, DV −3.0/−3.7/−4.3/−5.0 mm; group 3, AP −0.3 mm, ML ±3.3 mm, DV −2.8/−3.5 mm. Each site was infused with 2.5 μl of LPC, from depth to superficial. The rate of animals exhibiting focal edematous hypersignals on MRI (as in Figure 1(b)) is given as a percentage (and number of animals out of total the group number). The graph shows the maximum ventricle width (measured along the mediolateral plane as in Figure 1(c), and arbitrarily expressed as a negative value, in mm) and the total volume of corpus callosum exhibiting a normalization of the natively hypointense contrast (measured as in Figure 1(a), in mm^3).

Table 1: Quantification of [^{11}C]PIB uptake in ipsilateral (LPC) and contralateral (SAL) regions of interest (ROI) manually drawn onto T2WI (as shown in Figure 1(a)). The LPC-to-SAL ratio is expected to be < 1 in case of demyelination.

Rat	MRI observations	Vol. (mm^3) of ROI on T2WI	[^{11}C]PIB uptake (%ID/g)		
			LPC	SAL	Ratio
A	Large demyelination	5.20	0.16	0.15	1.03
B	Large demyelination	3.70	0.53	0.47	1.12
C	Small demyelination with necrosis	2.20	0.25	0.29	0.88
D	Small demyelination with ventricle dilation	1.90	0.23	0.23	1.00

Although previous studies reported testing several injection conditions [17, 19], the impact on imaging was never assessed. Therefore, in the second step, a limited number of PET imaging sessions with the reference radiotracer [^{11}C]PIB were conducted in additional animals representing the range of pathological conditions observed after LPC injection. The results unambiguously showed that ipsilateral tracer uptake in areas of demyelination was not decreased after LPC injection (rats A and B), although their volume exceeded the resolution of the small-animal PET scanner. Even more concerning was the observation of apparently decreased uptake in the necrosis site or enlarged ventricle (rats C and D). Therefore, in the absence of individual MRI, PET-driven analysis might incorrectly suggest demyelination (false-positive detection). These results highlight the low sensitivity of [^{11}C]PIB for detecting demyelination in small-animal models. Several factors may be put forward, including the mm-range resolution of small-animal PET scanners, combined with the low volume of highly myelinated axons in rodents, but also the relatively high nonspecific binding of [^{11}C]PIB. For ethical reasons, we considered these qualitative but clear-cut results as an endpoint for our PET study.

In the third step, we used *ex vivo* autoradiography instead of *in vivo* imaging. Five additional animals were injected with the fluorine-18 radiotracer [^{18}F]AV-45, because the short half-life of carbon-11 prevented accumulating enough signal. It should be noted that *in vitro* autoradiography is of little value for assessing radiotracer binding to myelin, because white matter to gray matter contrast entirely depends on washing conditions (data not shown) and might not reflect *in vivo* uptake. *Ex vivo* autoradiography appeared to be a viable strategy for assessing radiotracer performance in the LPC model for several reasons. First, side effects were easily identified and distinguished from the surrounding tissue on brain sections. Second, the signal drop in the injected corpus callosum reached 20%, which was highly reproducible (coefficient of variation < 3% between the 5 rats) and correlated with histology measurements. Though quantification was restricted to discrete 2D measurements on

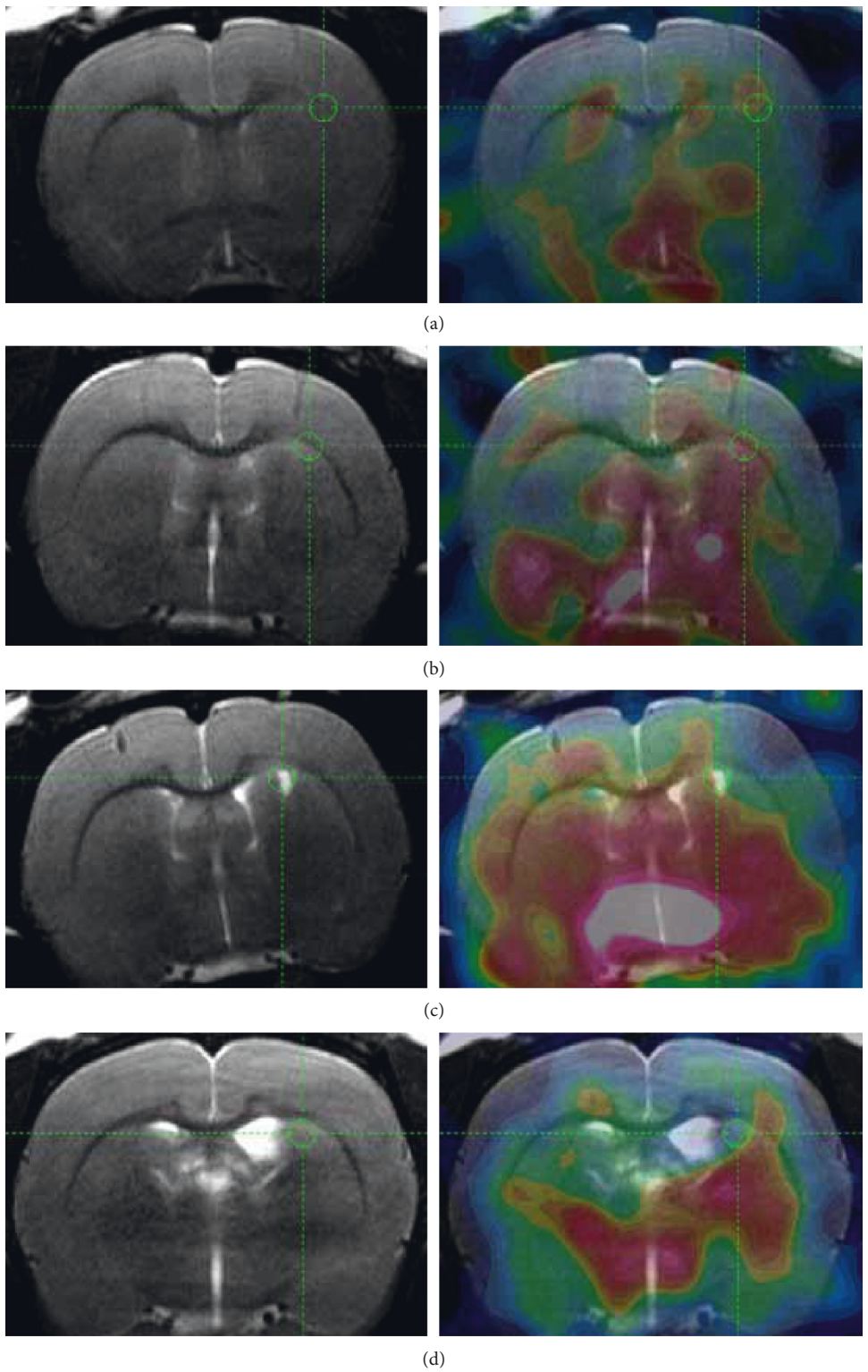

Figure 3: *In vivo* PET imaging with [^{11}C]PIB. T2WI MRI is shown in the left column and overlaid with a 20 min summed PET image of [^{11}C] PIB in the right column. Rats A and B (a, b) exhibited a large demyelination area without necrosis or ventricle dilation. Rats C and D (c, d) presented a smaller demyelination area and necrosis (c) or ventricle dilation (d).

four brain sections per animal in this proof-of-concept experiment, 3D-reconstruction methods dedicated to autoradiography may be used in future studies to assess signal drop in a continuous volume similar to *in vivo* imaging [29]. Overall, these promising results are in line with recent reports of repurposed fluorine-18 labeled amyloid radiotracers in MS patients (florbetapir or [^{18}F] AV-45 [30] and florbetaben or [^{18}F]AV-1 [31]).

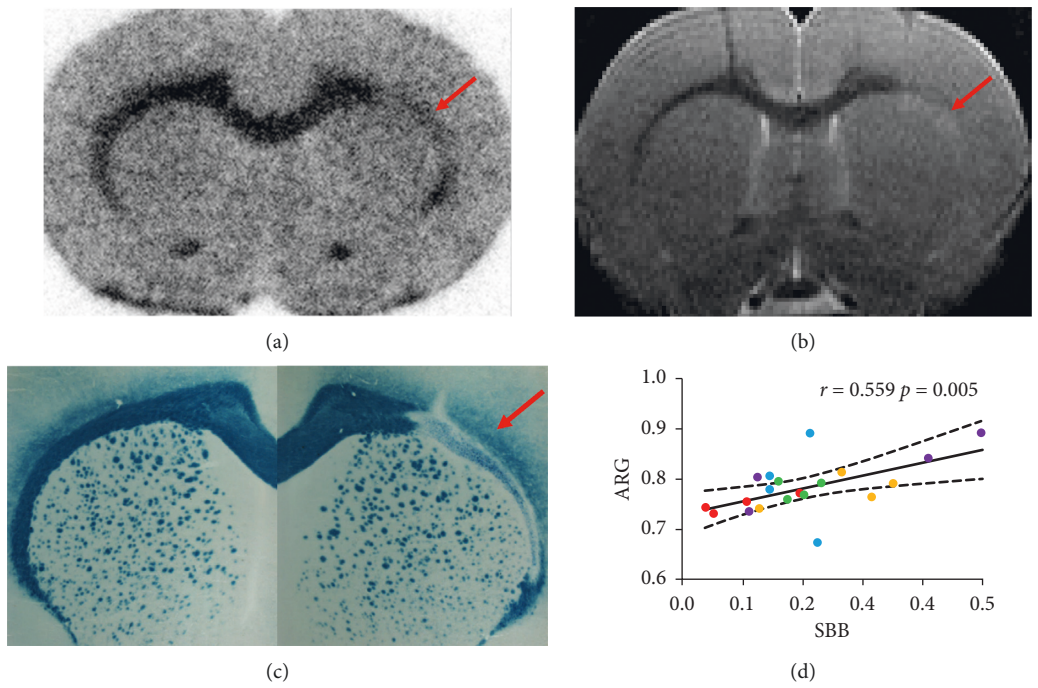

Figure 4: *Ex vivo* autoradiography with [^{18}F]AV-45. Reduced [^{18}F]AV-45 uptake in the LPC-injected site was visually identified ((a), arrow), and matched T2WI MRI (b), as well as Sudan Black B staining, which confirmed demyelination (c). Four sections per animal (each rat is represented with a different color), encompassing the whole area showing a decreased binding, were analyzed, hence resulting in 20 measurements (d). There was a significant correlation ($r = 0.559$, $p = 0.005$) between the ratio of ipsi-to-contralateral [^{18}F]AV-45 binding on autoradiography (ARG) and the corresponding ratio of ipsi-to-contralateral optical density on Sudan Black B (SBB) staining (plain line, linear fit; dashed lines, 95% confidence interval).

5. Conclusion

This study aimed to draw attention to common pitfalls associated with LPC injections in the central nervous system and their impact on nuclear imaging of myelin. While this animal model is attractive for evaluating imaging biomarkers of demyelination and remyelination, *in vivo* PET imaging in small animals may be sensitive to side effects of LPC injections rather than real demyelination. We conclude that appropriate use of this rodent model requires MRI to correctly identify animals with pure demyelination and *ex vivo* autoradiography to track spatial myelin changes with enough sensitivity. Alternatively, longitudinal studies with *in vivo* PET imaging could possibly be performed after LPC injection in larger animals, such as rabbits [32], swine [33], or primates [34].

Data Availability

All the data used to support the findings of this study are available from the corresponding author upon request.

Disclosure

Pr. Luc Zimmer is an academic editor of *Contrast Media & Molecular Imaging*.

Conflicts of Interest

The authors declare that they have no conflicts of interest.

Acknowledgments

Dr. Min Zhang was supported by the National Natural Science Foundation of China (81501499), Shanghai Jiaotong University Med-X Interdisciplinary Research Funding (YG2017MS61), and Shanghai Pujiang Program (18PJD030). This work was performed at CERMEP-Imagerie du Vivant within the framework of the Labex PRIMES (ANR-11-LABX-0063) of the University of Lyon, under the "Investissements d'Avenir" program (ANR-11-IDEX-0007) operated by the French National Research Agency (ANR).

Supplementary Materials

Document S1: completed "The ARRIVE Guidelines Checklist" for reporting animal data in this manuscript (downloaded from https://www.nc3rs.org.uk/arrive-guidelines). Dataset S2: individual measures and observations performed in rats from groups 1–3, by two independent operators. Figure S3: *ex vivo*[18F]AV-45 autoradiography sections showing the visual identification (red arrows) of cavitation resulting from necrotic tissue (A) and ventricle dilation (B). (*Supplementary Materials*)

References

[1] H. L. Zwibel and J. Smrtka, "Improving quality of life in multiple sclerosis: an unmet need," *American Journal of Managed Care*, vol. 17, no. 5, pp. 139–145, 2011.

[2] A. J. Thompson, B. L. Banwell, F. Barkhof et al., "Diagnosis of multiple sclerosis: 2017 revisions of the McDonald criteria," *Lancet Neurology*, vol. 17, no. 2, pp. 162–173, 2018.

[3] J. R. Plemel, W.-Q. Liu, and V. W. Yong, "Remyelination therapies: a new direction and challenge in multiple sclerosis," *Nature Reviews Drug Discovery*, vol. 16, no. 9, pp. 617–634, 2017.

[4] C. R. McCreary, T. A. Bjarnason, V. Skihar, J. R. Mitchell, V. W. Yong, and J. F. Dunn, "Multiexponential T2 and magnetization transfer MRI of demyelination and remyelination in murine spinal cord," *NeuroImage*, vol. 45, no. 4, pp. 1173–1182, 2009.

[5] J. Zhang, S. H. Kolind, C. Laule, and A. L. MacKay, "Comparison of myelin water fraction from multiecho T2 decay curve and steady-state methods," *Magnetic Resonance in Medicine*, vol. 73, no. 1, pp. 223–232, 2015.

[6] C. Enzinger, F. Barkhof, O. Ciccarelli et al., "Nonconventional MRI and microstructural cerebral changes in multiple sclerosis," *Nature Reviews Neurology*, vol. 11, no. 12, pp. 676–686, 2015.

[7] C. Louapre, B. Bodini, C. Lubetzki, L. Freeman, and B. Stankoff, "Imaging markers of multiple sclerosis prognosis," *Current Opinion in Neurology*, vol. 30, no. 3, pp. 231–236, 2017.

[8] B. Stankoff, L. Freeman, M.-S. Aigrot et al., "Imaging central nervous system myelin by positron emission tomography in multiple sclerosis using [methyl-^{11}C]-2-(4′-methyl-aminophenyl)-6-hydroxybenzothiazole," *Annals of Neurology*, vol. 69, no. 4, pp. 673–680, 2011.

[9] B. Zeydan, V. J. Lowe, C. G. Schwarz et al., "Pittsburgh compound-B PET white matter imaging and cognitive function in late multiple sclerosis," *Multiple Sclerosis Journal*, vol. 24, no. 6, pp. 739–749, 2018.

[10] L. Glodzik, H. Rusinek, J. Li et al., "Reduced retention of Pittsburgh compound B in white matter lesions," *European Journal of Nuclear Medicine and Molecular Imaging*, vol. 42, no. 1, pp. 97–102, 2015.

[11] A. E. Goodheart, E. Tamburo, D. Minhas et al., "Reduced binding of Pittsburgh compound-B in areas of white matter hyperintensities," *NeuroImage: Clinical*, vol. 9, pp. 479–483, 2015.

[12] D. de Paula Faria, S. Copray, J. W. A. Sijbesma et al., "PET imaging of focal demyelination and remyelination in a rat model of multiple sclerosis: comparison of [^{11}C]MeDAS, [^{11}C]CIC and [^{11}C]PIB," *European Journal of Nuclear Medicine and Molecular Imaging*, vol. 41, no. 5, pp. 995–1003, 2014.

[13] C. Wu, B. Eck, S. Zhang et al., "Discovery of 1,2,3-triazole derivatives for multimodality PET/CT/cryoimaging of myelination in the central nervous system," *Journal of Medicinal Chemistry*, vol. 60, no. 3, pp. 987–999, 2017.

[14] A. D. Tiwari, C. Wu, J. Zhu et al., "Design, synthesis, and evaluation of fluorinated radioligands for myelin imaging," *Journal of Medicinal Chemistry*, vol. 59, no. 8, pp. 3705–3718, 2016.

[15] S. M. Hall, "The effect of injections of lysophosphatidyl choline into white matter of the adult mouse spinal cord," *Journal of Cell Science*, vol. 10, no. 2, pp. 535–546, 1972.

[16] M. N. Degaonkar, R. Jayasundar, and N. R. Jagannathan, "Sequential diffusion-weighted magnetic resonance imaging study of lysophosphatidyl choline-induced experimental demyelinating lesion: an animal model of multiple sclerosis," *Journal of Magnetic Resonance Imaging*, vol. 16, no. 2, pp. 153–159, 2002.

[17] M. S. A. Deloire-Grassin, B. Brochet, B. Quesson et al., "In vivo evaluation of remyelination in rat brain by magnetization transfer imaging," *Journal of the Neurological Sciences*, vol. 178, no. 1, pp. 10–16, 2000.

[18] Y. Wang, C. Wu, A. V. Caprariello et al., "In vivo quantification of myelin changes in the vertebrate nervous system," *Journal of Neuroscience*, vol. 29, no. 46, pp. 14663–14669, 2009.

[19] D. de Paula Faria, E. F. de Vries, J. W. A. Sijbesma, C. A. Buchpiguel, R. A. Dierckx, and S. C. Copray, "PET imaging of glucose metabolism, neuroinflammation and demyelination in the lysolecithin rat model for multiple sclerosis," *Multiple Sclerosis Journal*, vol. 20, no. 11, pp. 1443–1452, 2014.

[20] T. Tourdias, I. Dragonu, Y. Fushimi et al., "Aquaporin 4 correlates with apparent diffusion coefficient and hydrocephalus severity in the rat brain: a combined MRI-histological study," *NeuroImage*, vol. 47, no. 2, pp. 659–666, 2009.

[21] M. Verdurand, G. Bort, V. Tadino, F. Bonnefoi, D. Le Bars, and L. Zimmer, "Automated radiosynthesis of the Pittsburg compound-B using a commercial synthesizer," *Nuclear Medicine Communications*, vol. 29, no. 10, pp. 920–926, 2008.

[22] Y. Liu, L. Zhu, K. Plössl et al., "Optimization of automated radiosynthesis of [^{18}F]AV-45: a new PET imaging agent for Alzheimer's disease," *Nuclear Medicine and Biology*, vol. 37, no. 8, pp. 917–925, 2010.

[23] C.-H. Yao, K.-J. Lin, C.-C. Weng et al., "GMP-compliant automated synthesis of [^{18}F]AV-45 (florbetapir F 18) for imaging β-amyloid plaques in human brain," *Applied Radiation and Isotopes*, vol. 68, no. 12, pp. 2293–2297, 2010.

[24] D. de Paula Faria, M. L. H. Vlaming, S. C. V. M. Copray et al., "PET imaging of disease progression and treatment effects in the experimental autoimmune encephalomyelitis rat model," *Journal of Nuclear Medicine*, vol. 55, no. 8, pp. 1330–1335, 2014.

[25] C. Readhead and L. Hood, "The dysmyelinating mouse mutations shiverer (shi) and myelin deficient (shi mld)," *Behavior Genetics*, vol. 20, no. 2, pp. 213–234, 1990.

[26] I. Tagge, A. O'Connor, P. Chaudhary et al., "Spatio-temporal patterns of demyelination and remyelination in the cuprizone mouse model," *PLoS One*, vol. 11, no. 4, Article ID e0152480, 2016.

[27] L. McCluskey, S. Campbell, D. Anthony, and S. M. Allan, "Inflammatory responses in the rat brain in response to different methods of intra-cerebral administration," *Journal of Neuroimmunology*, vol. 194, no. 1-2, pp. 27–33, 2008.

[28] S. Liachenko and J. Ramu, "Quantification and reproducibility assessment of the regional brain T_2 relaxation in naïve rats at 7T," *Journal of Magnetic Resonance Imaging*, vol. 45, no. 3, pp. 700–709, 2017.

[29] E. Prieto, M. Collantes, M. Delgado et al., "Statistical parametric maps of ^{18}F-FDG PET and 3-D autoradiography in the rat brain: a cross-validation study," *European Journal of Nuclear Medicine and Molecular Imaging*, vol. 38, no. 12, pp. 2228–2237, 2011.

[30] A. M. Pietroboni, T. Carandini, A. Colombi et al., "Amyloid PET as a marker of normal-appearing white matter early damage in multiple sclerosis: correlation with CSF β-amyloid levels and brain volumes," *European Journal of Nuclear Medicine and Molecular Imaging*, vol. 46, no. 2, pp. 280–287, 2019.

[31] J. A. Matías-Guiu, M. N. Cabrera-Martín, J. Matías-Guiu et al., "Amyloid PET imaging in multiple sclerosis: an ^{18}F-florbetaben study," *BMC Neurology*, vol. 15, no. 1, p. 243, 2015.

[32] S. G. Waxman, J. D. Kocsis, and K. C. Nitta, "Lysophosphatidyl choline-induced focal demyelination in the rabbit corpus callosum. Light-microscopic observations," *Journal of the Neurological Sciences*, vol. 44, no. 1, pp. 45–53, 1979.

[33] L. Kalkowski, I. Malysz-Cymborska, D. Golubczyk et al., "MRI-guided intracerebral convection-enhanced injection of gliotoxins to induce focal demyelination in swine," *PLoS One*, vol. 13, no. 10, Article ID e0204650, 2018.

[34] V. Dousset, B. Brochet, A. Vital et al., "Lysolecithin-induced demyelination in primates: preliminary in vivo study with MR and magnetization transfer," *American Journal of Neuroradiology (AJNR)*, vol. 16, no. 2, pp. 225–231, 1995.

Hindawi
Contrast Media & Molecular Imaging
Volume 2019, Article ID 6319476, 9 pages
https://doi.org/10.1155/2019/6319476

Research Article

Noninvasive Ultrasound Monitoring of Embryonic and Fetal Development in *Chinchilla lanigera* to Predict Gestational Age: Preliminary Evaluation of This Species as a Novel Animal Model of Human Pregnancy

A. Greco,[1,2,3] **M. Ragucci**,[2] **R. Liuzzi**,[2] **M. Prota**,[4] **N. Cocchia**,[4] **G. Fatone**,[4] **M. Mancini**,[2] **A. Brunetti**,[1] **and L. Meomartino**[3]

[1]*Department of Advanced Biomedical Science, University of Naples Federico II, Naples 80131, Italy*
[2]*Institute of Biostructure and Bioimaging, CNR, Naples 80131, Italy*
[3]*Interdepartmental Center of Veterinary Radiology, University of Naples Federico II, Naples 80137, Italy*
[4]*Department of Veterinary Medicine and Animal Production, University of Naples Federico II, Naples 80137, Italy*

Correspondence should be addressed to A. Greco; adegreco@unina.it

Received 30 October 2018; Revised 17 February 2019; Accepted 7 May 2019; Published 27 May 2019

Guest Editor: Michael Pedersen

Ultrasound is a noninvasive routine method that allows real-time monitoring of fetal development in utero to determine gestational age and to detect congenital anomalies and multiple pregnancies. To date, the developmental biology of *Chinchilla lanigera* has not yet been characterized. This species has been found to undergo placentation, long gestation, and fetal dimensions similar to those in humans. The aim of this study was to assess the use of high-frequency ultrasound (HFUS) and clinical ultrasound (US) to predict gestational age in chinchillas and evaluate the possibility of this species as a new animal model for the study of human pregnancy. In this study, 35 pregnant females and a total of 74 embryos and fetuses were monitored. Ultrasound examination was feasible in almost all chinchilla subjects. It was possible to monitor the chinchilla embryo with HFUS from embryonic day (E) 15 to 60 and with US from E15 to E115 due to fetus dimensions. The placenta could be visualized and measured with HFUS from E15, but not with US until E30. From E30, the heartbeat became detectable and it was possible to measure fetal biometrics. In the late stages of pregnancy, stomach, eyes, and lenses became visible. Our study demonstrated the importance of employing both techniques while monitoring embryonic and fetal development to obtain an overall and detailed view of all structures and to recognize any malformation at an early stage. Pregnancy in chinchillas can be confirmed as early as the 15th day postmating, and sonographic changes and gestational age are well correlated. The quantitative measurements of fetal and placental growth performed in this study could be useful in setting up a database for comparison with human fetal ultrasounds. We speculate that, in the future, the chinchilla could be used as an animal model for the study of US in human pregnancy.

1. Introduction

The developmental biology of the domesticated long-tailed*Chinchilla lanigera*, a South American species, is not well characterized. Recently, it has been shown that placental and fetal metabolism and the placental vessels of chinchillas are very similar to those of humans [1, 2]. The chinchilla placenta is of the haemomonochorial labyrinthine type and therefore resembles the human villous haemomonochorial placenta, demonstrating that this species is suitable for human obstetric research and for the study of placental and fetal functions [3–5]. Females typically twin (range: 1–6 pups) after a gestation of ~112 days (range: 105–115 days) and give birth to 2–3 litters per year, resulting in relatively fewer offspring than those of other rodent species [6]. The reproductive physiology of the hystricomorph chinchilla is

different from that of myomorphic rodents typically used in biomedical research. At the same time, the chinchilla has a long gestation period and a long estrus cycle compared with other rodents; for example, the gestational period of guinea pigs ranges from 59 to 72 days, that of rats from 21 to 23 days, and that of mice from 19 to 21 days [7–10]. The long gestation and the reduced number of fetuses per gestation allow for better visualization of the embryo, longer longitudinal monitoring, and a more detailed analysis of the placenta and fetal organs. In addition, the weight of the neonatal chinchilla is relatively high (50–70 g) compared to the weight of the adult chinchilla and or of other rodent models, which facilitate instrumental ultrasonographic examination [8].

Ultrasonography is the imaging technique of choice for analyzing embryonic and fetal formation in utero [11–15]. Until a few decades ago, structural phenotyping was based on macroscopic examinations and histological techniques that only allowed the postmortem analysis of static structures. Subsequently, different imaging approaches have become available for the study of small animals, such as ultrasonography, magnetic resonance imaging (MRI), optical imaging, and confocal biomicroscopy [2, 16–18]. The ability of ultrasonography to acquire longitudinal data in real time noninvasively, the ability to analyze the morphology of nearly all the organs, and the ability to perform quantitative measurements on most of the structures have made this imaging modality particularly advantageous in the field of medical imaging. Conventional ultrasonography uses a range of frequencies, from 2 to 15 MHz, with a spatial resolution of 200–500 μm; the limitations of these systems have become evident in several studies on embryonic development in the mouse, particularly during the morphogenesis phase [11]. Technological progress has also led to the development of high-frequency ultrasonography (HFUS), which achieves microscopic resolution and is thus the best imaging technique to monitor the embryonic development of small animals. HFUS systems use higher frequencies, between 40–100 MHz, and have a spatial resolution of approximately 30 μm; therefore, they are useful for imaging developmental processes occurring in small organisms [11, 13].

Previously, our research group used HFUS to monitor embryonic and fetal development in mice. We assessed changes in phenotypic parameters during pregnancy and evaluated physiological fetal parameters of the principal organ development to build a database of normal structural and functional parameters of mouse development [12, 13]. Due to the chinchilla embryos' dimensions, it was not possible to monitor the entire pregnancy with HFUS (with the exception of some specific parameters), but it was necessary to use conventional ultrasound in the advanced stage of pregnancy. Up until today, there are no published reports on the use of ultrasound to monitor the fetal development of chinchillas. The aim of our research was to acquire new knowledge of the reproductive physiology of chinchillas based on the gestational similarities with humans and to assess whether this species could potentially be used in obstetric biomedical research.

2. Materials and Methods

The study was performed with the consent of chinchilla owners and breeders. Ethical clearance (50380-2018) from the Ethical Committee for Animal Experimentation of the University of Naples Federico II was obtained.

Healthy pregnant chinchillas were analyzed at the Interdepartmental Radiology Center of the University of Naples Federico II and at the La Plata breeding center in Cupello (CH), Italy.

We divided the pregnancy into four stages: very early stage (T1) from embryonic day (E) E15 to E30, early stage (T2) from E31 to E46, intermediate stage (T3) from E47 to E70, and advanced stage (T4) from E71 to E115. The pregnancy stage of the monitored females was determined by the date of their last birth. The chinchilla, as well as the guinea pig, begins a new estrous 12–48 h after birth [6]. From this date, we assumed a period of approximately 115 days of gestation; at parturition, both the effective time of conception and the stages of gestation were retrospectively confirmed.

2.1. Ultrasound Imaging. All ultrasound (US) exams were performed by an experienced veterinary ultrasonographer on awake subjects gently restrained to avoid any possible stress to the pregnant females. We monitored 35 pregnant females with a mean age of 3.5 years. Of those, 15 were in their second coupling, 10 in their first, and 10 in their third. The animals used for this study underwent a trichotomy of the pelvic and abdominal area for which no sedation was necessary since the chinchilla is a docile animal. All measurements were made by the same ultrasonographer to ensure consistency during the investigation. In each pregnant female, 2-3 embryos were imaged. The number of fetuses ultrasonographically assessed was compared to the actual number of fetuses at parturition, as communicated to us by the breeders and owners. After obtaining the US results of the entire study, the pregnancy was divided into four stages in order to longitudinally analyze the same morphometric parameter. Each chinchilla was monitored with US in a period ranging from E15 to E115, for a total of four US examinations for each chinchilla. US was performed every two weeks at the beginning of the pregnancy, at T1 and T2, and about every 40 days during T3 and T4, to avoid excessive stress on the animals. The exact day of pregnancy, in which US was performed, was retrospectively determined only after the delivery date, which was communicated to us by the breeders and the owners.

During stage T1, we used the high-frequency ultrasound system, Vevo 770 (Visualsonics, Canada), equipped with a 40 MHz high-resolution linear transducer (focal length 6 mm, depth of penetration 5–15 mm, resolution 30–40 mm axial, and 70–90 mm lateral). During the other stages, we used a US device (MyLab 30, Esaote, Firenze, IT) equipped with a 12 MHz linear probe. A series of measurements were obtained: the longitudinal and transversal diameters of the gestational sacs and the diameter and thickness of the placenta at T1. At T2, T3, and T4, we measured the size of the

gestational sacs, the diameter and thickness of the placenta, and the crown-rump length (CRL). Furthermore, we measured the head diameter (HD), the body diameter (BD), the occipital-snout length (OSL), and the heart rate (HR); the femur length (FL) and the stomach were measured from T3, and eye and lens diameter were measured at T3.

2.2. Statistical Analysis. Continuous variables were reported as the mean ± standard deviation. Univariate analysis between each variable and embryonic day was performed using Spearman's rank correlation (Rs). Linear regression analysis was used to assess the relationships between embryonic variables and gestational time. A p value < 0.05 was considered statistically significant. Statistical analyses were performed using MedCalc 18.2.1 software (Ostend, Belgium).

3. Results

3.1. Ultrasonographic Findings. The ultrasonographic examination was feasible in all chinchilla subjects. Every ultrasonographic examination lasted approximately 10 min. Both techniques, HFUS and US, were able to diagnose pregnancy. However, not all fetal structures could be visualized with both techniques. In the first stage (T1), we found 74 embryos, but at the delivery, this number decreased as the 35 chinchillas effectively delivered 67 cubs. Considering the 35 pregnant females, the pregnancy loss was 11%. Since it was not possible to obtain the measurements of each parameter at every ultrasonographic examination, we reported the exact number of fetuses, for which each parameter was measured (Table 1).

It was possible to monitor the chinchilla embryos with HFUS from E15 to E60 and with US from E15 to E115. This was due to the increasing fetal dimensions that do not permit accurate measurement of several fetal structures with HFUS. The assessability of the analyzed fetal structures depended on their dimensions and thickness: the placenta was 100%, the HD was 82%, the CRL was 57%, and the femur was 26%. We summarized the assessed structures per gestational stage and the employed ultrasound technique in Table 2.

At T1, from E15 to E30, it was possible to visualize the gestational sac with both HFUS and US. However, the placental diameter and thickness were visualized and measured only with HFUS because the placenta at this stage is not yet discoidal in shape. In the very early stage, it was also possible to identify and measure the gestational sac and to distinguish the primitive node (Figure 1).

At T2, from E30 to E46, the placental diameter and the placental thickness were visualized with US. From E30, it was possible to measure the CRL with both HFUS and US (Figure 2), and from E38, the BD was also measurable. All these parameters were better visualized with HFUS at T2. The OSL, in particular, could be visualized and measured from E40 because, at this gestational age, the head becomes well defined.

Table 1: Number of embryos for each measurement.

Type of measurement	Gestational age (days)	Number of embryos measured
Longitudinal sac diameter	E15–E49	44
Transversal sac diameter	E15–E49	44
Placental diameter	E15–E107	74 to 67
Placental thickness	E15–E107	74 to 67
Lens	E60–E107	23
Eye	E55–E107	22
Head diameter	E31–E107	61
Occipital snout length	E40–E107	61
Heart rate (BPM)	E31–E107	55
Stomach	E55–E107	33
Longitudinal body diameter	E38–E107	61
Femur	E66–E107	19
Crown-rump length	E31–E70	42

E: embryonic day; BPM: beats per minute.

Table 2: Ultrasound visible fetal anatomic structure per gestational stage.

Stage	Anatomic embryo/fetal structure	Ultrasound techniques
T1 (E15–E30)	Longitudinal sac diameter	HFUS, US
	Transversal sac diameter	HFUS, US
	Placental diameter	HFUS
	Placental thickness	HFUS
T2 (E31–E46)	Longitudinal sac diameter	HFUS, US
	Transversal sac diameter	HFUS, US
	Placental diameter	HFUS, US
	Placental thickness	HFUS, US
	Head diameter	HFUS, US
	Occipital snout length	HFUS, US
	Heart rate (BPM)	HFUS, US
	Longitudinal body diameter	HFUS, US
	Crown-rump length	HFUS, US
T3 (E47–E70)	Placental diameter	HFUS, US
	Placental thickness	HFUS, US
	Lens	HFUS, US
	Eye	HFUS, US
	Head diameter	HFUS, US
	Occipital snout length	HFUS, US
	Heart rate (BPM)	HFUS, US
	Stomach	HFUS, US
	Longitudinal body diameter	HFUS, US
	Femur	HFUS, US
	Crown-rump length	US
T4 (E71–E115)	Placental diameter	US
	Placental thickness	US
	Lens	US
	Eye	US
	Head diameter	US
	Occipital snout length	US
	Heart rate (BPM)	US
	Stomach	US
	Longitudinal body diameter	US
	Femur	US
	Crown-rump length	US

BPM: beats per minute.

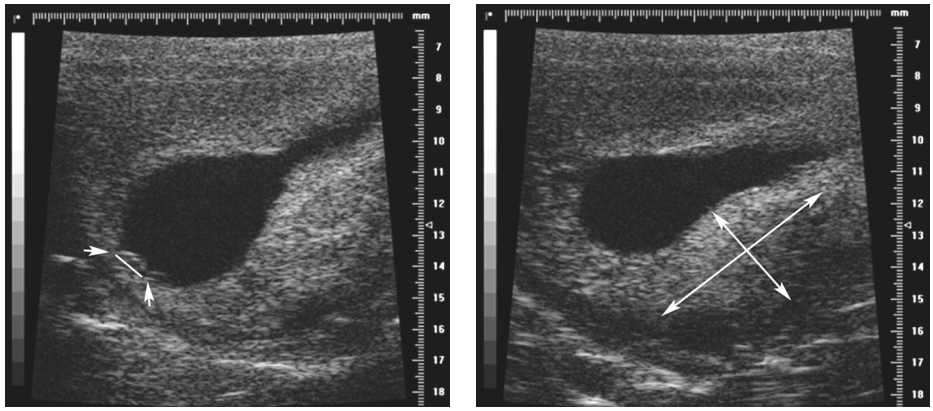

(a) (b)

Figure 1: HFUS B-mode image at E15. (a) An embryo 1.06 mm in diameter (arrow) is evident. (b) The placenta (4.24 × 9.17 mm).

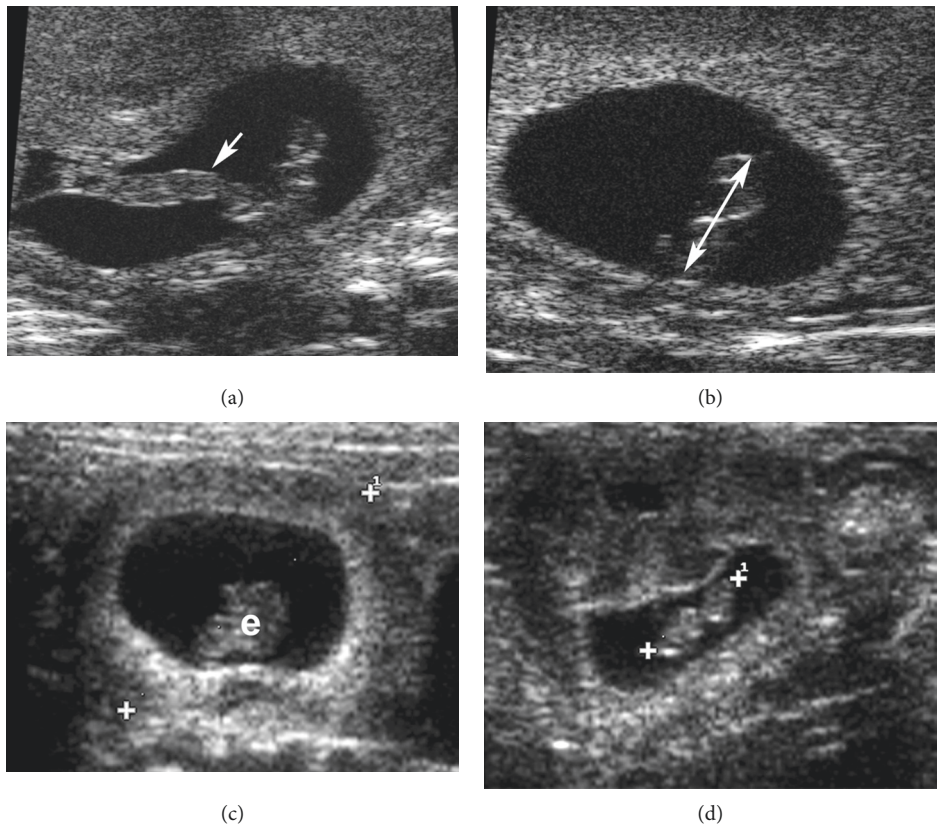

(a) (b)

(c) (d)

Figure 2: Images of a chinchilla embryo at embryonic day 31 (E31). HFUS B-mode: (a) the umbilical cord (arrow) is evident; (b) measurement of the crown-rump length (CRL) (double-headed arrow) (3.34 mm). US B-mode: (c) image of the embryo (e) and the gestational sac diameter (GSD) (16 mm); (d) measurement of the CRL (6 mm).

At E30, the heartbeat was detectable for the first time with HFUS, and it was possible to visualize the completed neural tube at E46 (Figure 3).

From E55, it was possible to detect the stomach, the eyes, and the lenses (Figure 4).

At E66, the femur became clearly visible and measurable because of increased mineralization (Figure 5(a)). In the advanced pregnancy stage T4 (E75–E115), it was no longer possible to measure the CRL due to fetal dimensions, bone mineralization was pronounced, and the dimensions of eyes and lenses were approximately the same as those in newborns (Figure 5).

From the beginning of the intermediate stage T3 (E47–E70), it was possible to monitor the chinchillas only with US due to the growing dimensions of the fetal structures. However, we were able to use HFUS to measure the anteroposterior and laterolateral lens diameters until E115. HFUS in this stage of gestation (E60)

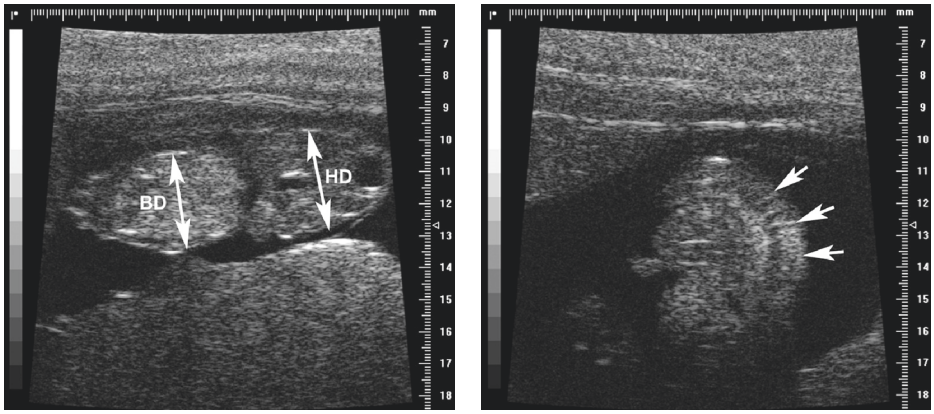

(a) (b)

Figure 3: HFUS B-mode image of the embryo at embryonic day 46. (a) The head diameter (HD) (4.3 mm) and the body diameter (BD) (3.1 mm) are highlighted (arrows); (b) the neural crest (arrows) is visible.

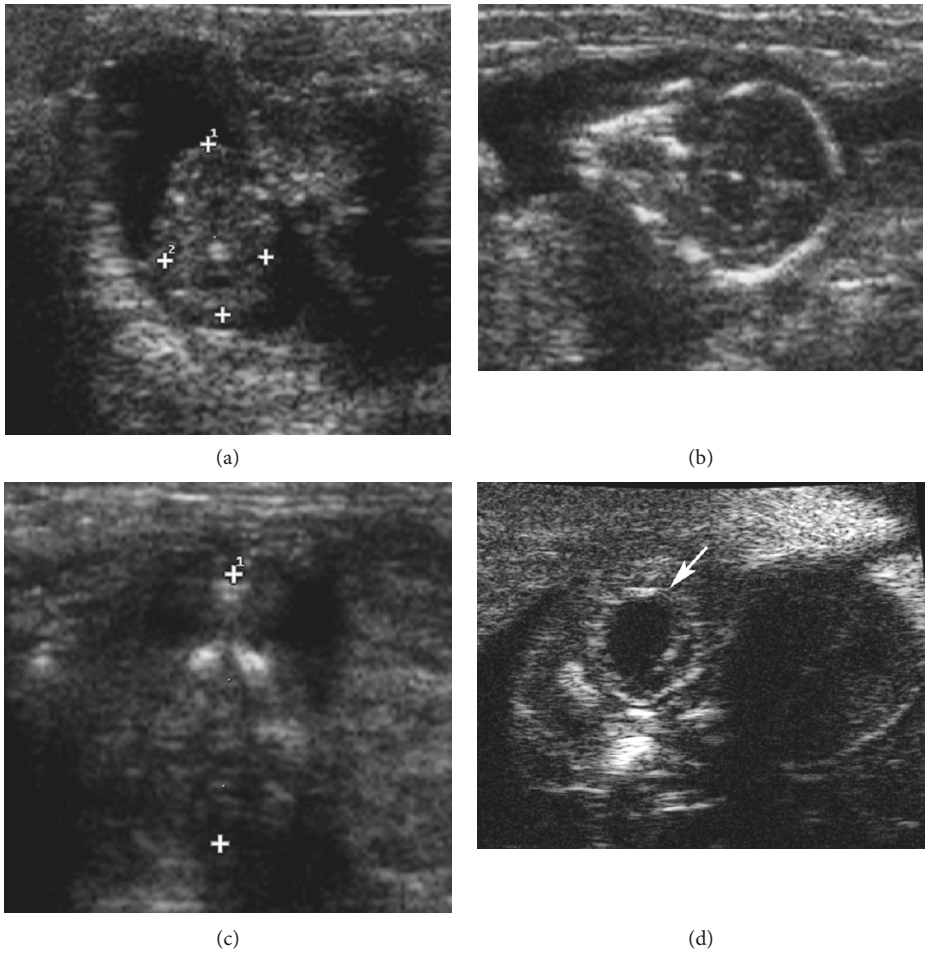

(a) (b)

(c) (d)

Figure 4: Embryonic days 49–60. US B-mode: (a) images of the head at embryonic day 49 with the measurements of the head diameter (HD) (short axis) and occipital to snout length (OSL) (long axis) (9.1 × 5.3 mm); (b) head US aspect at embryonic day 49: skull bones are hyperechoic but still not mineralized; (c) measurement of the occipital to snout length (OSL) at embryonic day 67 (12.6 mm); HFUS B-mode: (d) the eyes (arrow) and the ears are visible at E60.

was also useful to visualize the interventricular septum of the heart and to quantify the HR until the end of pregnancy.

3.2. Statistical Analysis. Summarizing the most important results of the first two stages (T1 and T2), the diameter of the placenta increases from 0.8 cm to 1.6 cm (about 2-fold) and

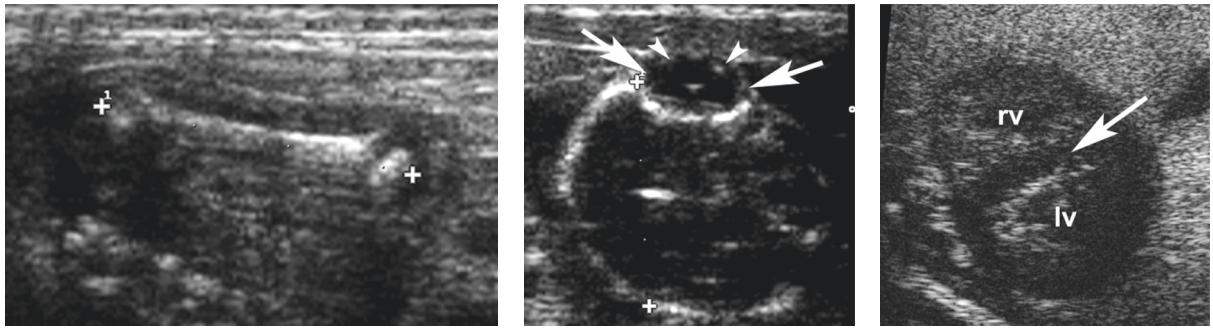

(a) (b) (c)

Figure 5: Embryonic days 98–102. US B-mode and HFUS: (a) measurement of the femur (16.5 mm); (b) measurement of the eye (arrows) and lens (arrowheads); (c) HFUS B-mode image of the heart (rv: right ventriculum; lv: left ventriculum) at embryonic day 102. The interventricular septum (arrow) is visible.

the thickness of the placenta increases from 0.4 to 1.21 cm (about 3-fold). A plot of the analysis of the diameter and the thickness of the placenta, measured longitudinally in the four stages, is presented in Figure 6.

The longitudinal size of the gestational sacs increased from 1.17 to 2.39 cm (2-fold) until E49. Also, the CRL, HD, and BD gradually increased (CRL: 0.7 to 2.7, about 4-fold; HD: 0.25 to 0.65, about 5-fold; BD: 0.85 to 1.9 cm, about 2-fold) till the end of the pregnancy (Figures 2 and 3). The precise measurements of the parameters from the first day of pregnancy to the last are reported in Table 3.

All structural measurements, except for femoral length, were significantly correlated with gestational age. The results of correlation analysis are reported in Table 4.

Based on the period during which it was possible to measure the aforementioned variables simultaneously, they embryos measured were placed in three groups for the regression analysis: group 1 included variables measurable between time T1 to T3 (i.e.,gestational sac diameter and placental diameter and thickness); group 2 included variables measurable between time T2 to T3 (i.e.,placental diameter and thickness, CRL, HD, BD, OSL, and HR); group 3 included variables measurable between time T2 to T4 (i.e.,placental diameter and thickness, BD, OSL, HD, and HR). Using this analysis, three models for predicting gestational age were obtained (Table 5).

4. Discussion

We examined embryo and fetus development in the *C. lanigera* using an ultrasonographic technique, and we predicted gestational age with the analysis of ultrasound parameters.

Ultrasonography is a noninvasive method that provides a longitudinal, real time, and detailed morphological evaluation of fetuses in vivo. Furthermore, US is quick and less expensive than other imaging modalities when screening for neonatal defects. We performed a longitudinal, qualitative, and morphometric evaluation of chinchilla embryonic parameters from E15 to the last day of pregnancy using HFUS and US. As in human obstetrics, we analyzed different morphometric parameters useful to predict the gestational age of the fetus (such as the CRL or the HR) and others like the HD, the OSL, or the BD, embryo anatomical size measurements, position of the placenta, and structures, which are useful for predicting anomalies in the unborn child. The ultrasonographic exam was feasible in all subjects, even when subjects were awake. The main difficulty encountered when performing the US exam was related to the anatomy of the chinchilla, which has a highly developed caecum that can sometimes hinder the sight of some structures of interest. Furthermore, the fetuses of chinchillas have a big head that, especially in the last part of pregnancy, when mineralization is advanced, can obstruct the visualization of other anatomical structures of the fetus. Lastly, US is a subjective technique in which the expertise and capabilities of the operator are of paramount importance. In further studies, it would be useful to compare US evaluation performed by two or more operators to assess reliability, sensitivity, and specificity of the method.

Since the animals examined in this study were bred or owned as pets, we had to perform our exams on awake subjects. This circumstance and the abovementioned anatomic characteristics of the chinchilla limited the analysis of some anatomical structures. However, the morphometric data we obtained for the different parameters during pregnancy were consistent and reproducible within the same gestational stage, and no female showed any signs of stress during or following US examinations. All subjects completed their pregnancies although some fetuses were reabsorbed. Studies performed in mice under general anesthesia are more detailed; however, the use of anesthetics often affects the newborn offspring, thus disrupting the possible comparison with human ultrasound findings [19].

Our intent was to protect the well-being of the cubs and fetuses and to demonstrate the noninvasiveness and feasibility of ultrasonographic examination, which can also be performed on awake subjects. In our study, some observation days were missed because we performed only four US examinations per chinchilla (from E15 to E115). This was done to avoid excessive stress on the pregnant females. Also limiting in our study is that, in the 115 days, we performed the first two US analyses in the first 115 days, about every 2 weeks and then about every 40 days thereafter, so we

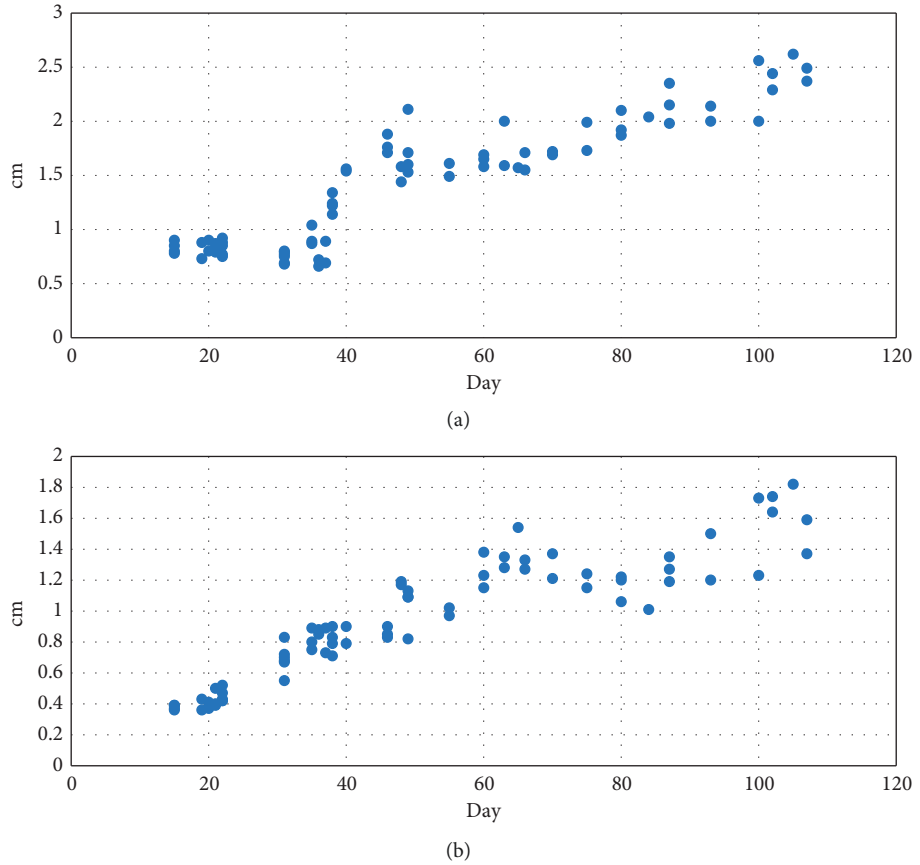

Figure 6: Plot of the US measurement of the placental diameter (a) and of the placental thickness (b) obtained from E15 to E115.

Table 3: Morphometric evaluation (in mm).

Type of measurement	Measurement at the beginning of pregnancy (mean ± SD)	Measurement at the end of pregnancy (mean ± SD)
Longitudinal sac diameter	11.7 ± 1.6 (E15)	23.9 ± 2.9 (E49)
Transversal sac diameter	8.9 ± 2.0 (E15)	18.6 ± 1.8 (E49)
Placental diameter	8.3 ± 0.6 (E15)	20.5 ± 5.6 (E107)
Placental thickness	4.1 ± 0.5 (E15)	13.6 ± 2.4 (E107)
Lens diameter	1.4 ± 0.3 (E60)	2.2 ± 0.8 (E107)
Eye axis	3.2 ± 0.6 (E55)	4.9 ± 1.2 (E107)
Head diameter	2.6 ± 0.7 (E31)	16.4 ± 1.7 (E107)
Occipital to snout length	5.0 ± 0.4 (E40)	26.9 ± 5.2 (E107)
Heart rate (BPM)	154 ± 13.8 (E31)	138 ± 39 (E107)
Stomach diameter	3.7 ± 1.0 (E55)	7.3 ± 2.1 (E107)
Body diameter (long axis)	8.5 ± 2.2 (E38)	19.0 ± 4.3 (E107)
Femur length	9.4 ± 0.7 (E66)	14.5 ± 4.3 (E107)
Crown-rump length	7.1 ± 3.3 (E31)	27.0 ± 7.8 (E70)

BPM: beats per minute.

lucked some temporal points of observation. This was due to difficulties reaching the breeding center and also because the chinchillas used for the study were domesticated animals and not experimental animals. Thus, we adjusted our research to suit the availability of the breeding center and owners.

We used a best-fit regression coefficient to analyze which parameters could be predicted for each gestational age. Based on our results, the placental thickness at T1–T3, the HR, and the CRL at T2-T3, and the HD and HR at T2–T4 could be used to predict the exact gestational age of the chinchilla fetuses. However, some parameters, such as the femoral length, which are used to predict gestational age in human pregnancy, have to be further evaluated to increase casuistry. Furthermore, other parameters will likely be needed to better predict gestational age. For this reason, it is useful to have a precise database of physiological morphometric parameters of embryo and fetal development

Table 4: Spearman's correlation coefficient and significance of each embryonic parameter.

Embryonic structure	Correlation coefficient	p
Longitudinal sac diameter	0.765	<0.0001
Transversal sac diameter	0.683	<0.0001
Placental diameter	0.841	<0.0001
Placental thickness	0.902	<0.0001
Lens diameter	0.639	0.0014
Eye axis	0.313	0.1914
Head diameter	0.942	<0.0001
Occipital to snout length	0.923	<0.0001
Heart rate (BPM)	−0.362	0.0062
Stomach diameter	0.517	0.0114
Body diameter (long axis)	0.919	<0.0001
Crown-rump length	0.71 ± 0.33 (E31)	2.70 ± 0.78 (E70)

BPM: beats per minute.

Table 5: Best-fit regression coefficient and standard error for the three groups of variables.

Gestation time	Model	Set of parameters	Coefficient	Standard error	p
T1–T3	1	Placental thickness	2.54	0.15	<0.0001
		Constant	0.007		
T2-T3	2	Heart rate in beats per minute	−0.009	0.001	<0.0001
		Crown-rump length	0.30	0.03	<0.0001
		Constant	3.19		
T2–T4	3	Head diameter	1.26	0.06	<0.0001
		Heart rate in beats per minute	−0.004	0.001	0.0008
		Constant	2.34		

Model 1 uses placental thickness to predict the gestational age from T1 to T3. Model 2 uses HR and CRL to predict gestational age from T2 to T3. Finally, model 3 uses HD and HR to predict gestational age from T2 to T4.

during chinchilla pregnancy, even if divided in stages and not in days, in order to diagnose pathological conditions that could occur.

Since 1947, the efficiency of animal models for the study of human pathologies of pregnancy has been investigated. Even today an adequate model for the study of human pregnancy has yet to be found [20]. A recent study shows that, in animal perinatology, the use of animal models does not give adequate mathematical correlations with human pregnancy preterm birth [21]. The choice of the right animal model in human obstetrics is challenging because there are several aspects to consider. The duration of gestation, the number of fetuses for each pregnancy, and the placental morphology are all important parameters to evaluate when comparing placentation and fetal morphology between rodents and humans. Other aspects that should not be underestimated are the management costs of the animal, the ease of animal housing, and the legislation (Directive 2010/63/EU) that regulates the use of one species instead of another as an animal model for biomedical research.

The chinchilla might be more suitable as an animal model for human obstetrics than the guinea pig and other rodents because of the longer duration of pregnancy (105–115 days) [22–24]. The female chinchilla's placenta is comparable to the human haemomonochorial placenta, which is formed of only one layer of syncytiotrophoblasts, unlike the other rodents [2]. Furthermore, chinchilla cubs are fully developed, covered with hair, have already developed sight and hearing, and are able to move a few hours after birth. These characteristics make chinchilla development resemble humans, who have a longer intrauterine development than myomorphic rodents and rabbits. Finally, the reduced number of offspring (1–6, on average 1 or 2 cubs per gestation) facilitates monitoring of the same fetus with US, avoiding errors due to the presence of numerous fetuses in a single pregnancy and allowing a higher spatial resolution and sensitivity using imaging techniques. The discordant data between the number of US examinations and the number of fetuses communicated by the owners and breeders are probably due to fetal reabsorption that often occurs in this species [25].

5. Conclusions

In conclusion, US lasts only a few minutes and is well tolerated in chinchillas, which have proved to be a suitable animal model for the study of human pregnancy and biomedical research in general [25]. Our research has provided important data, which allow the division of the gestation in four stages. This is particularly relevant in chinchillas since estrus is often silent and does not permit detection of the exact time of mating; with ultrasound, it is possible to establish the exact stage of pregnancy because of the reliability of morphometric measurements. One limitation of the study is the fact that we analyzed each chinchilla only four times during the entire pregnancy, which resulted in some

longitudinal observations being missed. Further studies will be carried out by our group to obtain all morphometric measurements that will cover the entire pregnancy of the chinchilla.

Data Availability

The ultrasound data used to support the findings of this study are included within the article.

Conflicts of Interest

The authors declare that there are no conflicts of interest regarding the publication of this paper.

Acknowledgments

The authors would like to thank Mr. Francesco Tolomeo and Mr. Umberto Monaco of La Plata Breeding Center for their kind collaboration in this study. The authors would also like to thank Editage (http:\\www.editage.com) for English language editing. This study was funded by the Interdepartmental Center of Veterinary Radiology and the Department of Advanced Biomedical Science, University of Naples Federico II.

References

[1] S. L. Johnsen, T. Wilsgaard, S. Rasmussen, R. Sollien, and T. Kiserud, "Longitudinal reference charts for growth of the fetal head, abdomen and femur," *European Journal of Obstetrics & Gynecology and Reproductive Biology*, vol. 127, no. 2, pp. 172–185, 2006.

[2] E. Mikkelsen, H. Lauridsen, P. R. Nielsen et al., "The chinchilla as novel animal model of pregnancy," *Royal Society Open Science*, vol. 4, no. 4, article 161098, 2016.

[3] P. Grigsby, "Animal models to study placental development and function throughout normal and dysfunctional human pregnancy," *Seminars in Reproductive Medicine*, vol. 34, no. 1, pp. 011–016, 2016.

[4] B. F. King and F. D. Tibbitts, "The fine structure of the chinchilla placenta," *American Journal of Anatomy*, vol. 145, no. 1, pp. 33–56, 1976.

[5] F. D. Tibbitts and H. H. Hillemann, "The development and histology of the chinchilla placentae," *Journal of Morphology*, vol. 105, no. 2, pp. 317–365, 1959.

[6] G. F. Mastromonaco, V. I. Cantarelli, M. G. Galeano, N. S. Bourguignon, C. Gilman, and M. F. Ponzio, "Non-invasive endocrine monitoring of ovarian and adrenal activity in chinchilla (*Chinchilla lanigera*) females during pregnancy, parturition and early post-partum period," *General and Comparative Endocrinology*, vol. 213, pp. 81–89, 2015.

[7] E. A. Bonney, "Demystifying animal models of adverse pregnancy outcome: touching bench and bedside," *American Journal of Reproductive Immunology*, vol. 69, no. 6, pp. 576–584, 2013.

[8] P. Georgiades, A. C. Ferguson-Smith, and G. J. Burton, "Comparative developmental anatomy of the murine and human definitive placentae," *Placenta*, vol. 23, no. 1, pp. 3–19, 2002.

[9] M. J. Soares, D. Chakraborty, M. A. Karim Rumi, T. Konno, and S. J. Renaud, "Rat placentation: an experimental model for investigating the hemochorial maternal-fetal interface," *Placenta*, vol. 33, no. 4, pp. 233–243, 2012.

[10] L. J. Friesen-Waldner, K. J. Sinclair, T. P. Wade et al., "Hyperpolarized [1-13C] pyruvate MRI for noninvasive examination of placental metabolism and nutrient transport: a feasibility study in pregnant Guinea pigs," *Journal of Magnetic Resonance Imaging*, vol. 43, no. 3, pp. 750–755, 2015.

[11] K. K. Shung, "High frequency ultrasonic imaging," *Journal of Medical Ultrasound*, vol. 17, no. 1, pp. 25–30, 2009.

[12] C.-P. Chang, L. Chen, and G. R. Crabtree, "Sonographic staging of the developmental status of mouse embryos in utero," *Genesis*, vol. 36, no. 1, pp. 7–11, 2003.

[13] A. Greco, M. Ragucci, A. R. D. Coda et al., "High frequency ultrasound for in vivo pregnancy diagnosis and staging of placental and fetal development in mice," *PLos One*, vol. 8, no. 10, Article ID e77205, 2013.

[14] A. Greco, A. R. D. Coda, S. Albanese et al., "High-frequency ultrasound for the study of early mouse embryonic cardiovascular system," *Reproductive Sciences*, vol. 22, no. 12, pp. 1649–1655, 2015.

[15] D. Marinac-Dabic, C. J. Krulewitch, and R. M. Moore, "The safety of prenatal ultrasound exposure in human studies," *Epidemiology*, vol. 13, pp. S19–S22, 2002.

[16] Y. Q. Zhou, F. S. Foster, D. W. Qu, M. Zhang, K. A. Harasiewicz, and S. L. Adamson, "Applications for multifrequency ultrasound biomicroscopy in mice from implantation to adulthood," *Physiological Genomics*, vol. 10, no. 2, pp. 113–126, 2002.

[17] J. Mu, J. C. Slevin, D. Qu et al., "In vivo quantification of embryonic and placental growth during gestation in mice using micro-ultrasound," *Reproductive Biology and Endocrinology*, vol. 6, no. 1, pp. 34–47, 2008.

[18] D. H. Turnbull, T. S. Bloomfield, H. S. Baldwin, F. S. Foster, and A. L. Joyner, "Ultrasound backscatter microscope analysis of early mouse embryonic brain development," *Proceedings of the National Academy of Sciences*, vol. 92, no. 6, pp. 2239–2243, 1995.

[19] S. Lee, W. Chung, H. Park et al., "Single and multiple sevoflurane exposures during pregnancy and offspring behavior in mice," *Pediatric Anesthesia*, vol. 27, no. 7, pp. 742–751, 2017.

[20] H. C. Miller, "The effect of pregnancy complicated by alloxan diabetes on the fetuses of dogs, rabbits and rats," *Endocrinology*, vol. 40, no. 4, pp. 251–258, 1947.

[21] B. W. Nielsen, E. A. Bonney, B. D. Pearce, L. R. Donahue, I. N. Sarkar, and For the Preterm Birth International Collaborative (PREBIC), "A cross-species analysis of animal models for the investigation of preterm birth mechanisms," *Reproductive Sciences*, vol. 23, no. 4, pp. 482–491, 2016.

[22] J. E. Jiménez, "The extirpation and current status of wild chinchillas *Chinchilla lanigera* and c. brevicaudata," *Biological Conservation*, vol. 77, no. 1, pp. 1–6, 1996.

[23] J. M. Busso, M. F. Ponzio, M. F. De Cuneo et al., "Non-invasive monitoring of ovarian endocrine activity in the chinchilla (*Chinchilla lanigera*)," *General and Comparative Endocrinology*, vol. 150, pp. 288–287, 2007.

[24] T. Bekyürek, N. Liman, and G. Bayram, "Diagnosis of sexual cycle by means of vaginal smear method in the chinchilla (*Chinchilla lanigera*)," *Laboratory Animals*, vol. 36, no. 1, pp. 51–60, 2002.

[25] M. D. Andersen, A. K. O. Alstrup, C. Sondergaard et al., *Animal Model of Fetal Medicine and Obstetrics in Intechopen*, Chapter 16, IntechOpen, London, 2018.

Hindawi
Contrast Media & Molecular Imaging
Volume 2019, Article ID 9787340, 6 pages
https://doi.org/10.1155/2019/9787340

Research Article

Biodistribution of [^{11}C]-Metformin and mRNA Expression of Placentae Metformin Transporters in the Pregnant Chinchilla

Maria Dahl Overgaard,[1] **Christina Søndergaard Duvald**,[1] **Mikkel Holm Vendelbo**,[2,3] **Steen Bønløkke Pedersen**,[4] **Steen Jakobsen**,[2] **Aage Kristian Olsen Alstrup**,[2] **Emmeli Mikkelsen**,[1] **Per Glud Ovesen**,[5] **and Michael Pedersen**[1]

[1]*Comparative Medicine Lab, Aarhus University Hospital, Aarhus, Denmark*
[2]*Department of Nuclear Medicine and PET Centre, Aarhus University Hospital, Aarhus, Denmark*
[3]*Department of Biomedicine, Aarhus University Hospital, Aarhus, Denmark*
[4]*Endocrinology and Internal Medicine, Aarhus University Hospital, Aarhus, Denmark*
[5]*Department of Obstetrics and Gynecology, Aarhus University Hospital, Aarhus, Denmark*

Correspondence should be addressed to Michael Pedersen; michael@clin.au.dk

Received 3 January 2019; Revised 18 March 2019; Accepted 3 April 2019; Published 30 April 2019

Academic Editor: Alexey P. Kostikov

Background. While metformin is the first-line pharmacological treatment of diabetes mellitus type 2, this drug is not considered safe to use in pregnant women because of its unknown consequences for the fetus. In this study, we aimed to investigate the biodistribution of metformin in the pregnant chinchilla, a species exhibiting placental characteristics comparable with the pregnant woman. Furthermore, we aimed to investigate the expression of metformin transporters in humans and chinchillas, respectively, in order to evaluate the pregnant chinchilla as a novel animal model for the use of metformin in pregnancy. *Methods*. Three chinchillas in the last part of gestation were injected with [^{11}C]-metformin and scanned by PET/CT for 70 minutes to visualize the distribution. To investigate the difference in expression of placenta transporters between humans and chinchillas, PCR was performed on samples from five chinchilla placentae and seven human placentae. *Results*. Dynamic PET with [^{11}C]-metformin showed that the metformin distribution in chinchillas was similar to that in nonpregnant humans, with signal from kidneys, liver, bladder, and submandibular glands. Conversely, no radioactive signal was observed from the fetuses, and no metformin was accumulated in the chinchilla fetus when measuring the SUV. PCR of placental mRNA showed that the human placentae expressed OCT3, whereas the chinchilla placentae expressed OCT1. *Conclusion*. Since metformin did not pass the placenta barrier in the pregnant chinchilla, as it is known to do in humans, we do not suggest the chinchilla as a future animal model of metformin in pregnancies.

1. Introduction

Today, 5% of all pregnant women develop gestational diabetes mellitus (GDM), and this prevalence is expected to increase due to the increasing proportion of overweight and obesity [1]. Diabetes in pregnancy can lead to adverse complications for both the mother and the unborn child [2]. Subcutaneous insulin injection is often used to control the blood glucose levels in pregnant women suffering from GDM. The insulin requirement changes throughout pregnancy, and treatment requires regular monitoring. Managing GDM with insulin injections can be challenging, particularly for those who have never used insulin injections before, leading to the risk of poor compliance. Alternatively, it is much easier to prescribe an antidiabetic oral drug. Metformin is first-line pharmacological treatment of diabetes mellitus type 2 (DM2) [3] and polycystic ovary syndrome (PCOS). It has few side effects, mainly gastrointestinal symptoms such as diarrhea and nausea [4], and is associated with a low risk of hypoglycemia and lactate acidosis [5].

Because metformin is a cationic base at physiological pH and has a hydrophilic structure, the passive diffusion through cell membranes is negligible. Instead, transporters must mediate uptake of metformin, both distribution and elimination. Metformin is substrate of different kinds of solute carrier transporters (SLC): organic cation transporters (OCT1, OCT2, and OCT3) and multidrug and toxin extrusion transporters (MATE1 and MATE2) [6]. It has been widely used in pregnancy for more than 40 years [7]. However, the pharmacokinetics of metformin and especially the biodistribution are not fully understood. Metformin passes across the placenta, and studies using umbilical cord blood samples from women treated with metformin during third trimester showed that the fetus was exposed to concentrations approaching those in the maternal circulation [8]. Two recent reviews concluded that metformin had no short-term adverse effects on pregnancy, potential benefits in the neonatal period, but limited long-term follow-up information [7, 9].

In the human, metformin is excreted unchanged in urine. In the fetus, the amniotic fluid is derived from fetal urination, and the amniotic fluid is primarily eliminated through fetal swallowing. The fetal metabolism of metformin is unknown; however, it could be speculated that metformin is excreted to the amniotic fluid, swallowed by the fetus and then reabsorbed to the fetal circulation. Hence, the fetus theoretically could have an increased concentration or accumulation of metformin. Thus, a recent study showed that children aged 5–10 years exposed to metformin in utero have higher body mass indices and measures of central adiposity, and increased risk of obesity [10]. Metformin treatment in pregnancy is a controversial option, and this drug is therefore not used during pregnancy in many countries [7].

For metformin to cross placenta, there must be both influx and efflux transporters in the trophoblast cells (Figure 1) [11]. The exact mechanism of transplacental metformin transport is not known. In order to study metformin during pregnancy, an appropriate animal model is needed. Such animal model must be carefully considered to investigate transplacental transports of substances. Krogh's principle should be applied for every pathological or physiological condition, and the most appropriate animal model must be chosen. An appropriate animal model of pregnancy should account for the number of fetuses, the length of gestation period, and the placental structure. The *Chinchilla lanigera* poses excellent characteristics in this matter, carrying only one or two cubs and having a hemomonochorial placenta barrier like the human placenta (Figure 1) [12]. Furthermore, the chinchilla has a long gestation period (115 days), and the offspring are precocious (matured neurodevelopment at birth, e.g., born with open eyes) like the human newborn [13]. Finally, the relatively large size of the chinchilla fetuses allows for the use of diagnostic imaging methods [12]. These characteristics suggest that the chinchilla is superior to other rodents as animal model of human pregnancy.

The aim of this study was to investigate the biodistribution and pharmacokinetics of metformin in a human translational animal model. We address this aim using a noninvasive approach, employing ^{11}C-labeled metformin ([^{11}C]-metformin) [14, 15] and positron emission tomography (PET) [15] in the pregnant chinchilla. [^{11}C]-metformin has previously been used to study biodistribution in humans but never during pregnancy.

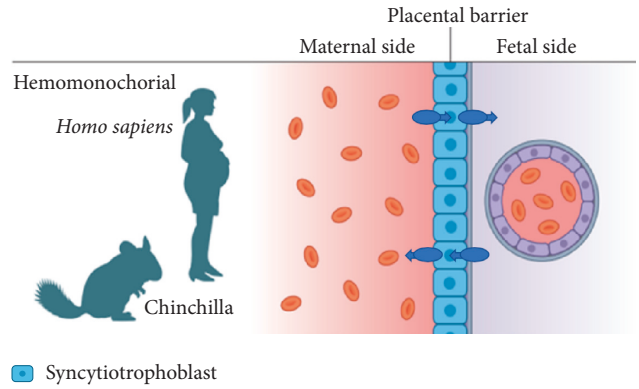

Figure 1: Transport of metformin across the placenta barrier depends on both influx transporters and efflux transporters. Influx and efflux transporters on both sides are necessary for bidirectional transport across the placenta. The placenta barrier of humans and chinchillas is called hemomonochorial because the maternal and fetal blood are divided by only one layer of syncytiotrophoblasts.

2. Materials and Methods

2.1. Animal Handling. We included clinically healthy, pregnant chinchillas purchased from a local commercial breeder. They were single housed, fed with a chinchilla pellet diet, and had ad libitum access to tap water. The environmental temperature was around 20°C with 12 hours of light cycles. The animals were fasted 6 hours prior to anesthesia.

2.2. PET-CT Examination. Three pregnant chinchillas in the last part of their pregnancy (gestation days 82–93) with a mean weight of 841 g (774–902 g) were used in this study. Two of them were carrying only one fetus and one had two fetuses. Anesthesia was induced with 5% isoflurane in a gas chamber and maintained with a mask delivering 1.5%–3% isoflurane. Respiration was monitored during the scan, and anesthesia protocols were followed by a veterinarian. Prior to the PET examination, intravenous access was gained through the tail vein and used for radiotracer injection. The animals were placed in the field of view in a PET-CT system (Siemens, Erlangen, Germany). ^{11}C-metformin was prepared as previously described [15], containing metformin dissolved in aqueous $(NH_4)_2HPO_4$ (100 mM, pH 5). A bolus of ^{11}C-metformin was injected (~1 min) followed by 0.5–1 mL saline at time = 0. A volume of 3.5–5 mL was injected intravenously with a mean radioactive dosage of 40 MBq (17–86 MBq; specific activity: 30–90 GBq/micromole). The animals underwent 70 min of dynamic PET/CT scan.

List-mode acquired PET data were reconstructed and divided into frames with the frame structure: 12×5 s,

5 × 10 s, 2 × 30 s, 4 × 60 s, 4 × 120 s, and 11 × 300 s. Volume of interest (VOI) was defined using PMOD (PMOD Technologies LLC, Zürich, Switzerland) in order to evaluate the tracer activity in specific areas.

2.3. Analysis of Metformin mRNA Transporters in Placenta

2.3.1. Chinchilla. Five placentae were dissected from chinchillas at gestation days 82–101. The placentae were rinsed in saline and divided into small parts, and the pieces were snap-frozen in liquid nitrogen. Samples were stored at −80°C until analysis.

2.3.2. Human. Seven placentae were collected immediately after planned cesarean sections from uncomplicated pregnancies. A paracentral grape-sized piece of villous tissue was excised, rinsed in saline, divided into smaller pea-sized pieces, and snap-frozen in liquid nitrogen. Samples were stored at −80°C until analysis.

2.3.3. qPCR Analysis. RNA was extracted using TRIzol (Gibco BRL; Life Technologies, Roskilde, Denmark). RNA was quantified using a NanoDrop 8000 spectrophotometer (Thermo Scientific, Waltham, MA). Integrity of the RNA was checked by visual inspection of the two ribosomal RNAs on an agarose gel. cDNA was synthesized using a Verso cDNA kit (Ab-1453; Thermo Scientific) with random hexamer primers. The PCR reactions were performed in duplicate using LightCycler SYBR Green master mix (Roche Applied Science, Indianapolis, IN) in a LightCycler 480 (Roche Applied Science) using the following protocol: one step at 95°C for 3 min, then 95°C for 10 s, 60°C for 20 s, and 72°C for 10 s, and finally, a melting curve analysis was performed. The increase in fluorescence was measured in real-time during the extension step. The relative gene expression was estimated using the "Advanced Relative Quantification" mode of the software version LCS 480 1.5.1.62 (Roche Applied Science), and specificity of the amplification was checked by melting temperature analysis. The following primer pairs were designed using QuantPrime [16]:

Chinchilla primers:

Housekeeping: beta-2 microglobulin, TGGTGCATG GCGCCTTTATC GACAGTGTGACGTGTGAAAC GC product length 70 bp
CH_MATE1 AAGGAGCTGTTGGAGTCAACCC TAACGATGCTGAAGCGCACAGG product length 74 bp
CH_OCT1 GCTGGGCATATAGCTCAGTGGTAG GATTGAACCAAGGGCCTTCAGC product length 62 bp
CH_OCT2 ATTCCCAGCCGCCTTCATTGTC TGA CACAGCCCAAGGATAACGG product length 70 bp
CH_OCT3 TTCAGGCCCAGACATCTGAAGG TC TGCTTGGCTCCTGGTAAAGC product length 62 bp

Human primers:

Housekeeping: beta-2 microglobulin: GAGGCTATCC AGCGTACTCC- AATGTCGGATGGATGAAACCC product length 111 bp
H.MATE1 TCGGCTTATCTTCTGCCTGT CTGGG TAAGCCTGGACACAT product length 197 bp
H.OCT1 TAATGGACCACATCGCTCAA AGCCCC TGATAGAGCACAGA product length 190 bp
H.OCT2 ATGCCCACCACCGTGGACGAT AGGA AGACGATGCCCACGTA product length 128 bp
H.OCT3 (SLC22A3) GGAGTTTCGCTCTGTTCAGG GGAATGTGGACTGCCAAGTT product length 216 bp

All primers were purchased from the same manufacturer (DNA Technology, Risskov, Denmark). A similar setup was used for negative controls, except that the reverse transcriptase was omitted, and no PCR products were detected under these conditions.

2.4. Ethical Aspects. The study followed the guidelines for use and care of laboratory animals and was approved by the Danish Inspectorate of Animal Experiments. During anesthesia, the animals were euthanized by an overdose injection of pentobarbital. For the human placentae, the mothers all gave informed consent prior to the placenta harvesting.

3. Results

3.1. PET. Visual inspection of the PET scans revealed that [^{11}C]-metformin was primarily found in the kidneys, liver and bladder, and a small amount in the submandibular glands (Figure 2). Dynamic PET with [^{11}C]-metformin showed a high signal from the liver and kidney, but there was no signal from the fetuses (Figures 3(b)–3(d)). Measurements of standardized uptake value (SUV) (Figure 4) showed that radioactive uptake in the liver increased just after [^{11}C]-metformin administration and steadily decreased from $t = 250$ s. A relatively high and prolonged uptake was observed in the kidneys. No [^{11}C]-metformin was accumulated in the fetus.

3.2. Analysis of mRNA for Metformin Transporters in Human and Chinchilla Placentas. mRNA expression of metformin transporters revealed that human placentae primarily expressed OCT3, whereas chinchillas primarily expressed OCT1 (Figure 5). The expression of other transporters was found very low.

4. Discussion

The biodistribution of [^{11}C]-metformin has previously been studied in pigs, rats, and humans, but none of them during pregnancy [15]. As the chemical production of [^{11}C]-metformin varied from time to time, and because the isotope has a short half-life of around 20 min, the animals included in this study received different volumes (3.5–5 mL) and radioactive dosages (17–86 MBq) of [^{11}C]-metformin.

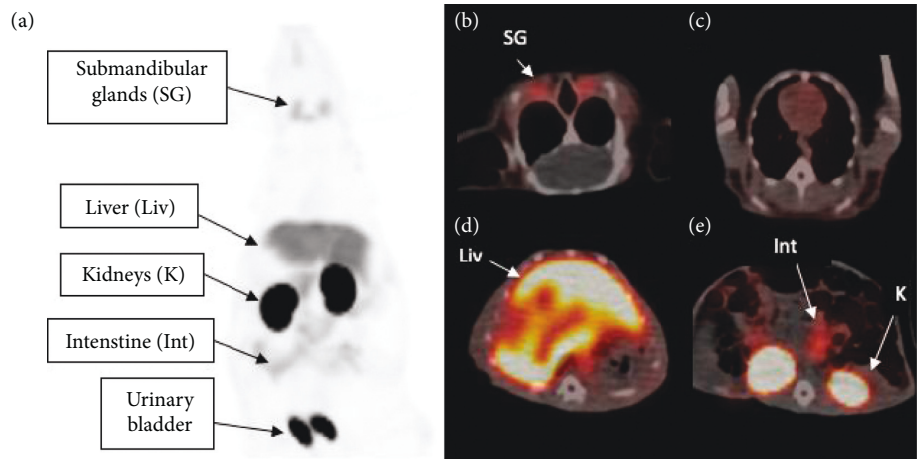

Figure 2: Whole-body [^{11}C]-metformin PET scans were performed after i.v. tracer injection. (a) Attenuation corrected maximum intensity projection of [^{11}C]-metformin biodistribution in a chinchilla 30 min after injection demonstrates uptake in submandibular glands, liver, kidneys, intestine, and urinary bladder (indicated by arrows). Transaxial slices of [^{11}C]-metformin biodistribution on merged PET/CT images (arrows indicate metformin avid organs) are displayed in (b) submandibular glands, (c) thorax, (d) liver, and (e) kidneys.

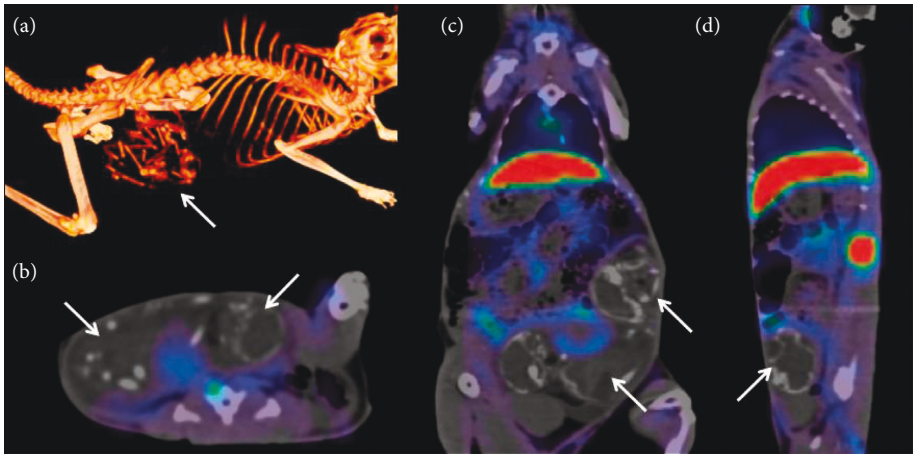

Figure 3: (a) Two fetuses identified in a pregnant chinchilla (the arrow indicates the fetuses) with 3D volume rendering of bone reconstructed CT scan. A summarized [^{11}C]-metformin PET/CT scan is visualized in transaxial (b), coronal (c), and sagittal plane (d) (arrows indicate the two fetuses), demonstrating no metformin uptake in the fetuses.

However, it was easy to follow the tracer in all PET scans with a signal-to-noise ratio sufficient for subsequent data analyses. The acquired PET images of the pregnant chinchillas revealed a maternal biodistribution of metformin that was comparable to that of nonpregnant humans [14]. The kidney curve (Figure 4) showed a high SUV variation compared to the other curves. However, an interindividual variation is also observed in humans due to both genetic variations and glomerular filtration rate [17]. The accumulation of metformin in the bladder indicated that metformin was excreted through the kidneys similar to humans (Figure 2(a)). We also found a very low SUV in the muscles which is comparable to humans. No uptake of metformin was observed in the chinchilla fetuses. Metformin is normally ingested orally but was administered intravenously in this study. However, as metformin is not metabolized in the body and is excreted uncharged, the mode of drug administration should not influence the distribution.

In humans, metformin transfers from the maternal to the fetal circulation, demonstrated by findings of metformin in umbilical cord blood samples in women taking metformin prior to birth [8]. The exact mechanism how metformin crosses the placenta in humans is not fully elucidated [18]. Nevertheless, the difference in the placental transport and pharmacokinetics of metformin between chinchilla and human suggests some limitations in the use of pregnant chinchillas as an animal model for human pregnancy. An obvious reason why metformin is not found in the chinchilla fetuses could be due to transporters in the trophoblasts. We found that human placentae express OCT3 whereas chinchillas express OCT1 (Figure 5). This difference in transporters could be the reason for the missing uptake of metformin in the chinchilla placenta and fetus. In humans, OCT1 is mainly found in hepatocytes and sometimes referred to as the "liver-specific" OCT. Some placenta studies have also found expression of OCT1 in the human placenta,

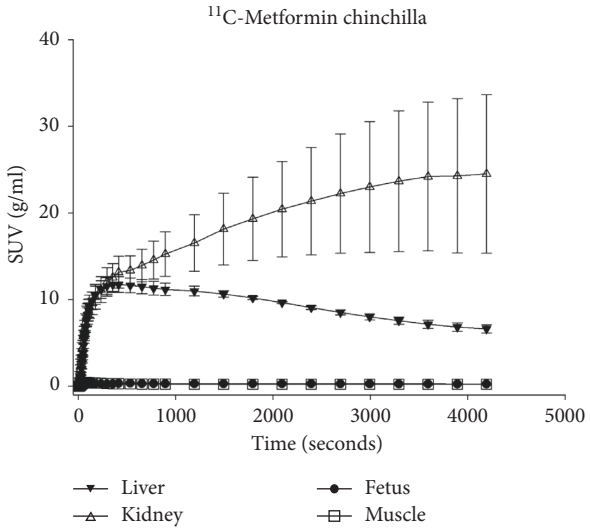

Figure 4: Dynamic PET metformin kinetics. Standardized uptake value (SUV, g/ml) of [^{11}C]-metformin in the liver, kidney, fetus, and muscle.

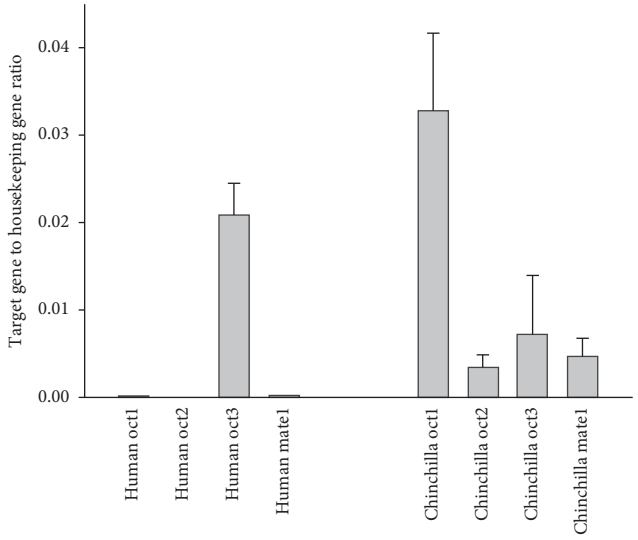

Figure 5: mRNA expression of the metformin transporters in chinchilla and human placentae related to housekeeping gene.

conflicting our findings [11]. OCT3 is the most abundantly expressed SLC transporter in the placenta in many species, including humans, rats, and mice [11], and it has been referred to as the "placenta specific" OCT. However, the tissue distribution of OCT3 is much broader and thus not specific for placenta [11]. Pregnancy is a dynamic process, and the placenta undergoes adaptations and physiological changes accordingly. In pregnant rats, the expressions of OCT3 and MATE1 change during the different stages of pregnancy [19]. Expression of MATE1 was found in human placenta from first trimester [19]. In the term human placentae, we found no expression of MATE1, confirming previous findings [11].

Although PCR is a valuable technique, PCR is capable only in showing whether mRNA is present, but it is incapable of revealing actual protein expressions. In addition, PCR is unable to identify where the transporters reside inside the trophoblasts. Functional studies in human placentae have found that OCT3 is located in the fetal facing membrane of the placenta [20]. Immunohistochemistry in rat placentae was used to identify OCT3 at the fetal side, like in human placentae, whereas MATE1 was located at the maternal side of the rat placenta [21]. In a study where a human *ex vivo* dual perfusion placenta model was used to study metformin, it was found that the fetal-to-maternal transfer of metformin was significantly higher than the maternal-to-fetal transfer [18]. In theory, metformin could be transported into the trophoblasts and quickly transported out again by efflux transporters and never reach the fetal compartment. A study in rats showed that MATE1 was responsible for the efflux of metformin from the trophoblasts [22], and as both OCT3 and MATE1 are found in the rat placentae, synchronized activity of these transporters is suggested as the transplacental pathway [21]. In mice, OCT3, but not MATE1, is found in the placentae, similar with human placentae from late pregnancy [11]. In terms of placentae metformin transporters, mice appear as a more comparable animal model for studying metformin transport in late pregnancy.

5. Conclusion

In conclusion, we found that PET and [^{11}C]-metformin administration can be used to study the biodistribution of metformin in a chinchilla animal model, and we found that the biodistribution was comparable to findings previously shown in nonpregnant humans. In chinchillas, however, [^{11}C]-metformin did not pass the placenta like in humans. Therefore, we studied the possible differences in metformin transporters between human and chinchilla placenta based on mRNA expression of these transport proteins. We interestingly found that the human placentae mainly expressed OCT3, whereas chinchilla placentae had high expression of OCT1. Based on these results, the *in vivo* pharmacokinetics and biodistribution of metformin in chinchillas do not advocate this animal model as an optimal choice for investigations of metformin in human pregnancy.

Data Availability

The PET/CT and mRNA data used to support the findings of this study are included within the article in Figures 2–5.

Conflicts of Interest

The authors declare that they have no conflicts of interest.

Acknowledgments

Per Glud Ovesen and Maria Dahl Overgaard received financial support from the Novo Nordisk Foundation.

References

[1] U. Kampmann, L. R. Madsen, G. O. Skajaa, D. S. Iversen, N. Moeller, and P. Ovesen, "Gestational diabetes: a clinical

update," *World Journal of Diabetes*, vol. 6, no. 8, pp. 1065–1072, 2015.

[2] R. Gabbay-Benziv, E. A. Reece, F. Wang, and P. Yang, "Birth defects in pregestational diabetes: defect range, glycemic threshold and pathogenesis," *World Journal of Diabetes*, vol. 6, no. 3, pp. 481–488, 2015.

[3] S. E. Inzucchi, R. M. Bergenstal, J. B. Buse et al., "Management of hyperglycemia in type 2 diabetes, 2015: a patient-centered approach: update to a position statement of the American Diabetes Association and the European Association for the study of diabetes," *Diabetes Care*, vol. 38, no. 1, pp. 140–149, 2015.

[4] B. Gottlieb and W. H. Auld, "Metformin in treatment of diabetes mellitus," *BMJ*, vol. 1, no. 5293, pp. 1692-1693, 1962.

[5] R. DeFronzo, G. A. Fleming, K. Chen, and T. A. Bicsak, "Metformin-associated lactic acidosis: current perspectives on causes and risk," *Metabolism*, vol. 65, no. 2, pp. 20–29, 2016.

[6] G. G. Graham, J. Punt, M. Arora et al., "Clinical pharmacokinetics of metformin," *Clinical Pharmacokinetics*, vol. 50, no. 2, pp. 81–98, 2011.

[7] R. S. Lindsay and M. R. Loeken, "Metformin use in pregnancy: promises and uncertainties," *Diabetologia*, vol. 60, no. 9, pp. 1612–1619, 2017.

[8] B. Charles, R. Norris, X. Xiao, and W. Hague, "Population pharmacokinetics of metformin in late pregnancy," *Therapeutic Drug Monitoring*, vol. 28, no. 1, pp. 67–72, 2006.

[9] S. Butalia, L. Gutierrez, A. Lodha, E. Aitken, A. Zakariasen, and L. Donovan, "Short- and long-term outcomes of metformin compared with insulin alone in pregnancy: a systematic review and meta-analysis," *Diabetic Medicine*, vol. 34, no. 1, pp. 27–36, 2017.

[10] L. G. E. Hanem, Ø. Salvesen, P. B. Juliusson et al., "Intrauterine metformin exposure and offspring cardiometabolic risk factors (PedMet study): a 5–10 year follow-up of the PregMet randomised controlled trial," *Lancet Child & Adolescent Health*, vol. 3, no. 3, pp. 166–174, 2019.

[11] F. Staud, L. Cerveny, and M. Ceckova, "Pharmacotherapy in pregnancy; effect of ABC and SLC transporters on drug transport across the placenta and fetal drug exposure," *Journal of Drug Targeting*, vol. 20, no. 9, pp. 736–763, 2012.

[12] E. Mikkelsen, H. Lauridsen, P. M. Nielsen et al., "The chinchilla as a novel animal model of pregnancy," *Royal Society Open Science*, vol. 4, no. 4, p. 161098, 2017.

[13] B. Clancy, R. B. Darlington, and B. L. Finlay, "Translating developmental time across mammalian species," *Neuroscience*, vol. 105, no. 1, pp. 7–17, 2001.

[14] L. C. Gormsen, E. I. Sundelin, J. B. Jensen et al., "In vivo imaging of human 11C-metformin in peripheral organs: dosimetry, biodistribution, and kinetic analyses," *Journal of Nuclear Medicine*, vol. 57, no. 12, pp. 1920–1926, 2016.

[15] S. Jakobsen, M. Busk, J. B. Jensen et al., "A PET tracer for renal organic cation transporters, 11C-metformin: radiosynthesis and preclinical proof-of-concept studies," *Journal of Nuclear Medicine*, vol. 57, no. 4, pp. 615–621, 2016.

[16] S. Arvidsson, M. Kwasniewski, D. M. Riano-Pachon, and B. Mueller-Roeber, "QuantPrime - a flexible tool for reliable high-throughput primer design for quantitative PCR," *BMC Bioinformatics*, vol. 9, no. 1, p. 465, 2008.

[17] M. V. Tzvetkov, S. V. Vormfelde, D. Balen et al., "The effects of genetic polymorphisms in the organic cation transporters OCT1, OCT2, and OCT3 on the renal clearance of metformin," *Clinical Pharmacology & Therapeutics*, vol. 86, no. 3, pp. 299–306, 2009.

[18] K. Tertti, U. Ekblad, T. Heikkinen, M. Rahi, T. Rönnemaa, and K. Laine, "The role of organic cation transporters (OCTs) in the transfer of metformin in the dually perfused human placenta," *European Journal of Pharmaceutical Sciences*, vol. 39, no. 1-3, pp. 76–81, 2010.

[19] D. Ahmadimoghaddam, L. Zemankova, P. Nachtigal et al., "Organic cation transporter 3 (OCT3/SLC22A3) and multidrug and toxin extrusion 1 (MATE1/SLC47A1) transporter in the placenta and fetal tissues: expression profile and fetus protective role at different stages of Gestation1," *Biology of Reproduction*, vol. 88, no. 3, pp. 1085–1093, 2013.

[20] R. Sata, H. Ohtani, M. Tsujimoto et al., "Functional analysis of organic cation transporter 3 expressed in human placenta," *Journal of Pharmacology and Experimental Therapeutics*, vol. 315, no. 2, pp. 888–895, 2005.

[21] D. Ahmadimoghaddam, J. Hofman, L. Zemankova et al., "Synchronized activity of organic cation transporter 3 (Oct3/Slc22a3) and multidrug and toxin extrusion 1 (Mate1/Slc47a1) transporter in transplacental passage of MPP+ in rat," *Toxicological Sciences*, vol. 128, no. 2, pp. 471–481, 2012.

[22] D. Ahmadimoghaddam and F. Staud, "Transfer of metformin across the rat placenta is mediated by organic cation transporter 3 (OCT3/SLC22A3) and multidrug and toxin extrusion 1 (MATE1/SLC47A1) protein," *Reproductive Toxicology*, vol. 39, pp. 17–22, 2013.

Hindawi
Contrast Media & Molecular Imaging
Volume 2019, Article ID 6501231, 7 pages
https://doi.org/10.1155/2019/6501231

Research Article

Cellular MRI Reveals Altered Brain Arrest of Genetically Engineered Metastatic Breast Cancer Cells

Katie M. Parkins,[1,2] Amanda M. Hamilton,[1] Veronica P. Dubois,[1,2] Suzanne M. Wong,[1] Paula J. Foster,[1,2] and John A. Ronald [1,2,3]

[1]*Robarts Research Institute, The University of Western Ontario, London, Ontario, Canada*
[2]*The Department of Medical Biophysics, The University of Western Ontario, London, Ontario, Canada*
[3]*Lawson Health Research Institute, London, Ontario, Canada*

Correspondence should be addressed to John A. Ronald; jronald@robarts.ca

Received 13 July 2018; Revised 15 November 2018; Accepted 4 December 2018; Published 8 January 2019

Guest Editor: Michael Pedersen

Purpose. The combined use of anatomical magnetic resonance imaging (MRI), cellular MRI, and bioluminescence imaging (BLI) allows for sensitive and improved monitoring of brain metastasis in preclinical cancer models. By using these complementary technologies, we can acquire measurements of viable single cell arrest in the brain after systemic administration, the clearance and/or retention of these cells thereafter, the growth into overt tumours, and quantification of tumour volume and relative cancer cell viability over time. While BLI is very useful in measuring cell viability, some considerations have been reported using cells engineered with luciferase such as increased tumour volume variation, changes in pattern of metastatic disease, and inhibition of *in vivo* tumour growth. *Procedures*. Here, we apply cellular and anatomical MRI to evaluate *in vivo* growth differences between iron oxide labeled naïve (4T1BR5) and luciferase-expressing (4T1BR5-FLuc-GFP) murine brain-seeking breast cancer cells. Balb/C mice received an intracardiac injection of 20,000 cells and were imaged with MRI on days 0 and 14. Mice that received 4T1BR5-FLuc-GFP cells were also imaged with BLI on days 0 and 14. *Results*. The number of signal voids in the brain (representing iron-labeled cancer cells) on day 0 was significantly higher in mice receiving 4T1BR5 cells compared to mice receiving 4T1BR5-FLuc-GFP cells ($p < 0.0001$). Mice that received 4T1BR5 cells also had significantly higher total brain tumour burden and number of brain metastases than mice that received 4T1BR5-FLuc-GFP cells ($p < 0.0001$). *Conclusions*. By employing highly sensitive cellular MRI tools, we demonstrate that engineered cells did not form tumours as well as their naïve counterparts, which appear to primarily be due to a reduction in cell arrest. These results indicate that engineering cancer cells with reporter genes may alter their tropism towards particular organs and highlight another important consideration for research groups that use reporter gene imaging to track metastatic cancer cell fate *in vivo*.

1. Introduction

The ability to accurately quantify tumour growth in preclinical cancer models is critical for effective study of tumour biology, metastatic spread, and treatment response. While some subcutaneous and orthotopic tumour volumes can be measured using either manual or electronic calipers, this relies on a fairly developed-palpable tumour. For instance, many murine cancer models have been developed to try to improve the clinical relevance such that micro- or macro-metastases form in the brain, bone, and lung and thus are not measurable with calipers. To better monitor the longitudinal growth of subpalpable or metastatic disease relies on one employing noninvasive imaging techniques.

There are a number of cellular and molecular imaging modalities that can be used to noninvasively measure tumour size, location, metabolism, and metastatic burden in preclinical cancer models such as ultrasound (US), computed tomography (CT), magnetic resonance imaging (MRI), single-photon emission computed tomography (SPECT), positron emission tomography (PET), and optical imaging modalities such as fluorescence imaging and bioluminescence imaging (BLI) [1–3]. Among these, BLI continues to be one of the most employed technologies for

evaluating tumour growth and viability over time due to its high sensitivity, high throughput nature, and relative cost-effectiveness. For BLI, tumour cell lines are engineered to express a luciferase reporter gene, most commonly firefly luciferase (FLuc), which produces light as a product of oxidation of a matching luciferin substrate. The relative amount of light produced at a particular location can provide indirect measures of total cancer cell viability over time [4]. This is an important consideration as larger tumours may have edema and/or necrosis, contributing to imaging measures of tumour volume, and as a result, overestimate the number of viable cancer cells present [5]. Furthermore, in models evaluating treatment response, the amount of viable tissue within the tumour may change before any anatomical changes occur. Thus, BLI can provide valuable complementary information to measures of tumour size with either calipers or anatomical imaging modalities such as MRI.

We have previously demonstrated the combined use of BLI, anatomical MRI, and cellular MRI tools for monitoring experimental breast cancer brain metastasis in mice [6]. Cellular MRI requires cancer cells to be labeled with superparamagnetic iron oxide (SPIO) nanoparticles in culture prior to transplantation into mice [7]. The iron causes a distortion in the magnetic field, leading to a loss of signal in an iron-sensitive MRI sequence. The blooming artifact produced by the SPIO is larger than the cell itself, and as a result, we can visualize single cancer cells arresting in the brain at the time of injection as well as nondividing cancer cells that retain their iron label over time [8]. A small portion of the cancer cells will divide and lose their iron label but can be visualized with conventional MRI. By using cellular MRI, anatomical MRI, and BLI simultaneously in the same animals, we can acquire measurements of viable single cell arrest and cell clearance as well as follow the growth and/or changes in viability of tumours in the brain over time [6].

While BLI is very useful in evaluating the fate of many different cell populations *in vivo*, including cancer cells, in recent years some considerations for the use of BLI have been reported. Following the engineering of cells with luciferase, several studies have noted changes in tumour volume variation across animals, altered cancer cell tropism toward particular organs, as well as differences in tumour growth rates [9–12]. The ability to sensitively track the dissemination, arrest, dormancy, or growth of single cells with cellular MRI may provide new insights into potential effects of cell engineering. The objective of this work was to use cellular and anatomical MRI to characterize the *in vivo* growth patterns of naïve and lentiviral-engineered brain-seeking triple negative breast cancer cells coexpressing fluorescent and bioluminescent reporters in the mouse brain.

2. Materials and Methods

2.1. In Vitro Studies

2.1.1. Cell Engineering. Brain-seeking mouse mammary carcinoma cells (4T1BR5) were a kind gift from Dr. Patricia Steeg's lab (NIH, Centre for Cancer Research) and engineered to stably coexpress red-shifted *Luciola italica* luciferase (FLuc) and GFP using a commercial lentiviral vector (RediFect Red-FLuc-GFP lentiviral particles; PerkinElmer, USA). Cells were transduced at a multiplicity of infection of 20 and sorted based on GFP expression using a FACSAria III flow cytometric cell sorter (BD Biosciences, San Jose, CA, USA). The resultant 4T1BR5-FLuc-GFP cells were maintained in DMEM containing 10% FBS at 37°C and 5% CO_2. All *in vitro* experiments were performed in triplicate.

2.1.2. Iron Labeling. For iron labeling, 2×10^6 cells were plated in a 75 cm^3 flask, supplemented with DMEM containing 10% FBS, and allowed to adhere for 24 hours. Cells were incubated for an additional 24 hours with 10 mL media containing 25 μg/mL of MPIO beads (0.9 μm in diameter, 63% magnetite, labeled with Flash Red; Bangs Laboratory, Fishers, IN, USA). Cells were washed three times with Hanks balanced salt solution (HBSS) and then trypsinized with 0.25% Trypsin-EDTA. The cells were then collected and thoroughly washed three more times with HBSS to remove unincorporated MPIO before cell injection and *in vitro* evaluation.

2.1.3. Propidium Iodide Cell Cycle Assay. Breast cancer cells (naïve and engineered 4T1BR5) were cultured as stated above. Cells were centrifuged at 1000 rpm for 5 minutes. Cell pellets were then fixed with 500 μl of 70% ethanol for 30 minutes in 4°C, washed twice with phosphate-buffered saline (PBS), and centrifuged at 850 g. Cells were then treated with 50 μL of RNase (100 μg/mL). The mixture was kept in a water bath at 37°C for 30 minutes prior to staining with 200 μL of propidium iodide solution (50 μg/mL) and then analyzed by flow cytometry using a FACSAria III flow cytometric cell sorter (BD Biosciences, San Jose, CA, USA).

2.1.4. Proliferation Assay. Vybrant MTT (3-(4,5-dimethylthiazolyl-2)-2,5-diphenyltetrazolium bromide) proliferation assays were used to evaluate whether genetic engineering had an effect on *in vitro* proliferation. 4T1BR5 and 4T1BR5-FLuc-GFP cells were seeded in 96-well plates (2.0×10^3 cells per well) with 0.25 mL of media, and cell proliferation was evaluated at 0, 24, 48, and 96 hours. MTT solution (20 μL) was added to each well, and absorbance at 450 nm was measured using a microplate spectrophotometer (Fluoroskan Ascent FL, ThermoLabSystems).

2.1.5. Clonogenic Assay. Naïve and engineered 4T1BR5 cells were seeded in 6-well plates (1.0×10^3 cells per well) with 2 mL of media. The number of colonies in each well was manually counted using a hemocytometer at 72 hours after plating.

2.2. In Vivo Studies

2.2.1. Experimental Breast Cancer Brain Metastasis Model. Animals were cared for in accordance with the standards of the Canadian Council on Animal Care and under an

approved protocol of the University of Western Ontario's Council on Animal Care (protocol number: 2014-026). To deliver MPIO-labeled 4T1BR5 or 4T1BR5-FLuc-GFP cells into the brain, 2.0×10^4 cells were injected into the left ventricle of female BALB/c mice ($n = 16$; 6–7 weeks old; Charles River Laboratories, Wilmington, MA, USA). Cells were suspended in 0.1 mL of HBSS, and image-guided injections into the left ventricle were performed using a Vevo 2100 ultrasound system (FUJIFILM VisualSonics Inc., Toronto, ON, Canada). MRI was performed on all sixteen mice on days 0 and 14 after intracardiac injection. In addition, mice that received 4T1BR5-FLuc-GFP cells had BLI performed on days 0 and 14 after intracardiac injection.

2.2.2. MRI. All MRI scans were performed on a 3T GE clinical MR scanner (General Electric) using a custom-built gradient coil and a custom-built solenoidal mouse brain radiofrequency coil [7, 13]. Mice were anesthetized with isoflurane (2% in 100% oxygen), and images were obtained using a 3D balanced steady-state free precession (bSSFP) imaging sequence (Fast Imaging Employing Steady-State Acquisition (FIESTA) on the GE system) which has been previously optimized for iron detection [14]. The scan parameters for day 0 images were repetition time (TR) = 8 ms, echo time (TE) = 4 ms, bandwidth (BW) = 41.7 kHz, flip angle (FA) = 35 degrees, averages (NEX) = 2, phase cycles = 4, and matrix = 150×150. Total scan time was 15 minutes per mouse. For day 14 images, a longer scan time was required for tumour detection, and so imaging parameters were TR = 10 ms, TE = 5 ms, BW = 12.5 kHz, FA = 35 degrees, NEX = 2, phase cycles = 8, and matrix = 150×150. Total scan time was 35 minutes per mouse.

2.2.3. BLI. BLI was performed using a hybrid optical/X-ray scanner (IVIS Lumina XRMS In Vivo Imaging System, PerkinElmer). Mice were anesthetized with isofluorane (2% in 100% oxygen) and received a 150 μL intraperitoneal injection of D-luciferin (30 mg/mL; Syd Labs, Inc., MA, USA), and BLI images were captured for up to 35 minutes after injection.

2.2.4. Image Analysis. MRI images were analyzed using OsiriX software (Pixmeo, SARL, Bernex, Switzerland). Day 0 images were analyzed by manually counting signal voids (representing iron-labeled cells) in every slice throughout the whole brain. For day 14 images, brain metastases were manually traced and 3D tumour volumes were reconstructed using the OsiriX volume algorithm. *In vitro* BLI signal was measured with region-of-interest (ROI) analysis using Living Image Software (PerkinElmer). An ROI was drawn around each well, and average radiance (photons/second/cm^2/steradian) was measured.

2.2.5. Histology. At endpoint, mice were sacrificed by pentobarbital overdose and perfusion fixed with 4% paraformaldehyde. Mouse brains were removed and cryopreserved in ascending concentrations of sucrose (10, 20, and 30% w/v) in distilled water for at least 1 hour each. Brains were immersed in the optimal cutting temperature (OCT) compound, oriented in a sectioning plane parallel to that of MRI, and frozen using liquid nitrogen. Frozen sections (10 μm) were collected and stained using hematoxylin and eosin (H&E) to visualize tumour morphology.

2.2.6. Statistics. A power analysis was performed using $G*$Power software to determine the appropriate sample size for this study. All statistics were calculated using GraphPad Prism 4. A Student's two-tailed unpaired t-test was used to compare conditions in *in vitro* experiments as well as between animal groups. A nominal p value less than 0.05 was considered statistically significant.

3. Results

After lentiviral transduction, 4.3% of the total population was found to be GFP positive, and these cells were sorted, expanded, and then sorted a second time (Figure 1(a)). During the second sort, we found 86.6% of the cells to be GFP positive. From this population, we isolated the brightest GFP cells (8.2%) by FACS and expanded them in culture to obtain a population of 4T1BR5-FLuc-GFP cells that were near 100% GFP positive (Figure 1(b)). *In vitro* GFP expression was assessed using fluorescence microscopy (Figure 1(c)) and FLuc with BLI (Supplementary Figure 1(a)). To determine the stability of our reporter genes, we performed *in vitro* BLI of 4T1BR5-FLuc-GFP cells and found no significant differences in luciferase activity over multiple passages in culture (Figure 1(d)). Similarly, using FACS, we found no significant differences in mean GFP signal intensity over 10 cell passages (Supplementary Figure 1(c)). Next, we determined whether cell cycle differences existed between naïve and engineered cells by performing a propidium iodide cell cycle arrest assay. As displayed in Figure 1(f), we observed a decrease in the number of cells in the S phase and an increase in the number of cells in G_0/G_1 for engineered 4T1BR5 cells compared to naïve cells (Figure 1(e)). We evaluated differences in cellular proliferation between naïve 4T1BR5 and 4T1BR5-FLuc-GFP cells over a four-day period using an MTT assay and found there were no significant differences in cell growth at any of the time points (Figure 1(g)). We also performed a clonogenic assay to evaluate differences in the ability of each cell population to form colonies and found there was no significant difference in the number of colonies formed between naïve and engineered 4T1BR5 cells (Supplementary Figure 1(b)).

MRI and BLI data from the day of intracardiac injection (day 0) are shown in Figure 2. Perl's Prussian blue stain was performed to show both 4T1BR5 and 4T1BR5-FLuc-GFP cells were efficiently (>90%) labeled with MPIO prior to intracardiac injection (Figure 2(a)). Iron-labeled cells were visualized in MR images as discrete signal voids distributed throughout the mouse brain (Figure 2(b)). BLI signal was detected in the brain and body of mice that received 4T1BR5-FLuc-GFP cells on day 0 (Figure 2(c)). Importantly, the number of discrete signal voids in the brain on day 0 was significantly higher in mice that received 4T1BR5 cells

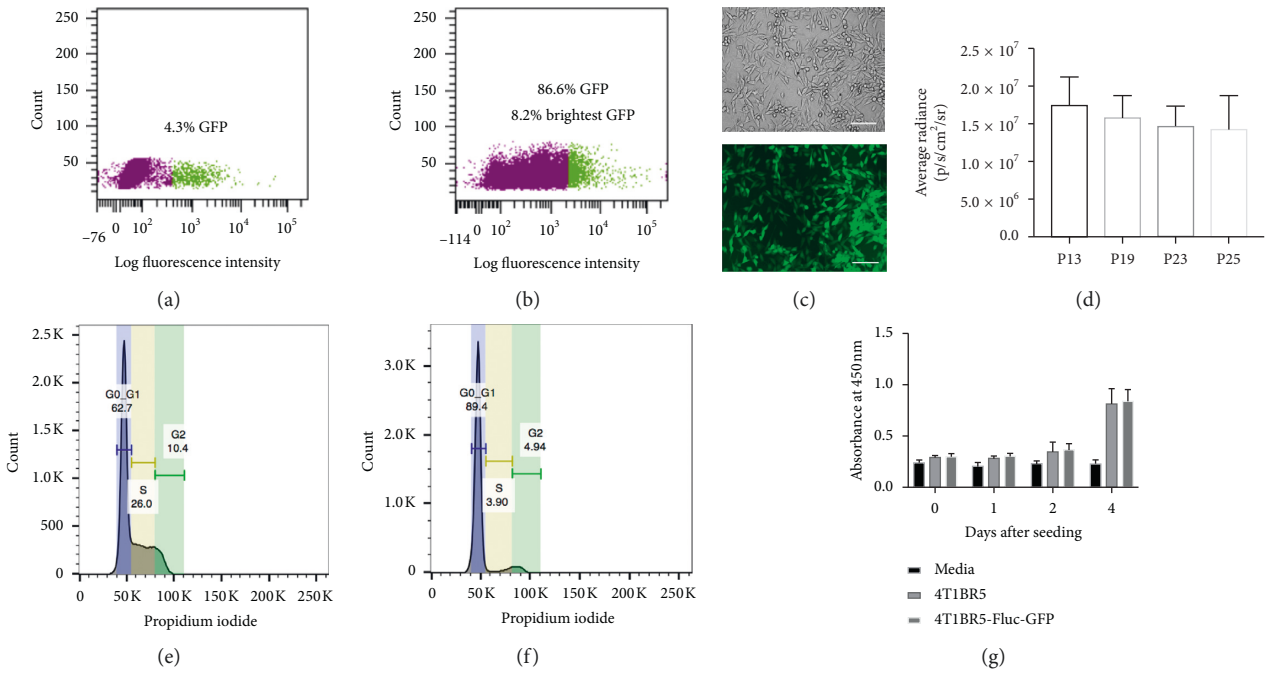

FIGURE 1: In vitro characterization of engineered 4T1BR5 cell line: after lentiviral transduction, 4.3% of the total population was GFP positive (purple = GFP negative; green = GFP positive) (sort 1) (a). These cells were grown out and found to be 86.6% GFP positive during the second sort. From this population, we sorted out the brightest 8.2% of cells (purple = cells not collected; green = 8.2% brightest GFP expression that were collected) (sort 2) (b). Brightfield and GFP expression of resultant 4T1BR5-Fluc-GFP cells (scale bar = 100 microns) (c). Luciferase activity of 4T1BR5-Fluc-GFP cells over multiple passages (P13–P25) in culture (d). Cell cycle arrest analysis of 4T1BR5 (e) and 4T1BR5-Fluc-GFP cells (f). Cellular proliferation of naïve 4T1BR5 and 4T1BR5-FLuc-GFP cells (g). Data are presented as mean ± SEM.

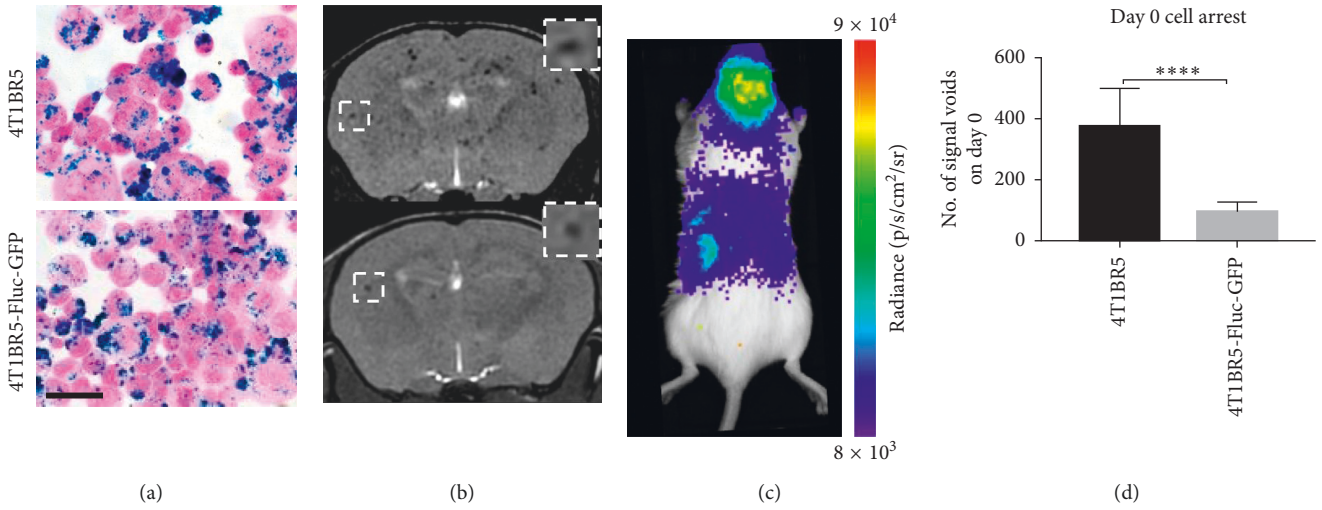

FIGURE 2: Altered initial brain arrest of engineered 4T1BR5 cells as detected with iron oxide cellular MRI: Perl's Prussian blue staining identifies iron-labeled cells in blue (scale bar = 50 microns) (a). Iron-labeled cells were visualized in brain MR images as discrete signal voids on day 0 ($n = 8$ per group); insets showing example of distinct voids (b). Brain and body BLI signal was also detectable on day 0 in mice that received luciferase-expressing cells ($n = 8$) (c). The number of voids (in MR images) on day 0 in mice receiving naïve 4T1BR5 cells or 4T1BR5-Fluc-GFP cells (d). The data are presented as mean ± SEM.

(379 ± 42 voids) than 4T1BR5-FLuc-GFP cells (98 ± 10 voids; $p < 0.0001$), despite mice receiving equivalent numbers of cells intracardially (Figure 2(d)).

On day 14, brain metastases appeared as hyperintense regions in MR images. Figure 3(a) shows an MR slice from a representative mouse brain from each group with white arrowheads pointing to metastases. All mice in this study, regardless of the cell line injected (naïve or engineered), had MR detectable metastases at endpoint. Figure 3(b) shows a whole body BLI image from a mouse with 4T1BR5-FLuc-GFP tumours. All mice that received 4T1BR5-FLuc-GFP cells had BLI detectable metastases in both the brain and

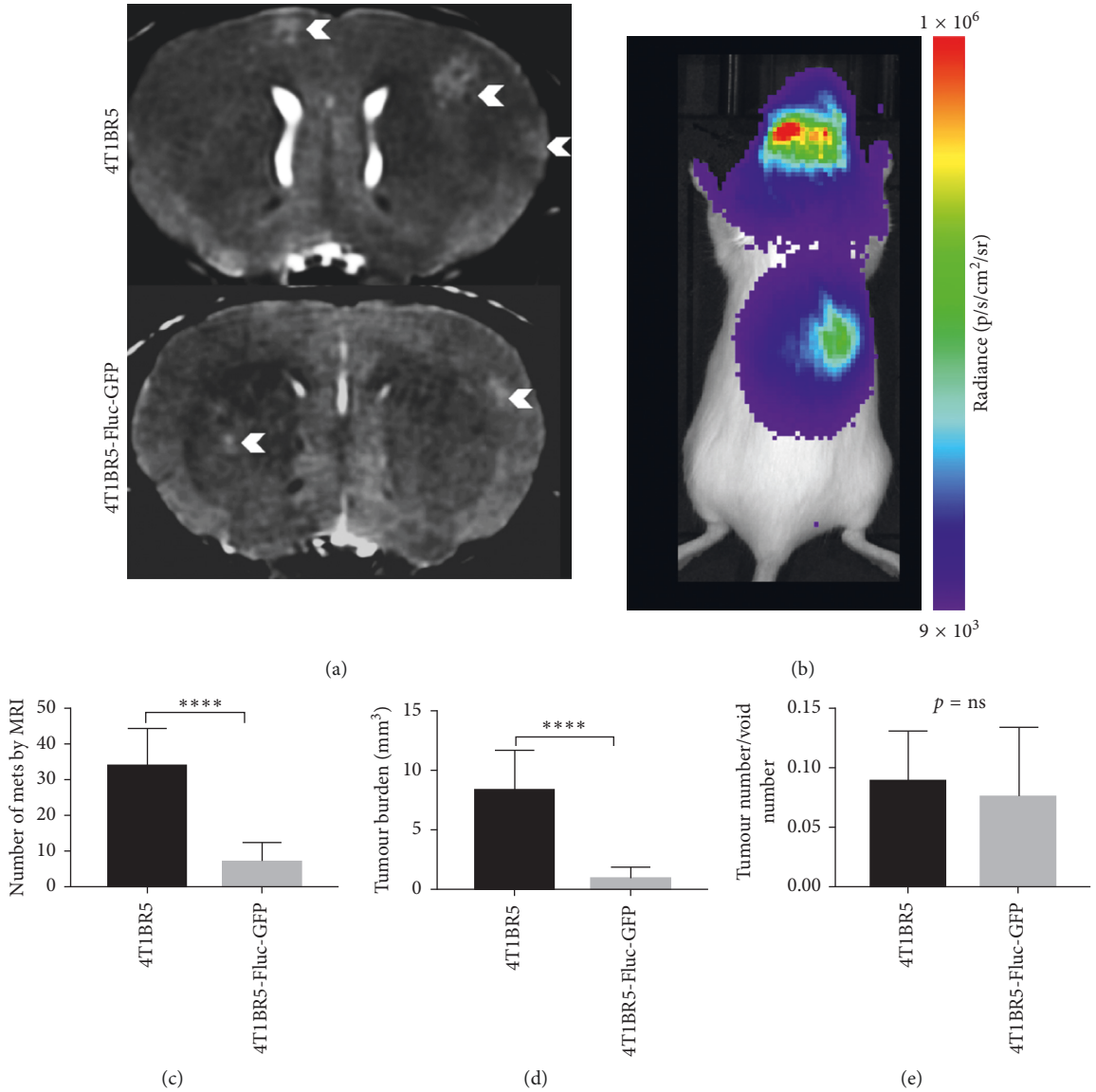

Figure 3: Differences in endpoint metastatic burden between naïve and engineered 4T1BR5 cells: representative MR slices from each group, and brain metastases indicated by white arrowheads ($n = 8$ per group) (a). BLI signal was detected in the brain and body of mice that received luciferase-expressing cells ($n = 8$) (b). The number of brain metastases (c) and total brain tumour burden (d) in mice that received naïve and luciferase-expressing 4T1BR5 cells. The ratio of the number of tumours at endpoint over the number of signal voids on day 0 was also compared between groups (e). The data are presented as mean ± SEM.

other parts of the body. In day 14 MR images, tumours were manually counted throughout the entire mouse brain. In addition, tumour boundaries were manually traced, and 3D tumour volumes were determined using the OsiriX volume algorithm. MR image analysis revealed that mice that received 4T1BR5 cells had a significantly higher number of brain metastases (34 ± 4 tumours) than mice that received 4T1BR5-FLuc-GFP cells (7 ± 2 tumours; $p < 0.0001$) (Figure 3(c)). We also found that mice that received 4T1BR5 cells had significantly more total brain tumour volume (8.27 ± 1.15 mm^3) than mice who received the 4T1BR5-FLuc-GFP cells (1.03 ± 0.28 mm^3; $p < 0.0001$) (Figure 3(d)). We also evaluated whether the relative number of tumours that formed between the groups was related to the initial number of cells seeding the brain. To do so, we evaluated the ratio of the tumour number at endpoint to the initial number of voids on day 0 and found there were no significant differences between the two mouse cohorts (Figure 3(e)). Finally, the presence of tumours was also confirmed using hematoxylin and eosin (H&E) staining. Qualitatively, mice that received 4T1BR5 cells had more metastases in the brain compared to mice with 4T1B3R5-FLuc-GFP tumours (Figure 4).

4. Discussion

In this study, we used anatomical and cellular MRI to characterize *in vivo* arrest of single cancer cells and growth differences in an established preclinical model of brain

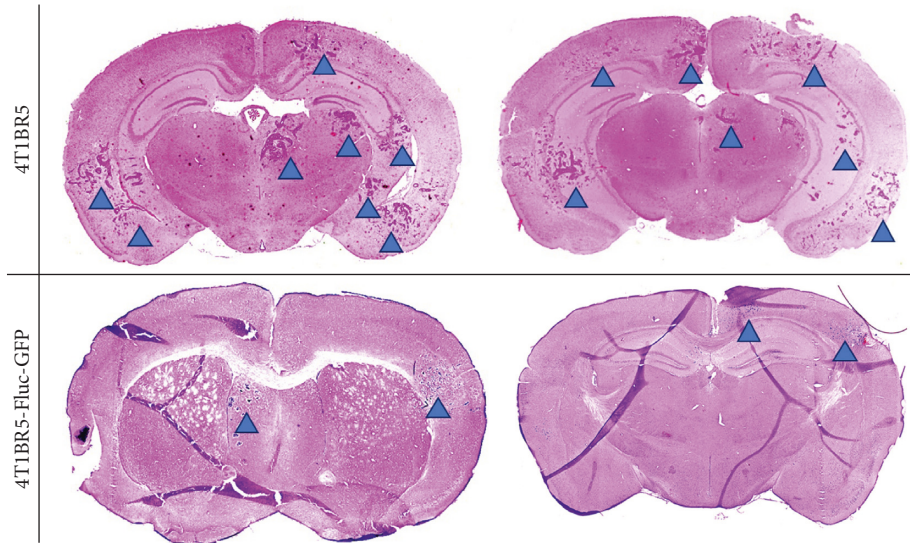

Figure 4: Histological differences in tumour burden between naïve and engineered 4T1BR5 cells: the presence of tumours was confirmed using hematoxylin and eosin (H&E) staining. Tumours are indicated with blue arrowheads.

metastasis between naïve triple negative breast cancer cells and cells engineered to stably express fluorescence and bioluminescence reporter genes. Here, we report mice that received naïve 4T1BR5 cells had significantly more brain metastases and significantly higher total brain tumour burden than mice that received engineered 4T1BR5-FLuc-GFP cells. Furthermore, through the use of iron-based cellular MRI, we were able to determine that mice that received the naïve cell line also had significantly more discrete signal voids (representing iron-labeled cells) in the brain on the day of intracardiac injection compared to mice that received our engineered cell line. This highlights that differences in metastatic tumour burden between engineered and naïve cells may not only be due to differences in *in vivo* growth rates of engineered cells as suggested by others [9–12] but may also arise very early in the metastatic process by altering organ seeding efficiency.

An important step in the metastatic cascade is the initial arrest of circulating tumour cells. Our results point to decreased arrest of engineered cancer cells being the probable explanation for differences in endpoint tumour number and burden. In the current study, we found the engineering of the 4T1BR5 cell line caused an increase in the number of cells in G_0/G_1 *in vitro*. Altered cell arrest could be the result of several possibilities including selection of a subset of cells with reduced arrest ability, the use of lentiviral vectors that integrate into the genome causing altered expression of genes important for homing and arrest, or an early immune response to a specific transgene (e.g., GFP or luciferase). Baklaushev et al. suggested an early immune response to luciferase may limit the spread of metastatic cells when they migrate as single cells in the vasculature. Since immune competent mouse models and reporter gene imaging are likewise invaluable tools for studying cancer progression, scientists should start to consider novel ways around these adverse effects (e.g., the use or development of less immunogenic reporters). If growth differences are primarily attributable to cell arrest and this is being caused by luciferase or GFP expression, one potential way to mitigate this would be the use of inducible promoters whereby the reporters are not turned on until after the cells have arrested normally.

Alternatively, our initial transduction efficiency was quite low in this study, and potential clonal dominance needs to be considered. Previous work has shown that the bulk of a solid cancer mass is derived from a single cell rather than a variety of cells that proliferate at a similar rate to produce a heterogeneous tumour [15]. By selecting a relatively small subset of cells during the engineering process, it is possible that the resultant cell line was less brain trophic or less aggressive/metastatic than the initial cell line leading to significantly less brain tumour burden in these animals. Furthermore, our naïve 4T1BR5 cell line was truly "naïve," and thus, we were unable to mock sort and expand them based on reporter gene expression as we did with our engineered cell line. Those using engineered cell lines for reporter gene imaging should provide a thorough explanation of how the cells were engineered to express those reporters. The vector used the selection process, and the purity of the cells will all provide information on how well the resultant cell line represents the initial population.

Previous studies have shown the types of genetic manipulations or variations in culture conditions that are necessary for reporter gene imaging have the potential to alter the cell's behavior both *in vitro* and *in vivo* [12]. Numerous groups have also shown engineered cells can have a similar growth rate to naïve cells *in vitro* but report a significantly slower growth rate *in vivo* compared to naïve cells [9, 12, 16], and that these differences can be related to the expression of a specific reporter. In a study by Tiffen et al., B16-F10 tumours expressing GFP-P2A-luc (luciferase) grew significantly slower than tumours formed expressing GFP only. Similarly, previous work has shown a link between the amount of reporter expression in the engineered cells and the magnitude of effect on growth. Brutkiewicz et al. found that a high level of luciferase expression can severely inhibit *in vivo* tumour growth while a low level of expression showed similar tumour growth to naïve

cells [10]. However, vying for a lower level of reporter expression would limit the detectability of the cancer cells *in vivo*, which would be of great value in studies evaluating small numbers of cells arresting in downstream organs or those evaluating micrometastasis development. In contrast, other groups have found no significant differences in *in vivo* tumour growth following luciferase engineering [11, 12]. Previous work has also shown engineering cells to express luciferase can lead to increased survival of animals compared to animals receiving an injection of naïve cells, suggesting luciferase expression may render cells less aggressive/metastatic [9]. Many of these studies have attributed differences to the expression of luciferase itself and disregarded other variables in the engineering process that may affect *in vivo* growth such as how many cells from the initial population were engineered to avoid selecting a subpopulation with altered tropism or potential effects on where the reporter genes are integrated which may affect gene expression or other confounding variables.

5. Conclusions

In summary, this study describes the application of cellular and molecular imaging tools to characterize *in vivo* growth differences between naïve and engineered cell lines in a well-established mouse model of experimental breast cancer brain metastasis. By employing cellular MRI, we have demonstrated for the first time that cell engineering can have a significant effect on cell arrest in the brain. This indicates engineering cancer cells with reporter genes may alter their tropism towards particular organs, and care should be taken when engineering cells for reporter gene imaging of cancerous, and possibly noncancerous, cell populations.

Data Availability

The data used to support the findings of this study are included within the article.

Conflicts of Interest

The authors declare that they have no conflicts of interest.

Acknowledgments

This study was supported by the Canadian Cancer Society (P.J. Foster), the Natural Sciences and Engineering Research Council of Canada (J.A. Ronald), and the Breast Cancer Society of Canada (K.M. Parkins).

Supplementary Materials

Supplementary Figure 1. In vitro characterization of cell line: bioluminescence imaging was performed to assess the functionality of the firefly luciferase gene in engineered 4T1BR5 cells (a). A clonogenic assay was performed to determine differences in the ability of each cell line to form colonies (b). Flow cytometry was used to determine differences in mean GFP fluorescence intensity over multiple passages (c). (*Supplementary Materials*)

References

[1] S. S. Gambhir, "Molecular imaging of cancer with positron emission tomography," *Nature Reviews Cancer*, vol. 2, no. 9, pp. 683–693, 2002.

[2] P. R. Contag, "Whole-animal cellular and molecular imaging to accelerate drug development," *Drug Discovery Today*, vol. 7, no. 10, pp. 555–562, 2002.

[3] R. Weissleder, "Scaling down imaging: molecular mapping of cancer in mice," *Nature Reviews Cancer*, vol. 2, no. 1, pp. 11–18, 2002.

[4] J. A. Prescher and C. H. Contag, "Guided by the light: visualizing biomolecular processes in living animals with bioluminescence," *Current Opinion in Chemical Biology*, vol. 14, no. 1, pp. 80–89, 2010.

[5] T. N. T. Le, H. Lim, A. M. Hamilton et al., "Characterization of an orthotopic rat model of glioblastoma using multiparametric magnetic resonance imaging and bioluminescence imaging," *Tomography*, vol. 4, no. 2, pp. 55–65, 2018.

[6] K. M. Parkins, A. M. Hamilton, A. V. Makela, Y. Chen, P. J. Foster, and J. A. Ronald, "A multimodality imaging model to track viable breast cancer cells from single arrest to metastasis in the mouse brain," *Scientific Reports*, vol. 6, no. 1, article 35889, 2016.

[7] C. Heyn, C. V. Bowen, B. K. Rutt, and P. J. Foster, "Detection threshold of single SPIO-labeled cells with FIESTA," *Magnetic Resonance in Medicine*, vol. 53, no. 2, pp. 312–320, 2005.

[8] E. M. Shapiro, S. Skrtic, K. Sharer, J. M. Hill, C. E. Dunbar, and A. P. Koretsky, "MRI detection of single particles for cellular imaging," *Proceedings of the National Academy of Sciences*, vol. 101, no. 30, pp. 10901–10906, 2004.

[9] C. C. Milsom, C. R. Lee, C. Hackl, S. Man, and R. S. Kerbel, "Differential post-surgical metastasis and survival in SCID, NOD-SCID and NOD-SCID-IL-2rγ^{null} mice with parental and subline variants of human breast cancer: implications for host defense mechanisms regulating metastasis," *PLoS ONE*, vol. 8, no. 8, Article ID e71270, 2013.

[10] J. C. Tiffen, C. G. Bailey, C. Ng, J. E. Rasko, and J. Holst, "Luciferase expression and bioluminescence does not affect tumor cell growth in vitro or in vivo," *Molecular Cancer*, vol. 9, no. 1, p. 299, 2010.

[11] A. J. Clark, M. Safaee, T. Oh et al., "Stable luciferase expression does not alter immunologic or in vivo growth properties of GL261 murine glioma cells," *Journal of Translational Medicine*, vol. 12, no. 1, p. 345, 2014.

[12] S. Brutkiewicz, M. Mendonca, K. Stantz et al., "The expression level of luciferase within tumour cells can alter tumour growth uponin vivo bioluminescence imaging," *Luminescence*, vol. 22, no. 3, pp. 221–228, 2007.

[13] C. Heyn, J. A. Ronald, S. S. Ramadan et al., "In vivo MRI of cancer cell fate at the single-cell level in a mouse model of breast cancer metastasis to the brain," *Magnetic Resonance in Medicine*, vol. 56, no. 5, pp. 1001–1010, 2006.

[14] E. J. Ribot, F. M. Martinez-Santiesteban, C. Simedrea et al., "In vivo single scan detection of both iron-labeled cells and breast cancer metastases in the mouse brain using balanced steady-state free precession imaging at 1.5 T," *Journal of Magnetic Resonance Imaging*, vol. 34, no. 1, pp. 231–238, 2011.

[15] P. Nowell, "The clonal evolution of tumor cell populations," *Science*, vol. 194, no. 4260, pp. 23–28, 1976.

[16] V. P. Baklaushev, A. Kilpeläinen, S. Petkov et al., "Luciferase expression allows bioluminescence imaging but imposes limitations on the orthotopic mouse (4T1) model of breast cancer," *Scientific Reports*, vol. 7, no. 1, p. 7715, 2017.

Hindawi
Contrast Media & Molecular Imaging
Volume 2019, Article ID 6438196, 7 pages
https://doi.org/10.1155/2019/6438196

Research Article

In Vivo Biokinetics of ^{177}Lu-OPS201 in Mice and Pigs as a Model for Predicting Human Dosimetry

Seval Beykan,[1] **Melpomeni Fani**,[2] **Svend Borup Jensen**,[3,4] **Guillaume Nicolas**,[5] **Damian Wild**,[5] **Jens Kaufmann**,[6] **and Michael Lassmann**[1]

[1]*Department of Nuclear Medicine, University of Würzburg, Würzburg, Germany*
[2]*Division of Radiopharmaceutical Chemistry, University Hospital Basel, Basel, Switzerland*
[3]*Department of Nuclear Medicine, Aalborg University Hospital, Aalborg, Denmark*
[4]*Department of Chemistry and Bioscience, Aalborg University, Aalborg, Denmark*
[5]*Division of Nuclear Medicine, University Hospital Basel, Basel, Switzerland*
[6]*Octreopharm Science GmbH, Ipsen Group, Berlin, Germany*

Correspondence should be addressed to Seval Beykan; beykan_s@ukw.de

Received 19 September 2018; Revised 25 October 2018; Accepted 21 November 2018; Published 3 January 2019

Academic Editor: Giancarlo Pascali

Introduction. ^{177}Lu-OPS201 is a high-affinity somatostatin receptor subtype 2 antagonist for PRRT in patients with neuroendocrine tumors. The aim is to find the optimal scaling for dosimetry and to compare the biokinetics of ^{177}Lu-OPS201 in animals and humans. *Methods*. Data on biokinetics of ^{177}Lu-OPS201 were analyzed in athymic nude *Foxn1*^{nu} mice (28 F, weight: 26 ± 1 g), Danish Landrace pigs (3 F-1 M, weight: 28 ± 2 kg), and patients (3 F-1 M, weight: 61 ± 17 kg) with administered activities of 0.19–0.27 MBq (mice), 97–113 MBq (pigs), and 850–1086 MBq (patients). After euthanizing mice (up to 168 h), the organ-specific activity contents (including blood) were measured. Multiple planar and SPECT/CT scans were performed until 250 h (pigs) and 72 h (patients) to quantify the uptake in the kidneys and liver. Blood samples were taken up to 23 h (patients) and 300 h (pigs). In pigs and patients, kidney protection was applied. Time-dependent uptake data sets were created for each species and organ/tissue. Biexponential fits were applied to compare the biokinetics in the kidneys, liver, and blood of each species. The time-integrated activity coefficients (TIACs) were calculated by using NUKFIT. To determine the optimal scaling, several methods (relative mass scaling, time scaling, combined mass and time scaling, and allometric scaling) were compared. *Results*. A fast blood clearance of the compound was observed in the first phase (<56 h) for all species. In comparison with patients, pigs showed higher liver retention. Based on the direct comparison of the TIACs, an underestimation in mice (liver and kidneys) and an overestimation in pigs' kidneys compared to the patient data (kidney TIAC: mice = 1.4 h, pigs = 7.7 h, and patients = 5.8 h; liver TIAC: mice = 0.7 h, pigs = 4.1 h, and patients = 5.3 h) were observed. Most similar TIACs were obtained by applying time scaling (mice) and combined scaling (pigs) (kidney TIAC: mice = 3.9 h, pigs = 4.8 h, and patients = 5.8 h; liver TIAC: mice = 0.9 h, pigs = 4.7 h, and patients = 5.3 h). *Conclusion*. If the organ mass ratios between the species are high, the combined mass and time scaling method is optimal to minimize the interspecies differences. The analysis of the fit functions and the TIACs shows that pigs are better mimicking human biokinetics.

1. Introduction

Recently, the radiolabeled somatostatin receptor subtype 2 (SST2) agonists DOTA-[Tyr3]octreotate (DOTATATE), DOTA-[Tyr3]octreotide (DOTATOC), and DOTA-[NaI3] octreotide (DOTANOC), as well as the antagonists OPS201 (DOTA-JR11) and OPS202 (NODAGA-JR11), have been used for imaging and treatment of neuroendocrine tumors (NETs) which are overexpressing the somatostatin receptor SST2 [1–5].

Previous preclinical and clinical studies have indicated that radiolabeled SST2 antagonists are superior to the corresponding agonists especially for tumor targeting despite little to no internalization in tumor cells [1, 3, 5–7].

A possible explanation for this observation is that the antagonistic peptides are independent of the somatostatin receptor activation state (G-protein phosphorylation); therefore, they utilize more binding sites on the tumor cell surface, have a lower dissociation rate, and also have longer tumor retention than agonistic peptides [8]. It was also shown that the uptake in the tumor is higher for SST2 antagonists compared to SST2 agonists [1, 3–5, 8]. The absorbed dose to the kidneys, the main organ at risk after treatment of NETs with DOTA labeled compounds [9], was around 50% higher for the antagonist as compared to the agonist ^{177}Lu-octreotate [5].

Rodents are the most frequently used species in preclinical studies. However, larger animals such as pigs or dogs are expected to mimic humans' physiology better than rodents [2]. In addition, these larger animals can be scanned several times with a human SPECT/CT under the same conditions as patients. Therefore, these studies have the advantage of long follow-up times and showed that multiple blood samples can be taken for dosimetry and metabolism assessment similar to patient studies.

Until today, there is one clinical human study (by Wild et al. [5]), two preclinical mouse model studies (by Dalm et al. [7] and by Nicolas et al. [3]), and one preclinical pig study (by Beykan et al. [2]) with ^{177}Lu-DOTA-JR11 (OPS201) focusing on biodistribution and dosimetry [2, 3, 5, 7]. In all of these studies, the main focus was on biodistribution and dosimetry. In the clinical study [5], the dosimetry of four patients with advanced NET was analyzed and compared to ^{177}Lu-DOTATATE. In the preclinical study by Dalm et al. [7], tumor-xenografted mice were used to determine the optimal dosage for therapy, and the therapeutic effect of ^{177}Lu-OPS201 (^{177}Lu-DOTA-JR11) was compared to the effect of ^{177}Lu-DOTA-octreotate. The follow-up period of the experiments was short (4 time points up to 7 d after injection) for a quantification of the biodistribution and dosimetry. In another preclinical study on mice by Nicolas et al. [3], OPS201 labeled with ^{177}Lu, ^{90}Y, and ^{111}In was compared with the ^{177}Lu-DOTATATE. Neither time-integrated activity coefficient (TIAC) values nor absorbed dose values were published; only the relative administered activity values per gram were reported. The focus of the preclinical pig study by Beykan et al. [2] was on in vivo biodistribution and dosimetry in pigs. Five pigs (four with coadministered amino acids and one without kidney protection) were analyzed; TIAC, absorbed dose, and effective dose coefficients values were reported.

For dose calculations, none of the preclinical studies accommodated methods for considering the differences in physiology between animals and humans. For this purpose, extrapolation methods are used that are based on mathematical equations in order to predict TIACs and consequently absorbed doses in humans by using data collected from animals. Mostly, these techniques are needed for predicting the absorbed doses for a first application of a radiopharmaceutical in humans [10]. As of today, there is no systematic study that analyzes the difference in biokinetics of radiopharmaceuticals dedicated to therapy between animal models and patients. In total, there are five published interspecies extrapolation methods related to the use of radionuclides [10, 11] in preclinical studies. However, there are no studies related to either comparing extrapolation methods or optimizing a scaling method.

Therefore, the aim of this work is to compare the in vivo biokinetics of ^{177}Lu-OPS201 in two animal models (mice and pigs) and in patients for the liver, kidneys, and blood. In addition, all published extrapolation methods related to the use of radionuclides ("scaling methods") were examined to find the optimal method for analyzing biokinetics and dosimetry.

2. Methods

OPS201 was synthesized and ^{177}Lu-OPS201 was prepared for mice as described in the study by Nicolas et al. (for mice [3]), by Beykan et al. (for pigs [2]), and by Wild et al. (for humans [5]).

For analyzing the biokinetics of ^{177}Lu-labeled peptides in preclinical and clinical studies, the data of ^{177}Lu-OPS201 athymic nude Foxn1nu mice (28 females, weight: 26 ± 1 g, age: 8–9 weeks) [3], Danish Landrace pigs (3 females-1 male, weight: 28 ± 2 kg, age: 3 months) [2], and patients (3 females-1 male, weight: 61 ± 17 kg, age: 44–77 years) [5] with administered activities of 0.19–0.27 MBq (mice, 0.017 μg of peptide), 97–113 MBq (pigs, 9 μg of peptide), and 850–1086 MBq (patients, 55–106 μg of peptide) were included. For pigs and patients, kidney protection was applied.

After administration of ^{177}Lu-OPS201, blood samples were taken up to 72 h for mice, up to 300 h for pigs, and up to 23 h for patients in order to measure the blood radioactivity contents by using the same well-type gamma counter (Packard Instruments). The human blood data were, originally, provided as relative values, normalized to the first blood sample immediately taken after injection. In order to convert the raw count values to blood uptake values per mL human blood in each time point, human blood data were quantified (in Bq/mL) retrospectively by using the same calibration factor as for the mouse study. As the data showed high variability, the median values of all mice and patients were used for further processing.

2.1. Image Acquisition and Reconstruction for Liver and Kidneys

2.1.1. For Pigs. After injection, multiple whole body (WB) planar images and SPECT/CT scans were acquired at 0.5, 2, 3, 4, 50, 100, 150, and 250 h to quantify the uptake in the kidneys and liver. SPECT/CT data and WB planar images were acquired using Symbia T16 (Siemens AG). The acquisition duration was 50 min for all scans: 10 min for WB and 40 min for SPECT (2 bed positions of 20 min each). In addition, a 5 min CT was performed for attenuation correction. For reconstruction, CT-based attenuation correction and triple energy window-based scatter corrections were applied. The images were reconstructed with the FLASH 3D iterative reconstruction algorithm with 6 iterations and 6 subsets. The resulting images were smoothed with a 6 mm Gauss filter.

2.1.2. For Patients. SPECT/CT data and WB planar images were generated with the Philips BrightView XCT equipped with a medium-energy, parallel-hole collimators SPECT/CT scanner. WB scans and low-dose SPECT/CT were performed at 1, 3, 24, and 72 h after 975 MBq mean administered activity of ^{177}Lu-OPS201. The acquisition duration was 43 min for all scans: 17 min for WB and 26 min for SPECT (2 bed positions of 13 min each). In addition, a CT was performed for attenuation correction. For reconstruction, CT-based attenuation correction and triple energy window-based scatter corrections were applied. The images were reconstructed with the Astonish (Philips) iterative reconstruction algorithm with 4 iterations and 16 subsets.

2.2. Dosimetry Analysis

2.2.1. Quantification of Activity and Integration of the Time-Activity Curves. To quantify the amount of activity, the average percentage values corresponding to the injected radioactivity (A%) per organ as a function of time were calculated for the liver, right kidney, left kidney, and blood for each species via a manual VOI analysis (for pigs and patients) and via gamma counter (for mice). For pigs, all VOIs were drawn based on the CT scan. In order to avoid spill-out effects, CT-based organ VOIs were enlarged as matching 2 voxels plus their actual CT-based volumes. For mice, scarified organs were counted by using the well-type gamma counter, total numbers of count values for the selected organs (kidneys and liver) were reported, and A% values were calculated. The time-activity curves of blood for each species were analyzed separately from the collected samples. Since the scan times of pigs were not exactly identical to those of all animals, the population-based A% values of pigs were used to create the time-activity curves for both selected organs and blood. For the mice and humans, since all scanning time points were identical in each study and the standard deviations in each time point are less than 5% (as is shown in the supplementary file), mean A% values for organs and median A% values for blood were used.

To analyze the interspecies differences in biokinetics of ^{177}Lu-OPS201, the time-dependent uptake data sets for the kidneys, liver, and blood were used, and individual fits (TACs) for each species including optimal fit function parameters by using the software solution NUKFIT [12] were created. The resulting fits were investigated to compare the biokinetics of the different species.

The organ TIACs were calculated by integration of the mean (for mice and humans) and population-based (for pigs) time-dependent uptake data sets using NUKFIT [12], choosing the optimal fit functions as proposed by the code. The TIACs are estimated by analytically integrating the fitted functions. Their standard error values are determined assuming Gaussian error propagation (can be seen in Supplementary Table 1). For this investigation, a systematic error in activity quantification of 10% was assumed for each measured data point.

2.3. Extrapolation Methods. There are several extrapolation approaches that are used to estimate TIAC values, absorbed doses, and in vivo biokinetics and biodistribution in humans based on animal data. Assuming the same biodistribution in animals and humans is one of the most commonly used methods, which means applying no extrapolation. In addition to this, relative mass scaling, time scaling, allometric scaling, and the combined relative mass and time scaling are the other techniques described in the literature; however, there is no common well-accepted method.

In this study, five interspecies extrapolation methods were applied on blood TIAC values (only for pigs) and kidneys and liver TIAC values (for mice and pigs) and examined to determine the optimal method for dosimetry [10, 13]. None of the extrapolation method could be applied on blood TIAC values of mice since the data for the total animal blood volume were not available.

Method 1 (equation (1)) ("same biodistribution approach") is based on the assumption that the TIACs for the same organ in an animal and human are the same [10]. Method 2 (equation (2)) is relative mass scaling in which the TIAC value of a human organ is set equal to the TIAC value of the same animal organ multiplied by the ratio of WB and the selected organ mass of the human and animal. Method 3 (equation (3)) is time scaling in which time is scaled by a power function of the ratio of WB masses of the human and animal for calculating the TIACs. In Method 3, the exponent is set to 0.25 [10]. Method 4 is a combined method: first time scaling is applied (equation (3)) and then the TIAC values of the animal are scaled based on relative mass scaling (equation (2)) [10]. Method 5 (equation (4)) applies allometric scaling in which TIACs of an animal are scaled by a power function of the ratio of WB masses of the human and animal. In this method, the exponent depends on the selected organ and is set equal to 0.92 for the liver and 0.82 for the kidneys [13]:

$$\text{TIAC organ}_{\text{human}} = \text{TIAC organ}_{\text{animal}}, \tag{1}$$

$$\text{TIAC organ}_{\text{human}} = \text{TIAC organ}_{\text{animal}} \times \frac{\left(m_{\text{organ}}/m_{\text{WB}}\right)_{\text{human}}}{\left(m_{\text{organ}}/m_{\text{WB}}\right)_{\text{animal}}}, \tag{2}$$

$$t_{\text{organ}_{\text{human}}} = t_{\text{organ}_{\text{animal}}} \times \left[\frac{\left(m_{\text{WB}}\right)_{\text{human}}}{\left(m_{\text{WB}}\right)_{\text{animal}}}\right]^{1/4}, \tag{3}$$

$$\text{TIAC organ}_{\text{human}} = \text{TIAC organ}_{\text{animal}} \times \left[\frac{\left(m_{\text{WB}}\right)_{\text{human}}}{\left(m_{\text{WB}}\right)_{\text{animal}}}\right]^{[b-1]}, \tag{4}$$

where m = mass, WB = whole body, t = time, b = scaling component, b (for liver) = 0.92, and b (for kidneys) = 0.85.

3. Results

3.1. Biodistribution and Dosimetry Calculations. Calculated lambda values used to create the TACs by using the optimal fit function parameters from NUKFIT for each

species and organ are shown in Supplementary Table 1. The respective species-dependent time-activity curves based on VOI and well-type gamma counter analysis for the kidneys, liver, and blood are displayed in Figures 1–3. Dots represent time-dependent percentage uptake data sets for the selected organs and blood, while lines represent individual fits (TACs) including fit function parameters from NUKFIT for the selected organs and blood in each species. Kidneys, liver, or blood fit curves including fit functions were named using the first letter of the kidneys, liver, or blood such as for mice (KM, LM, or BM), pigs (KP, LP, or BP), or humans (KH, LH, or BH), respectively. Since a logarithmic scale was used in all figures for better visualization, the error bars cannot be distinguished in total. However, all standard deviation values were less than 10% (shown in Supplementary Tables 2(a) and 2(b)). A fast blood clearance of the compound is observed in the first phase (largest half-life: 1.83 h; Supplementary Table 1) for each species. 10 min after injection, less than 5% of the injected activity per milliliter of blood circulates in pigs and humans (Figure 3). Overall, the blood clearance of OPS201 in pigs and humans was faster compared to mice.

The best approximation for the last phase of the liver curves for pigs and humans was a monoexponential function. However, the liver decay function in mice has biexponential characteristics. The slope of the last phase was lower than the corresponding function of pigs and humans. In comparison to patients, pigs show higher liver retention (Figure 2). As for kidneys, the shapes of curves for each species were similar (Figure 1).

The resulting TIACs based on extrapolation methods are summarized in Tables 1 and 2. Applying Method 1 (same biodistribution approach) to the mice data for both kidneys and liver resulted in underestimation by a factor of 4 for the kidneys and a factor of 7 for the liver compared to the patient data (kidney TIAC: mice = 1.4 h and patients = 5.9 h; liver TIAC: mice = 0.7 h and patients = 5.3 h). On the contrary, since pigs mimic humans better as compared to mice, Method 1 in pigs results in a slight overestimation for the kidneys and a slight underestimation for the liver by a factor of 1.3 (kidney TIAC: pigs = 7.7 h and patients = 5.9 h; liver TIAC: pigs = 4.1 h and patients = 5.3 h).

Most similar TIACs were obtained by applying time scaling (Method 3) and combined relative mass and time scaling (Method 4) methods (kidney TIAC: mice = 3.9 h, pigs = 4.8 h, and patients = 5.9 h; liver TIAC: mice = 0.9 h, pigs = 4.7 h, and patients = 5.3 h; Table 2). Other methods showed higher deviations.

The kidney TIAC values of mice (except the results after applying Method 3) are underestimated approximately fourfold in Method 1 and Method 4, and they are overestimated twelvefold by Method 2 (relative mass scaling) and Method 5 (allometric method). In contrast to the mouse data, the kidney TIAC values of pigs did not show high levels of variations; the data are overestimated 1.2–1.6 times in Method 1, Method 3, and Method 5.

For mice liver TIAC values despite of the scaling, even when applying Method 3, underestimations approximately by a factor of 6 (in Method 3) up to 17 (in other methods) were observed. For pigs liver TIAC values, only in Method 2 and Method 4, underestimations approximately by a factor of 5 were calculated; other applied methods show similar results.

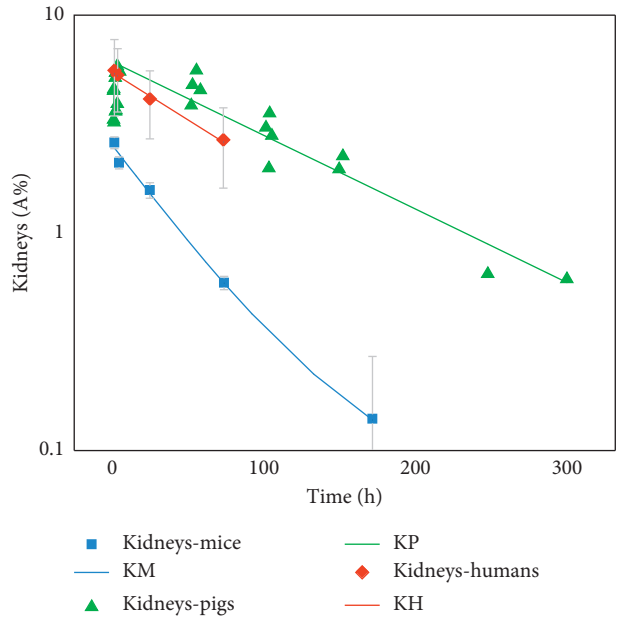

Figure 1: Time-activity curves of the kidneys based on VOI and well-type gamma counter analysis for each species. Dots: time-dependent percentage uptake data sets for the kidneys. Line: fit curves for the kidneys including fit function parameters from NUKFIT for mice (KM), pigs (KP), and humans (KH), respectively. All standard deviation values were less than 10% (can be seen in Supplementary Tables 2(a) and 2(b)).

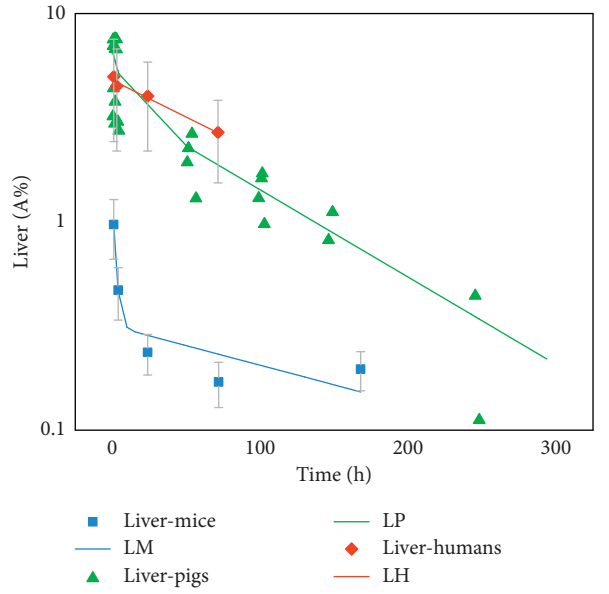

Figure 2: Time-activity curves of the liver based on VOI and well-type gamma counter analysis for each species. Dots: time-dependent percentage uptake data sets for the liver. Line: fit curves for the liver including fit function parameters from NUKFIT for mice (LM), pigs (LP), and humans (LH), respectively. All standard deviation values were less than 10% (can be seen in Supplementary Tables 2(a) and 2(b)).

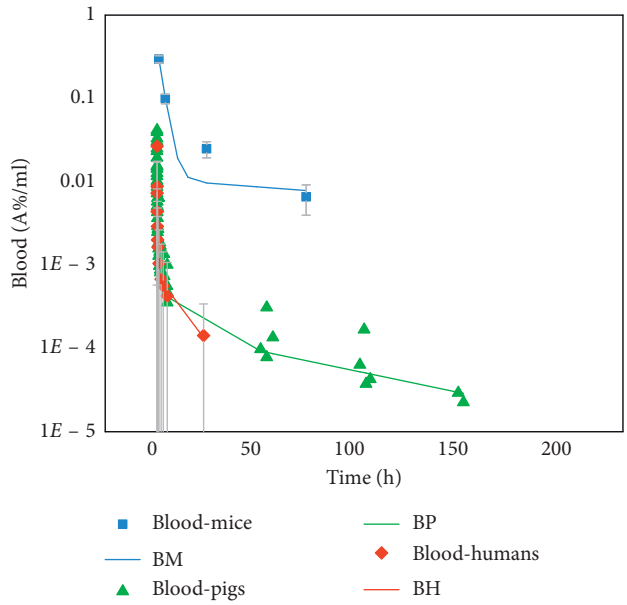

Figure 3: Time-activity curves of blood based on VOI and well-type gamma counter analysis for each species. Dots: time-dependent percentage uptake data sets for the blood. Line: fit curves for the blood including fit function parameters from NUKFIT for mice (BM), pigs (BP), and humans (BH), respectively. All standard deviation values were less than 10% (can be seen in Supplementary Tables 2(a) and 2(b)).

Table 1: Time-integrated activity coefficient (TIAC (unit: h)) values for the selected organs of mice, pigs, and humans with respective error calculated by NUKFIT with an assumption of 10% systematic error based on Method 1 (same biodistribution approach).

	Kidney TIAC ± error (h)	Liver TIAC ± error (h)	Blood TIAC ± error (ml/h)
Method 1			
Mice	1.44 ± 8.5*E* − 02	0.75 ± 4.1*E* − 02	0.0370 ± 2.0*E* − 03
Pigs	7.67 ± 1.8*E* − 01	4.08 ± 9.4*E* − 02	0.0002 ± 3.4*E* − 06
Humans	5.85 ± 4.2*E* − 01	5.32 ± 3.4*E* − 01	0.0002 ± 8.2*E* − 05

Table 2: Time-integrated activity coefficient (TIAC (unit: h)) values for the selected organs of mice and pigs based on applied scaling methods.

	Kidney TIAC (h)		Liver TIAC (h)		Blood TIAC (h/ml)
	Mice	Pigs	Mice	Pigs	Pigs
Method 2	0.43	4.17	0.32	1.04	0.00022
Method 3	3.89	8.73	0.88	4.65	0.00025
Method 4	1.17	4.75	0.38	1.18	0.00026
Method 5	0.44	6.63	0.40	3.78	0.00021

Method 2: relative mass scaling; Method 3: time scaling; Method 4: combined relative mass and time scaling; Method 5: allometric scaling.

4. Discussion

In this study, the in vivo biokinetics of ^{177}Lu-OPS201 for three species (mice, pigs, and humans) in the liver, kidneys, and blood were compared by using well-type gamma counter measurements and multiple WB planar and SPECT/CT images. In addition to this, all applicable scaling methods in the literature were summarized in order to identify an appropriate extrapolation method that minimizes the interspecies differences for comparing biokinetics, in vivo biodistribution, and dosimetry.

Observed interspecies differences in the fitted curves used to investigate the biokinetics show the necessity of scaling. Five interspecies extrapolation methods were tested on the kidneys and liver of both species (mice and pigs) and also on blood data of pigs. Our results show that all applied scaling methods, except time scaling (Method 3), result in a weight-dependent decrease of TIAC values and, consequently, the absorbed doses. Instead of Method 1, when the organ mass ratios between the species are high (e.g., for mice compared to humans), the scaling method either 3 or 4 should be applied to predict in vivo biokinetics, dosimetry, and absorbed doses in humans based on animal data more accurately. On the contrary, in small animals like mice, despite the applied extrapolation methods, interspecies differences may still be observed. For instance, in our study, none of the applied extrapolation methods on mice liver TIAC values provides similar values compared to humans due to the biphasic clearance of the OPS201 agent from the mice liver which was different compared to pigs and humans.

Although mouse models are applied widely in cancer translational research, there are still some limitations that need to be addressed [14]. Amongst others, the main differences in physiological parameters are the organ size, the heartbeat rate, and, as a consequence, the faster biological half-life of radioactive compounds in the animals [14]. In addition, gender-specific differences may play a role; however, the setup of the studies was not optimized to address these potential effects.

Allometric scaling may account partially for some of these effects as we have shown in our study (equation (4); Method 5). However, as de Jong and Maina stated [14], it is advisable to remain "critical and cautious about the applicability of animal data to the clinical domain."

Not only scaling but also the follow-up period plays an important role when investigating the biokinetics of therapeutic agents. In this study, the follow-up time in mice and patients was rather short, especially for an analysis of the biokinetics and dosimetry. The blood samples were taken from 1 h up to 72 h for mice and from 0.3 h up to 23 h for patients. We are missing the early phase (for mice) and late phase (for mice and humans) of the biokinetics. These data at early time points provide valuable information of the uptake pattern of the radiopharmaceutical, whereas for biodistribution and dosimetry assessments of ^{177}Lu-labeled compounds, the late time points (72 hours and later) have the greatest impact on the TIAC values which directly affect also the absorbed dose values [15]. In order to have sufficient data leading to more accurate results for analyzing the biokinetics and dosimetry, blood sampling at least up to 150–200 h is needed. As observed for blood, additional data on both early time points and late time points are needed for a better analysis of the liver and kidney biokinetics in mice and patients, despite the fact that the patterns in each species were similar.

Since the follow-up time of blood in mice and humans was not sufficient and, additionally, because of high variability in the median values for humans and mice blood data, mice blood data were neglected from the extrapolation method analyses. In addition, there is a lack of information about the total blood volume of mice; thus, the uptake of the radiopharmaceutical cannot be deduced. On the contrary, since we do not have these limitations in pigs, five extrapolation methods were applied on the pig blood data set. In addition to this, in pigs, measurements could be carried out over a longer period for dosimetry, biokinetics, and biodistribution assessments of therapeutic agents as compared to rodents, which makes the analyses more stable and accurate.

Since the kidneys and bone marrow are critical organs in ^{177}Lu-OPS201 treatment, applying our results to calculate bone marrow-absorbed doses could potentially improve the study analyses. Bone marrow dosimetry can be performed either on the basis of blood and whole body TIACs [16, 17] image based on scans of lumbar vertebrae 2–4 (LV2–4) [18]. As we have neither data for mice on the activity contents of bone marrow containing tissues nor LV2–4-segmented uptake values for the patients, a comparison of bone marrow dosimetry based on images (for humans) and on bone marrow uptake values (for mice) could not be performed. For the blood-based method, the main contributor to the bone marrow-absorbed dose is the TIAC of the blood ([16, 17]) which we have compared in our work. For future studies, it could be beneficial to have bone marrow tissue samples and/or corresponding image data for an improved comparison of bone marrow TIACs and, as a consequence, absorbed doses.

The fast blood clearance of the OPS201 in the first phase (<56 h) for each species was in agreement with studies of the agonist [15, 19]. Sandstrom et al. [15] observed a first phase with a mean effective half-life of 1.6 h, in agreement with our data for mice (1.8 h) and pigs (1.7 h). For humans, most likely because of the short observation period, the value was lower (0.5 h). For the late phase in pigs, our result (58 h) is also close to the results obtained in the human study with the agonist (43 h). Part of an ongoing phase 1 study [20] with ^{177}Lu-OPS201 in patients with SSTR-positive progressive NETs, in which dosimetry data are taken also at time points later than 48 h, is to substantiate whether the biokinetics of the agonist and antagonist in the pig model are comparable to those in the patients after treatment with ^{177}Lu-OPS201.

5. Conclusion

Extrapolation methods need to be applied in preclinical studies in order to predict the biokinetics, TIACs, absorbed doses, and dosimetry in humans more accurately. According to our results, if the organ mass ratios between the species are high (e.g., for mice compared to humans), the most adequate scaling method for TIACs is either time scaling or combination of relative mass and time scaling. Furthermore, this study shows that, for the ^{177}Lu-labeled dosimetry studies, follow-up times at late time points (more than 72 h) are needed for TIAC calculations in order to appropriately represent the area under the curve and to analyze both biokinetics and dosimetry accurately. Based on our analysis of the biokinetics, fit functions, and the TIAC values, pigs mimic humans better than mice. In addition to all of these topics mentioned above, increasing the number of subjects and including a gender-based analysis of biokinetics and dosimetry may produce even more representative results.

Abbreviations

A%: The average percentage values corresponding to the injected radioactivity
CT: Computed tomography
JR11: Cpa-c(DCys-Aph(Hor)-DAph(Cbm)-Lys-Thr-Cys)-DTyr-NH_2
^{177}Lu: Lutetium 177
NET: Neuroendocrine tumor
OPS201: DOTA-JR11
OPS202: NODAGA-JR11
PRRT: Peptide receptor radionuclide therapy
SD: Standard deviation
SST2: Somatostatin receptor subtype 2
TIACs: Organ-specific time-integrated activity coefficients
TACs: Individual time-activity fits
VOI: Volume of interest
WB: Whole body.

Data Availability

The data used to support the findings of this study are available from the corresponding author upon request.

Ethical Approval

As this study is a retrospective analysis of previously published data, all ethical approvals were provided in the respective publications [2, 3, 5]. All procedures involving pigs were performed after a written permission from the Danish Animal Experiments Inspectorate (no. 2014-15-0201–00102) [2]. Mice were housed and cared for according to Swiss regulations on animal experimentation (approval no. 789) [3]. For patients, the institutional review board (University Hospital of Basel) approved this study, and all subjects gave written informed consent in accordance with the Declaration of Helsinki [5].

Disclosure

Parts of the results of this work were presented at the "Annual Congress of the European Association of Nuclear Medicine, October 21–25, 2017" and at the "World Congress on Medical Physics and Biomedical Engineering, June 3–8, 2018."

Conflicts of Interest

Jens Kaufmann is an employee of OctreoPharm Sciences GmbH, Ipsen Group, Berlin, Germany.

Acknowledgments

We greatly appreciate the valuable help of Romain Bejot, Ipsen Pharma, for reviewing the time points of scans and thoroughly analyzing the blood biodistribution data for the pig study. This publication was funded by the German Research Foundation (DFG) and the University of Wuerzburg through the funding programme Open Access Publishing.

Supplementary Materials

Supplementary Table 1: calculated lambda values used to create the TACs by using the optimal fit function parameters from NUKFIT [12] for each species' organs and blood including standard deviation (SD) and coefficient of variation (CV) values determined assuming Gaussian error propagation. Supplementary Table 2(a): the median and mean percentage injected radioactivity (A%) values per ml in blood of mice and humans with corresponding standard deviation (SD). Supplementary Table 2(b): the mean percentage injected radioactivity (A%) values per ml in the kidneys and liver of mice and humans with corresponding standard deviation (SD). (*Supplementary Materials*)

References

[1] R. Cescato, B. Waser, M. Fani, and J. C. Reubi, "Evaluation of ^{177}Lu-DOTA-sst2 antagonist versus ^{177}Lu-DOTA-sst2 agonist binding in human cancers in vitro," *Journal of Nuclear Medicine*, vol. 52, no. 12, pp. 1886–1890, 2011.

[2] S. Beykan, J. S. Dam, U. Eberlein et al., "^{177}Lu-OPS201 targeting somatostatin receptors: in vivo biodistribution and dosimetry in a pig model," *EJNMMI Research*, vol. 6, no. 1, p. 50, 2016.

[3] G. P. Nicolas, R. Mansi, L. McDougall et al., "Biodistribution, pharmacokinetics, and dosimetry of ^{177} Lu-, ^{90} Y-, and ^{111} In-labeled somatostatin receptor antagonist OPS201 in comparison to the agonist ^{177} Lu-DOTATATE: the mass effect," *Journal of Nuclear Medicine*, vol. 58, no. 9, pp. 1435–1441, 2017.

[4] D. Wild, M. Fani, M. Behe et al., "First clinical evidence that imaging with somatostatin receptor antagonists is feasible," *Journal of Nuclear Medicine*, vol. 52, no. 9, pp. 1412–1417, 2011.

[5] D. Wild, M. Fani, R. Fischer et al., "Comparison of somatostatin receptor agonist and antagonist for peptide receptor radionuclide therapy: a pilot study," *Journal of Nuclear Medicine*, vol. 55, no. 8, pp. 1248–1252, 2014.

[6] M. van Essen, E. P. Krenning, B. L. R. Kam, M. de Jong, R. Valkema, and D. J. Kwekkeboom, "Peptide-receptor radionuclide therapy for endocrine tumors," *Nature Reviews Endocrinology*, vol. 5, no. 7, pp. 382–393, 2009.

[7] S. U. Dalm, J. Nonnekens, G. N. Doeswijk et al., "Comparison of the therapeutic response to treatment with a 177-lutetium labeled somatostatin receptor agonist and antagonist in preclinical models," *Journal of Nuclear Medicine*, vol. 57, no. 2, pp. 260–265, 2015.

[8] M. Ginj, H. Zhang, B. Waser et al., "Radiolabeled somatostatin receptor antagonists are preferable to agonists for in vivo peptide receptor targeting of tumors," *Proceedings of the National Academy of Sciences*, vol. 103, no. 44, pp. 16436–16441, 2006.

[9] U. Eberlein, M. Cremonesi, and M. Lassmann, "Individualized dosimetry for theranostics: necessary, nice to have, or counterproductive?," *Journal of Nuclear Medicine*, vol. 58, no. 2, pp. 97S–103S, 2017.

[10] R. B. Sparks and B. Aydogan, "Comparison of the effectiveness of some common animal data scaling techniques in estimating human radiation dose," in *Proceedings of Sixth International Radiopharmaceutical Dosimetry Symposium*, pp. 705–716, Oak Ridge, TN, USA, January 1999.

[11] D. J. Macey, E. Williams, H. B. Breitz, A. Liu, T. K. Johnson, and P. B. Zanzonico, *A Primer For Radioimmunotherapy and Radionuclide Therapy*, Medical Physics Publishing, Madison, WI, USA, 2001.

[12] P. Kletting, S. Schimmel, H. A. Kestler et al., "Molecular radiotherapy: the NUKFIT software for calculating the time-integrated activity coefficient," *Medical Physics*, vol. 40, no. 10, article 102504, 2013.

[13] S. Shen, R. F. Meredith, J. Duan et al., "Improved prediction of myelotoxicity using a patient-specific imaging dose estimate for non-marrow-targeting ^{90}Y-antibody therapy," *Journal of Nuclear Medicine*, vol. 43, no. 9, pp. 1245–1253, 2002.

[14] M. de Jong and T. Maina, "Of mice and humans: are they the same?--Implications in cancer translational research," *Journal of Nuclear Medicine*, vol. 51, no. 4, pp. 501–504, 2010.

[15] M. Sandstrom, U. Garske-Roman, D. Granberg et al., "Individualized dosimetry of kidney and bone marrow in patients undergoing ^{177}Lu-DOTA-Octreotate treatment," *Journal of Nuclear Medicine*, vol. 54, no. 1, pp. 33–41, 2012.

[16] A. C. Traino, M. Ferrari, M. Cremonesi, and M. G. Stabin, "Influence of total-body mass on the scaling of S-factors for patient-specific, blood-based red-marrow dosimetry," *Physics in Medicine and Biology*, vol. 52, no. 17, pp. 5231–5248, 2007.

[17] C. Hindorf, G. Glatting, C. Chiesa, O. Lindén, G. Flux, and E. D. Committee, "EANM dosimetry committee guidelines for bone marrow and whole-body dosimetry," *European Journal of Nuclear Medicine and Molecular Imaging*, vol. 37, no. 6, pp. 1238–1250, 2010.

[18] J. Blakkisrud, A. Løndalen, J. Dahle et al., "Red marrow-absorbed dose for non-hodgkin lymphoma patients treated with ^{177} Lu-lilotomab satetraxetan, a novel anti-CD37 antibody-radionuclide conjugate," *Journal of Nuclear Medicine*, vol. 58, no. 1, pp. 55–61, 2016.

[19] U. Eberlein, C. Nowak, C. Bluemel et al., "DNA damage in blood lymphocytes in patients after ^{177}Lu peptide receptor radionuclide therapy," *European Journal of Nuclear Medicine and Molecular Imaging*, vol. 42, no. 11, pp. 1739–1749, 2015.

[20] G. Nicolas, R. Baum, K. Herrmann et al., "Peptide receptor radionuclide therapy (PRRT) with a somatostatin receptor (SSTR) antagonist in patients with SSTR-positive, progressive neuroendocrine tumours (NETs): a phase I/II open-label trial to evaluate the safety and preliminary efficacy of ^{177}Lu-OPS201," *Neuroendocrinology*, vol. 105, p. 250, 2017.